Nanoscale

REVIEW

View Article Online
View Journal | View Issue

Cite this: *Nanoscale*, 2021, **13**, 9908

# A review on vertical and lateral heterostructures of semiconducting 2D-$MoS_2$ with other 2D materials: a feasible perspective for energy conversion

Gayatri Swain, Sabiha Sultana and Kulamani Parida *

Received 10th February 2021,
Accepted 10th May 2021

DOI: 10.1039/d1nr00931a

rsc.li/nanoscale

Fossil fuels as a double-edged sword are essential to daily life. However, the depletion of fossil fuel reservoirs has increased the search for alternative renewable energy sources to procure a more sustainable society. Accordingly, energy production through water splitting, $CO_2$ reduction and $N_2$ reduction *via* photocatalytic and electrocatalytic pathways is being contemplated as a greener methodology with zero environmental pollution. Owing to their atomic-level thickness, two-dimensional (2D) semiconductor catalysts have triggered the reawakening of interest in the field of energy and environmental applications. Among them, following the unconventional properties of graphene, 2D $MoS_2$ has been widely investigated due to its outstanding optical and electronic properties. However, the photo/electrocatalytic performance of 2D-$MoS_2$ is still unsatisfactory due to its low charge carrier density. Recently, the development of 2D/2D heterojunctions has evoked interdisciplinary research fascination in the scientific community, which can mitigate the shortcomings associated with 2D-$MoS_2$. Following the recent research trends, the present review covers the recent findings and key aspects on the synthetic methods, fundamental properties and practical applications of semiconducting 2D-$MoS_2$ and its heterostructures with other 2D materials such as g-$C_3N_4$, graphene, CdS, $TiO_2$, MXene, black phosphorous, and boron nitride. Besides, this review details the viable application of these materials in the area of hydrogen energy production *via* the $H_2O$ splitting reaction, $N_2$ fixation to $NH_3$ formation and $CO_2$ reduction to different value-added hydrocarbons and alcohol products through both photocatalysis and electrocatalysis. The crucial role of the interface together with the charge separation principle between two individual 2D structures towards achieving satisfactory activity for various applications is presented. Overall, the current studies provide a snapshot of the recent breakthroughs in the development of various 2D/2D-based catalysts in the field of energy production, delivering opportunities for future research.

## 1. Introduction

The exacerbation of global warming, the energy crisis and environmental pollution in the $21^{st}$ century is highly related to the depletion of fossil fuels, which is becoming one of the biggest challenges with the rapid industrial and population growth.[1–3] Additionally, the consumption of fossil fuels significantly contributes to the greenhouse effect by emitting $CO_2$.[1,4] Therefore, to alleviate these problems and achieve a greener world, photocatalysis and electrocatalysis have emerged as the Holy Grails of green and sustainable technology towards the conversion of solar energy and electric energy into chemical energy through water splitting, $N_2$ reduction, and $CO_2$ reduction.[5–8] However, for the efficient utilization of solar energy together with the extensive use of electrocatalysis, the choice of catalyst is essential.[9–11]

In recent decades, nanostructured materials have become one of the main influencers in the field of photo/electrocatalysis mainly due to their large surface area, quantum confinement effect and dominant interfacial phenomena.[12–15] In contrast to conventional 0D and 1D catalysts with restricted dimensions, catalysts based on 2D materials have attracted a great deal of attention in the field of catalysis due to their remarkable physical and chemical properties together with controllable optical and electronic properties. Due to their planar structure and abundant exposed surface atoms, 2D materials provide a large number of active sites for photo/electrocatalytic reactions. In addition, they possess sufficient space for the integration of various catalysts, thus enhancing the flexibility of catalytic activity and formation of new active sites.[9,16–20] The design of 2D materials has been inspired by one particular two-dimensional material, graphene, which is considered the tip of the iceberg, where the first real and

---

*Centre for Nanoscience and Nanotechnology, Siksha 'O' Anusandhan (Deemed to be University), Jagamohan Nagar, Jagamara, Bhubaneswar-751030, Odisha, India. E-mail: kulamaniparida@soa.ac.in, paridakulamani@yahoo.com*

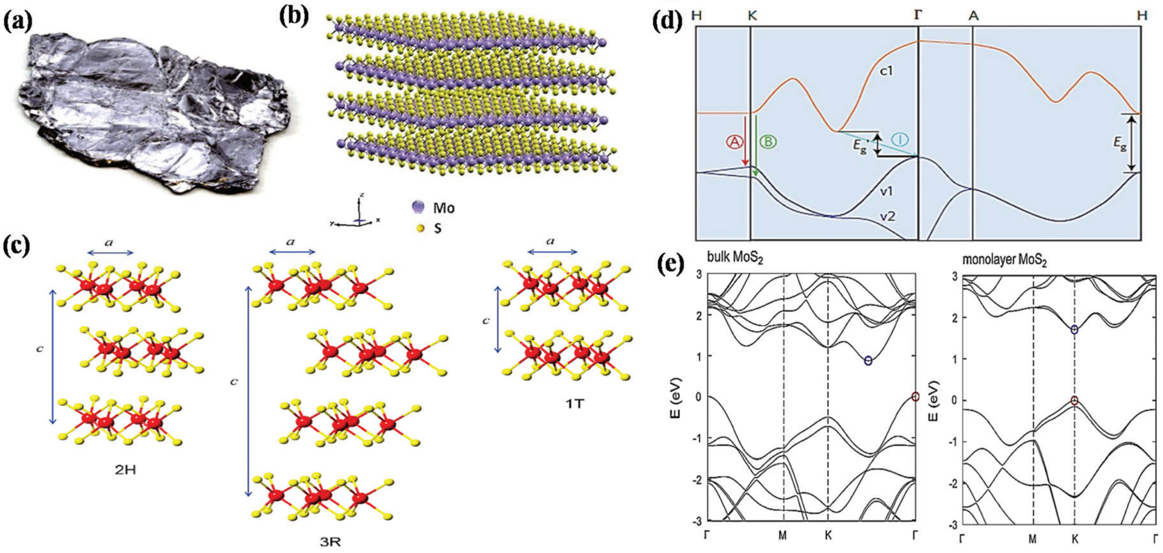

**Fig. 1** (a) Picture of bulk $MoS_2$ crystal. Reproduced from ref. 29. (b) Three-dimensional model of the crystal structure of $MoS_2$. Reproduced from ref. 33. (c) Schematic illustration of the various crystal structure polytypes: 2H, 3R and 1T. Reproduced from ref. 36. (d) Typical band structure of $MoS_2$, where c1 represents the conduction band and v1 and v2 the valence bands. A and B show the direct band-gap transitions and I stands for the indirect band-gap transition. $E_g$ and $E'_g$ represent the direct and indirect band-gap for the monolayer and bulk, respectively. Reproduced from ref. 28. (e) Illustration of the electronic band structures of bulk and monolayer $MoS_2$. Reproduced from ref. 29.

thermodynamic stable single 2D sheet of graphite was reported by Novoselov and Geim in 2004.[19,21] After the first seminal isolation of graphite, graphene and its derivatives have been employed as significant catalysts in a variety of catalytic applications, triggering the search for other 'beyond graphene' materials. Therefore, a wide range of 2D materials, especially those similar to graphene have been applied in a wide range of fields such as photocatalysis, electrocatalysis, energy storage, and biosensors. To date, for instance, numerous 2D materials (single and 2D-based composites) such as hexagonal boron nitride, graphitic carbon nitride, transition metal chalcogenides, MXenes, layered double hydroxides, and boron phosphides have been developed.[22–25]

However, the development of the research interest in the photo/electrocatalysis field has diverted attention toward transition metal dichalcogenides especially 2D-$MoS_2$, a chalcogenide derivative of molybdenum and a rising star in the graphene analogous family.[26–29] $MoS_2$ is an inorganic silvery black solid (Fig. 1a), which mainly occurs in nature as the mineral molybdenite, the principal ore of Mo.[29–31] As depicted in Fig. 1b, the

**Gayatri Swain**

*Dr Gayatri Swain completed her Master of Science (M.Sc.) in Chemistry from Berhampur University, Odisha, India in 2014 and then completed her PhD in 2020 at Siksha 'O' Anusandhan (Deemed to be University), Bhubaneswar, India under the supervision of Prof. Kulamani Parida. At present she is working as a Research Associate at the Centre for Nanoscience and Nanotechnology, Siksha 'O' Anusandhan (Deemed to be University), Bhubaneswar, India. She is the author of 10 international journal articles with one book chapter. Her current research interests are mainly focused on the synthesis of two-dimensional transition metal dichalcogenides and their application towards energy and environmental benefits.*

**Sabiha Sultana**

*Dr Sabiha Sultana received her Bachelor's Degree from Utkal University, Bhubaneswar in 2012 and M.Sc. Chemistry from Ravenshaw University, Cuttack in 2014. Then, she joined as a PhD student under the supervision of Prof. K. M. Parida the Centre for Nanoscience and Nanotechnology, ITER, SOA Deemed to be University and recently completed her PhD Degree. Her research area focuses on the development of nanostructured materials including metal oxides, metal sulphides, and phosphides and their application towards water splitting, $N_2$, $CO_2$ reduction, and pollutant abatement. She has published 12 research articles in various international journals.*

structural units of $MoS_2$ arrange themselves in a way that the transition-metal atom exhibits six-fold coordination and is covalently bonded in between two chalcogen atomic layers in an S–Mo–S fashion, forming a sandwich layer, and each sandwich layer connects to the other by means of weak interlayer van der Waals forces.[31–33] According to the atomic co-ordination of the surrounding S atoms with respect to the central Mo atom and stacking sequence of each $MoS_2$ layer, the crystal structure of $MoS_2$ has been classified into 3 types of polymorphs, among which two configurations occur naturally (2H and 3R), whereas the other polytype (1T) is synthetically available (Fig. 1c). The terms H, R and T represent hexagonal, rhombohedral and tetragonal, and hence their naming depends on their symmetry. The 2H and 3R phase of $MoS_2$ is semiconducting, while the 1T phase of $MoS_2$ is metallic.[31,34–36] In particular, the crystal structure of 2H-$MoS_2$ mainly consists of an Mo central atom surrounded by 6 sulfide ($S^{2-}$) ligands, which occupy a trigonal prismatic coordination sphere, where each sulfur center is connected to 3 Mo centres to form a pyramidal structure. Accordingly, several trigonal prisms are intertwined to construct a layered structure in which one layer of Mo atoms is sandwiched between two sheets of S atoms, resulting in the formation of a hexagonal sheet-like structure of $MoS_2$.[37] The basic difference between the two naturally occurring forms of $MoS_2$, *i.e.*, 2H-$MoS_2$ and 3R-$MoS_2$, is the stacking order of the S–Mo–S sheets in their unit cell. Moreover, the stacking order of 2H-$MoS_2$ is AbA BaB, *i.e.*, 2 S–Mo–S units per primitive unit cell with hexagonal symmetry in the space group *P*63/*mmc*, whereas 3R-$MoS_2$ exhibits rhombohedral symmetry with the stacking order of AbA CaC BcB, *i.e.*, 3 S–Mo–S units per unit cell in the space group *R*3*m*. In the stacking order model, the upper and lower cases represent the relative position of the S and Mo atoms, respectively. 1T-$MoS_2$ is a one-layer crystal cell that has tetragonal polytype symmetry, in which the Mo atoms are octahedrally coordinated by six S atoms in the AbC AbC… stacking order.[34,38,39] Most experimental studies reveal that 1T-$MoS_2$ is a metastable structure that can be completely transformed to 2H-$MoS_2$ upon annealing over a particular temperature range.[34,40] However, according to the current research, the most widely studied phase of $MoS_2$ is semiconducting, *i.e.*, 2H-$MoS_2$, which is attributed to its excellent stability, unique structural arrangement, suitable band gap for various catalytic reactions, *etc*. Therefore, in the current review, we extensively focus on two-dimensional semiconducting 2H-$MoS_2$.

The electronic structure of semiconducting 2H-$MoS_2$ includes its band structure and change in band structure, which are controlled by the number of layers and change in hybridization between the d orbital and $P_z$ orbital of Mo and S, respectively.[31,37] The band structure and change in band gap with respect to layer number is illustrated in Fig. 1d and e, respectively.[28,29] According to the literature, bulk $MoS_2$ possess an indirect bandgap with an energy gap of 1.2 eV, while its bandgap becomes direct for few or single-layer $MoS_2$ with an energy gap of about 1.9 eV, which varies with the tuning of the layer of $MoS_2$.[39] From an experimental view, it has been found that few-layer $MoS_2$ exhibits four weak humped absorption peaks in the wavelength range of 250–700 nm. Among them, the characteristic peaks observed in the range of 250–450 nm are mainly attributed to the higher excited states or bands, whereas the doublet located in the range of 600–700 nm originates from the direct excitonic transition occurring at the Brillouin zone *K* point between the VBM and CBM due to the spin–orbit dissociation of transition at that point.[37,39] Moreover, the change in bandgap energy, *i.e.*, from indirect to direct with a change in layer number also greatly affects the photoluminescence spectrum (PL), absorption spectrum and photoconductivity of $MoS_2$. It has been shown that the intensity of the PL spectrum is inversely proportional to the layer number, where few-layer or thin layer $MoS_2$ exhibits the strongest PL intensity with a large quantum efficiency. Experimentally, the two excitonic peaks in the PL spectrum of $MoS_2$ are observed at ~1.9 eV and ~2.08 eV at the *K* point, which may be due to the spin–orbit band splitting near the valence band. It has been shown that monolayer $MoS_2$ exhibits a main peak at 1.9 eV due to its direct gap luminescence, whereas few layer $MoS_2$ show additional peaks together with the main peak originating from the direct gap hot luminescence and indirect-gap luminescence.[37,41] Further, the valence band is derived from the overlapping of the filled $d_{z^2}$ orbital of Mo-4d with the filled sp orbital of the S atoms. Conversely, the conduction band is determined by the degenerate Mo-3d orbitals, *i.e.*, $d_{x^2-y^2}$, $d_{z^2}$, which overlap with the empty antibonding orbitals of the S atom.[39]

$MoS_2$ has two distinctive orientations in its structure, namely basal planes with surface inertness and edge planes with high surface energy, and each orientation is terminated by chalcogen atoms. The electrical conductivity along the layer is very high, while it is low across the van der Waals gaps

**Kulamani Parida**

*Prof. Kulamani Parida currently works as a Distinguished Professor in Chemistry and Director of the Centre for Nanoscience and Nanotechnology, Siksha O Anusandhan, Deemed to be University, Odisha, India. He received his PhD degree and DSc from Utkal University in 1981 and 2002, respectively, on solid-state chemistry and catalysis. In 1981, he joined the Regional Research Laboratory, Bhubaneswar and worked there for 37 years and retired as a Chief Scientist and Head of Colloids and Materials Chemistry Department. His area of interest covers extensive research on narrow and wide band gap semiconductors, metal oxides, metal phosphides, metal sulphides, metal carbides and nitrides exhibiting efficient electro and photocatalytic water splitting and pollutant degradation activity.*

between the layers, which indicates that compared to the basal planes, the edge sites exhibit the fast transportation of electrons.[30,42,43] Hence, in recent decades, ultrathin $MoS_2$ has been demonstrated to be an excellent electrocatalyst towards the hydrogen evolution reaction.[43,44] Moreover, its properties such as high chemical stability, superior charge carrier mobility, good surface to volume ratio and visible light absorbing property makes it an ideal candidate catalyst for photocatalytic reactions.[39,45–48] More importantly, $MoS_2$ is considered to be a good substitute for noble metals (such as Pt, Rh, Ru, and Pd) and a low-cost catalyst for both photocatalytic and electrocatalytic reactions. Although the absorbance edge of $MoS_2$ extends from the UV-Vis to IR region, which seems ideal as a solar light harvester, single $MoS_2$ has negligible photocatalytic activity towards energy production. This poor photocatalytic activity is attributed to the insufficient charge separation and low conductivity power between the adjacent S–Mo–S layers, which lead to poor charge mobility.[49–51] Accordingly, the abovementioned difficulties have been overcome using various techniques such as sulfur edge activation, phase transition, heteroatom doping, and fabrication of heterojunction or composite with other materials. Among the various strategies, many studies reveal that the formation of hierarchical composites of $MoS_2$ with other 2D-layered materials such as 2D-metal, 2D-semiconductor and 2D-insulator provides abundant active sites and immense surface area, which greatly enhance the effectiveness of the reaction.[52–55]

Although several excellent reviews summarizing the advantages, synthetic techniques, different physicochemical properties and potential application of 2D/2D heterostructures have been published, there is no comprehensive review on 2D-$MoS_2$-based 2D/2D heterostructure materials. Therefore, herein we present an in-depth overview on the recent progress in the development of 2D $MoS_2$-based 2D/2D heterostructure catalysts towards energy production. It includes various emerging strategies and fundamental aspects on the recent development of 2D $MoS_2$ and its synthetic methods, photocatalytic and electrocatalytic activity, and on-demand modification of its photo/electrocatalytic activity *via* the introduction of other 2D materials. Subsequently, the various applications summarized in this review mainly include photocatalytic and electrocatalytic hydrogen evolution, $CO_2$ reduction and nitrogen reduction. Therefore, in this review, we offer the latest progress in the 2D-$MoS_2$ based 2D/2D heterostructure catalyst towards energy benefits along with various catalytic mechanisms.

## 2. Basis for 2D/2D heterostructures and types of interfacial coupling

2D/2D material-based composites possess a solid structure, which provides a large intimate contact interface between the individual materials, resulting in excellent photo/electro stability in the catalyst.[17,56,57] Moreover, in 2D/2D heterostructures, interfacial charge migration and separation is more efficient due to the formation of a large contact area, which provides trapping channels by the large lateral size of the combined 2D materials. In the case of photocatalytic reactions, besides the formation of a high surface contact, the type and nature of the intimate interface are crucial parameters to accelerate charge carrier migration, thus suppressing the formation of photogenerated electron–hole pairs.[58–63]

Generally, there are two directions, *i.e.*, vertical and lateral, for the engineering of 2D/2D heterostructures with a different contact interface (Scheme 1). In the lateral direction, 2D/2D heterostructures are successfully achieved through the cross-section interface contact *via* the epitaxial growth method, which can be considered to be both a patterned and paralleled contact surface. In contrast, 2D/2D heterostructures in the vertical direction are realized *via* face-to-face contact and acquired by stacking two or multiple monolayer sheets of different nanomaterials. This method proceeds through atomic precision by regulating the relative orientation between the single 2D components.[54,64–67] However, Wang *et al.* demonstrated a

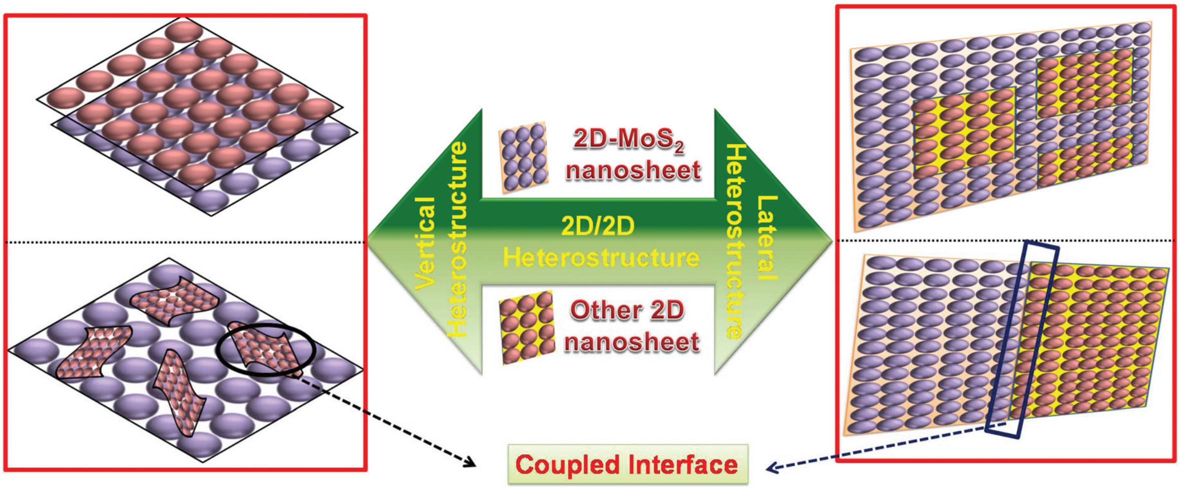

**Scheme 1** Schematic representation of the 2D/2D vertical (left) and lateral (right) heterostructures with a coupled interface.

high-quality $MoS_2$ : h-BN vertical heterostructure *via* a stacking process of two 2D crystals on top of each other, which provided better interlayer interaction at the interface.[68] Behranginia *et al.* synthesized a lateral $MoS_2$/graphene 2D/2D heterostructure, which provided a high quality lateral interface between $MoS_2$ and graphene.[69] Moreover, Yoo and coworkers reported both a lateral and vertical heteroepitaxy interface between $WS_2$ and $MoS_2$ monolayers by carefully controlling the contamination and defects in each 2D crystal. The as fabricated lateral and vertical 2D/2D heterostructure provides a building block for an abrupt and patterned junction in 2D materials.[70]

In terms of bonding, 2D/2D heterostructure including covalently bonded and van der Waals interacted heterostructures fall in a category. Considering that the layers of 2D materials are connected by *via* both covalent bonding (strong) and van der Waals forces (weak), during the formation of a well-defined 2D/2D heterostructure with a covalent bonding interface, it is necessary to maintain both the lattice constant matching and valence matching on each side of the interface. However, in terms of van der Waals integration, although the van der Waals forces between the layers are weak, it does not rely on either lattice matching or valence matching, but facilitates the formation of a broader heterostructure phase space, which mediates various catalytic reaction across the interface.[64,66,71,72] Thus, it has been concluded that to successfully construct a 2D/2D interface, it is necessary to achieve strong interfacial bonding by optimizing the interaction forces in the composite structure. Generally, in the case of $MoS_2$-based 2D/2D heterostructures, the strength of the interfacial bonding is regulated through various factors such as chemical bonding, Coulomb force, van der Waals force, and electrostatic interaction. For example, Yu and his group designed an $MoS_2$/graphene 2D/2D van der Waals heterostructure with face-to-face contact through the alternating arrangement of monolayer $MoS_2$ nanosheets and graphene. It was observed that the obtained coupled interface improved the electronic conductivity of the heterostructure material by providing more edge active sites and defects.[73] Further, Shi *et al.* employed a simple electrostatic self-assembly process followed by the hydrothermal method to design $MoS_2$/g-$C_3N_4$ nanosheets, which provided abundant available reaction sites for enhanced photocatalytic activities. In this case, the positively charged g-$C_3N_4$ obtained *via* the protonation method interacts electrostatically with the negatively charged $MoS_4{}^{2-}$ under hydrothermal treatment.[74] In addition, each atom, *i.e.*, Mo and S, present in $MoS_2$ also contributed to the formation of chemical bonds during the construction of 2D/2D heterostructures. For example, Zhao *et al.* reported an *in situ* pyrolysis strategy to achieve 2D/2D $MoS_2$/$C_3N_4$-based electrodes through Mo–N coordination between 2D-$MoS_2$ and 2D-$C_3N_4$, which act as the main active sites for catalyzing the NRR by promoting electron transfer, thus improving the catalytic activity across the $MoS_2$/$C_3N_4$ interface.[75] In another study, Swain *et al.* fabricated strong interface coupling between 2D-$MoS_2$ and 2D-$CaIn_2S_4$ through an S–S linkage, which facilitated the channelization of photogenerated charge carriers throughout the interface of both 2D materials.[76] Furthermore, Wan *et al.* developed an Au-coupled $Bi_2WO_6$–$MoS_2$ heterojunction photocatalyst in which the charge transfer process occurred from the surface of $Bi_2WO_6$ to $MoS_2$ *via* the interfacial S–O bonds. It was observed that the interfacial S–O bond is derived from the outer sulfur atoms and vertex oxygen atoms present in the $MoS_2$ layer and $WO_6$ octahedron of $Bi_2WO_6$, respectively.[77]

## 3. Procedures for the synthesis of 2D-$MoS_2$ and $MoS_2$-based 2D/2D heterojunction composites

The practical application of various 2D nanomaterials is mainly governed by their exposed active sites, and thus it is an essential requirement to design nanomaterials with properties having large area uniformity and layer controllability. Accordingly, considerable efforts have been devoted to the construction of 2D $MoS_2$ and $MoS_2$-based 2D/2D heterostructures with satisfactory yields, controllable thickness, unique size, and controllable morphologies by engineering synthetic techniques. The detailed procedures employed for the synthesis of 2D-$MoS_2$ together with its 2D/2D heterostructures are depicted in Scheme 2.

### 3.1 Synthesis of 2D-$MoS_2$

To date, numerous synthetic procedures have been developed for the synthesis of various nanostructured 2D $MoS_2$, which can be divided into two routes, *i.e.*, (a) top-down routes including mechanical exfoliation and chemical exfoliation and (b) bottom-up routes including hydrothermal and solvothermal method, chemical and physical vapour deposition, and decomposition method.[32,39]

**3.1.1 Top-down routes.** The top-down approach mainly relies on the preparation of nanostructured 2D-$MoS_2$ from its respective bulk counterparts. It is mainly based on the exfoliation of layered bulk structured materials into few or single layers by breaking the van der Waals interaction between the layer *via* various driving forces as follows.

*3.1.1.1 Mechanical exfoliation.* Similar to the Scotch tape method for the preparation of graphene from graphite, bulk $MoS_2$ is attached on an adhesive tape and subjected to repeated exfoliation on the support of a substrate to produce a high-quality monolayer phase of $MoS_2$. Consequently, its pristine crystal structure is the same as that of its bulk. Li and co-workers constructed $MoS_2$ nanosheets through the mechanical exfoliation method using $Al_2O_3$ ceramic substrates.[78] As illustrated in Fig. 2a, thin $MoS_2$ flakes were obtained when the attached Scotch tape was removed from the bulk $MoS_2$ crystals by repeatedly folding and separating the Scotch tape-adhered $MoS_2$ flakes. Subsequently, the Scotch tape attached to the $MoS_2$ thin flakes was tightly pasted onto a clean $Al_2O_3$ ceramic substrate on the support of Ag–Pd interdigital electrodes and left for about 6 h to maintain the adhesion state. To remove the adhesive

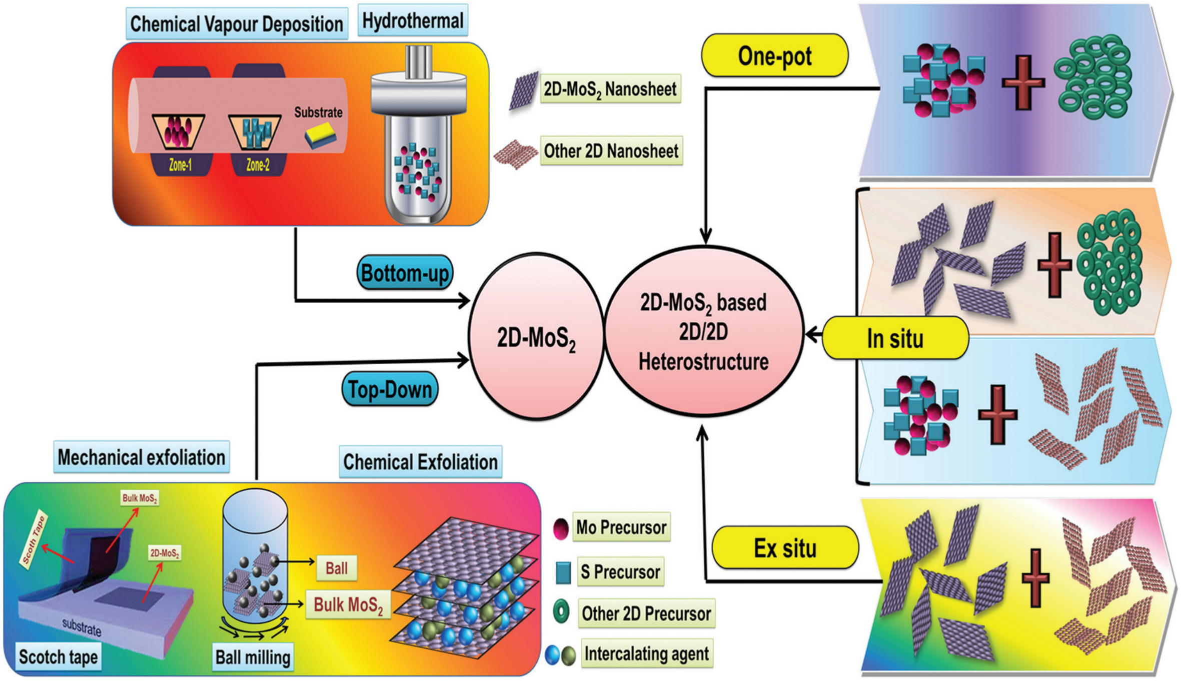
Chemical Vapour Deposition
Hydrothermal
Zone-1
Zone-2
Substrate
2D-MoS$_2$ Nanosheet
Other 2D Nanosheet
One-pot
Bottom-up
2D-MoS$_2$
2D-MoS$_2$ based 2D/2D Heterostructure
In situ
Top-Down
Mechanical exfoliation
Chemical Exfoliation
Scotch Tape
Bulk MoS$_2$
2D-MoS$_2$
substrate
Scotch tape
Ball
Bulk MoS$_2$
Ball milling
Mo Precursor
S Precursor
Other 2D Precursor
Intercalating agent
Ex situ

**Scheme 2** Schematic illustration of the various techniques used for the synthesis of 2D-MoS$_2$ and its 2D/2D-heterostructures.

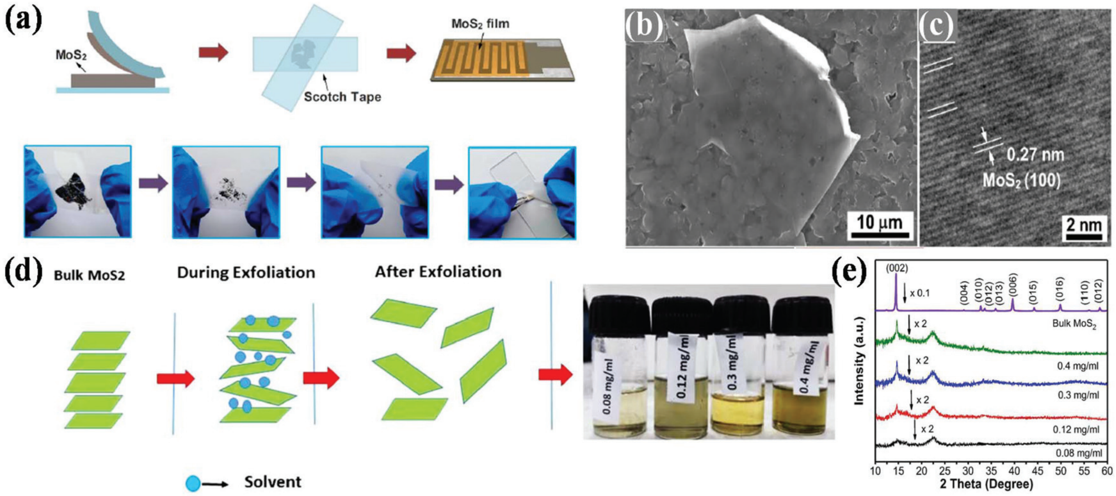

**Fig. 2** (a) Schematic diagram showing the mechanical exfoliation technique for the synthesis of MoS$_2$ nanosheets, and (b) SEM and (c) HRTEM images of MoS$_2$ nanosheets. Reproduced from ref. 78 (d) Scheme of the synthesis process *via* the liquid-phase exfoliation of MoS$_2$ nanosheets and (e) X-ray diffraction patterns of bulk MoS$_2$ powder and MoS$_2$ nanosheets synthesized using different initial concentrations of bulk MoS$_2$. Reproduced from ref. 81.

residue from the Scotch tape, acetone was used as the solvent. The as-obtained few-layer microstructure of MoS$_2$ exhibited a smooth surface on the substrate together with the same pattern as the substrate and it possesses the good crystallinity of MoS$_2$ nanosheets with an ordered arrangement of lattice fringes, as presented in Fig. 2b and c. However, this process requires a substrate for sample preparation, which gives a very low product yield, and it is very difficult to control the size, shape and thickness of the resulting material. Consequently, this method is not suitable for the large-scale production of the materials. Besides the Scotch tape method, ball milling is another strategy that is also responsible for the synthesis of high-quality 2D MoS$_2$ nanosheets. Krishnamoorthy *et al.* mechanically delaminated bulk MoS$_2$ into few-layered MoS$_2$ nanosheets using the ball milling method. The ball milling method is performed in a ball and bowl made up of tungsten carbide, and *N*-methyl-2-pyrrolidine (NMP) is used as the solvent throughout the reaction. After ball milling at a speed of 300 rpm, the final MoS$_2$ product is obtained after washing with ethanol followed by drying.[79] Besides the Scotch tape and ball milling techniques, in 2012, Gacem's group reported an anodic bonding technique, in which high-quality nanosheets with high yield, good optical properties and excellent purity were obtained.[80]

*3.1.1.2 Liquid-phase exfoliation.* In this method, few-layered materials are prepared directly under the influence of various solvents followed by the joint action of sonication and centrifugation. Here, sonication breaks the weak van der Waals interaction present between the stacking layers without destroying the covalent bonding in each layer.[38] This technique includes ion intercalation, ion exchange and ultrasonic cleavage, which generates a large amount of 2D-$MoS_2$ with good quality single and few-layered nanosheets. The choice of solvent is a key parameter in liquid exfoliation, where there should be a good match between the solvent and surface tension present between the layers, which minimizes the energy required for exfoliation, thus increasing the exfoliation efficiency. Here, the number of layers in the resulting 2D materials is governed by the choice of solvent together with the concentration of the precursor solute. Gupta and co-workers prepared $MoS_2$ nanosheets through the liquid-phase exfoliation method using NMP as the exfoliating solvent. From experimental studies, it has been deduced that the presence of a small mole fraction of water in NMP stabilizes the $MoS_2$ nanosheets in the dispersion during sonication. Particularly, the stability of the $MoS_2$ nanosheets in the NMP dispersion solution is due to the water molecules confined at the Mo edges of $MoS_2$, which prevent chemical erosion of the edges. This, enhances the interaction between the NMP solvent and $MoS_2$, leading to a stable dispersion.[82] Therefore, it has been concluded that the use of solvent during the exfoliation method is not only responsible for the synthesis of two-dimensional nanosheets, but also plays a big role in stabilizing the nanosheets. In the literature on studies regarding liquid-phase exfoliation, it has also been observed that solvents with a low volatile rate hamper the rate of exfoliation and yield of 2D catalysts. Thus, the choice of solvent with a high volatility rate is another crucial factor that should be considered. Accordingly, Sahoo *et al.* employed a cost-effective liquid-phase exfoliation route for the scalable production of high-quality $MoS_2$ nanosheets using acetone as the solvent. The use of acetone as a solvent overcomes the drawbacks of low-volatility solvents. In this method, the bulk $MoS_2$ is exfoliated into 2D-$MoS_2$ nanosheets *via* sonication followed by centrifugation. The synthetic method involves several steps as follows: (i) grinding of bulk $MoS_2$ using a mortar and pestle followed by drying to evaporate the water and impurities, (ii) addition of acetone to a particular concentration of dried $MoS_2$ in a glass vial, (iii) treatment in a sonication bath to interrupt the weak van der Waals force present between the adjacent layers, and (iv) finally the supernatant is collected using a micropipette after centrifugation followed by filtration. Fig. 2d depicts the procedure for the synthesis of $MoS_2$ nanosheets *via* the weakening of van der Waals forces, which helps in thinning the layers, where the exfoliation procedure proceeds with different initial concentrations. As shown in Fig. 2e, the strong diffraction peak observed at the (002) plane decreases gradually with a change in the initial concentration of bulk $MoS_2$ in a given concentration of solvent, indicating that the bulk $MoS_2$ is exfoliated to few layers. Moreover, in the case of the ion intercalation mechanism, cations are intercalated into the interlayer spacing of the bulk materials to destroy the van der Waals interaction present between the layers.[81] However, the use of harmful toxic organic solvents, low quantum yield, and small lateral size of the as-obtained sheets limit its large scale utilization by many researchers.

**3.1.2 Bottom-up approach.** The bottom-up approach is the most compatible method used to fabricate the target substance with certain precursors followed by chemical reactions mainly in the solution phase. In some cases, surfactants are often used, which mainly help to stabilize the products and control their shape, size and morphology.

*3.1.2.1 Chemical vapour deposition.* The chemical vapour deposition (CVD) approach involves the growth mechanism of the products *via* chemical reactions and has been proven to be a beneficial method to synthesize high-quality substances that are thin and highly conductive, especially $MoS_2$ films. The CVD method requires a two-furnace approach to control the temperature of both Mo and S precursors separately. In a typical process, the desired product is obtained due to the redox reaction between the reactant precursors on the support or surface of a substrate whenever one or more volatile precursors decompose and react with each other at high temperature and high vacuum conditions. Typically, the growth temperature is maintained about 700–1000 °C and for the growth of 2D-$MoS_2$ thin layers, various substrates are employed as insulating supports. Initially, the $MoS_2$ precursors such as Mo, $MoO_3$, $(NH_4)_2MoS_4$ are deposited on the supporting surface and then subjected to thermal decomposition or sulfurization at an elevated temperature to generate $MoS_2$ layers with controlled structures.[37,46,83]

In addition, by customizing the essential parameters (growth temperature and time, flow rate of the carrier gas, mass amount, and the position of both the reactant and substrate), a high-quality $MoS_2$ monolayer can be achieved together with tunable film thickness and large active sites, which are beneficial for interplanar charge transport. Wan and his group demonstrated fractal-shaped single-layer $MoS_2$ to engineer the active sites of $MoS_2$ through the CVD method on a fused silica substrate. It was observed that water-soluble polymer-assisted method prevented the formation of the fractal-shaped morphology during the transformation process.[84] Li and co-workers employed a single-step CVD approach (Fig. 3a) for the development of an edge-enriched 2D-$MoS_2$ thin film with high catalytic efficiency towards the HER. The CVD process was carried out on a wide range of substrates including a silicon wafer, graphite, and glassy carbon. During the synthesis, the total number of edge sites on $MoS_2$ and its surface area increased when smaller layered $MoS_2$ grew on large $MoS_2$ platelets in a perpendicular direction (Fig. 3b). The TEM images in Fig. 3c and d demonstrate the formation of vertically orientated layers, in which vertically aligned nanoflakes are grown on the petal site of $MoS_2$.[85]

In terms of wafer-scale production with low manufacturing cost and highly crystalline $MoS_2$, the atmospheric pressure

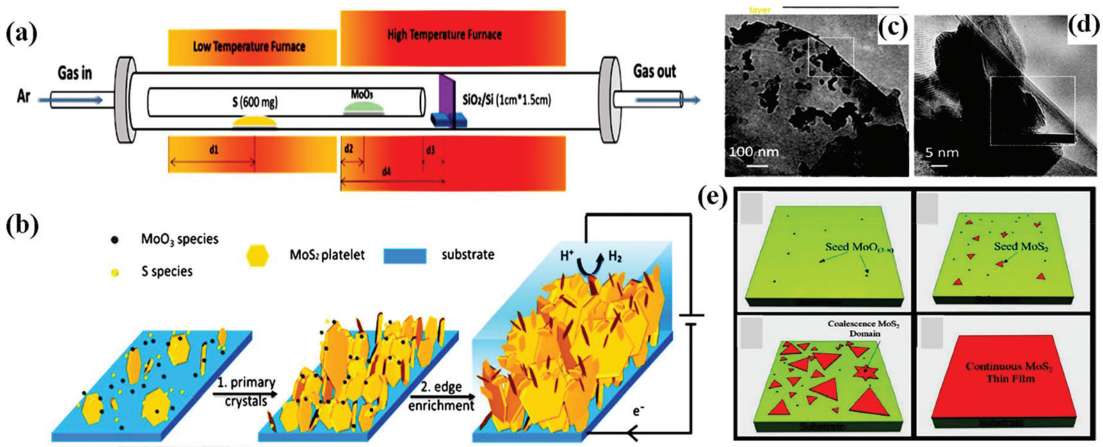

**Fig. 3** (a) Schematic representation showing the experimental CVD setup, (b) mechanistic demonstration of the edge enrichment of $MoS_2$, (c) and (d) TEM images of the petal site showing the nucleation of vertically aligned nanoflakes on the top-layer crystals. Reproduced from ref. 85. (e) Schematic illustration of monolayer $MoS_2$ growth on a Piranha-treated substrate. Reproduced from ref. 86.

chemical vapour deposition (APCVD) method has emerged as an excellent approach. Gnanasekar and his group developed a high-quality $MoS_2$ monolayer for the electrochemical hydrogen evolution reaction using a seed promoter-free APCVD method directly on an $SiO_2$ substrate. The CVD method mainly involves the transport and adsorption of the final growth species on a given substrate followed by the nucleation and future growth of new $MoS_2$. Initially, at a particular high temperature, the Mo precursors are reduced and are adsorbed on the arbitrary position of the substrate with the flow of carrier gas, which is further subjected to a sulfurization process, resulting in nucleated species. The as-obtained $MoS_2$ acts as a seed, which allows further growth of another $MoS_2$ thin film. The overall reaction procedure is depicted in Fig. 3e. From the experiment, the large scale high-quality $MoS_2$ possessed excellent HER properties.[86] However, using this method, it is very challenging to prepare $MoS_2$ crystals by controlling the number of layers due to the use of non-crystalline precursors, where it is difficult to control the number of layers of the product material during the reaction.

*3.1.2.2 Hydrothermal or solvothermal method.* Among the various synthetic methods, the hydrothermal process is preferred by many researchers because it can achieve high surface area, good-quality crystals and controlled morphological composition of the products. It is a growth method in which water and organic and inorganic solvents are used as the reaction medium dissolve the commonly used Mo and S precursor substances. The reaction generally involves the crystallization of a material under high pressure (1 MPa to 1 GPa) and high temperature (100–250 °C) conditions from an aqueous and organic solvent. This technique is very promising due to its safe and simple operation, mild conditions, high purity, low pollution, low cost and easy hybrid dispersion nature. The solvothermal synthesis technique of 2D-$MoS_2$ basically requires the use of an organic/inorganic sulfur source such as thioacetamide, thiourea and KSCN, and sodium molybdate, ammonium molybdate, and molybdenum trioxide as the Mo source. By controlling the reaction temperature and time, the size, crystallinity and morphology of the resultant 2D-$MoS_2$ can be modulated to some extent.[34,37,87] Muralikrishna and co-workers synthesized 2D $MoS_2$ nanosheets with high catalytic activity *via* a facile hydrothermal approach, which exhibited superior electrocatalytic HER activity.[88] The sulfur source used was thiourea, which acts as both a reducing agent and stabilizer, which stabilizes the defect-rich $MoS_2$ nanosheets. Under hydrothermal conditions, *i.e.*, high temperature and high pressure, firstly Mo(VI) present in $MoO_3$ is reduced to Mo(IV) under the influence of excess thiourea. Finally, the reduced Mo(IV) couples with the excess thiourea and undergoes a nucleation process and is converted to $MoS_2$ nanoparticles, which then grow into defect-rich nanosheets. The use of ammonia during the reaction procedure has a great advantage over the stacking of $MoS_2$ nanosheets and facilitates the production of thin nanosheets very easily. In another study, Swain *et al.* prepared crumpled-type exfoliated $MoS_2$ nanosheets under simple one-step hydrothermal conditions. It was also observed that without the inclusion of any surfactants, the hydrothermal technique is also responsible for the production of highly efficient morphological-oriented structured $MoS_2$ nanosheets.[89] In this regard, Swain *et al.* designed rose-like $MoS_2$ nanoflowers by employing a facile hydrothermal technique using only water as the solvent. The as-obtained $MoS_2$ exhibited like a rose-like nanoflower structure with a diameter of 500–800 nm. During hydrothermal treatment from the precursor salt solutions of Mo and S, firstly the $MoS_2$ nanoparticles self-aggregate and undergo a reduction in surface energy and get converted into partially monodispersed isolated $MoS_2$ microspheres. Under a prolonged hydrothermal process with an increase in temperature, petal-like nanosheets of $MoS_2$ are grown on the surface of the $MoS_2$ spheres, thus displaying a hierarchical rose-like $MoS_2$ nanoflower morphology.[90] Several studies have also reported that the introduction of the combined effect of both defects and S-vacancy results in superior catalytic activity. Li *et al.* employed a facile hydrothermal method for the synthesis of multilayered $MoS_2$ nanosheets in *N*,*N*-DMF using $(NH_4)_2MoS_4$ as both the Mo and S precursors. The as-obtained $MoS_2$ consisted of point-defect S-vacancies together with coordinated Mo regions, which reduced the free energy of hydrogen adsorption during the HER.[91]

### 3.2 Techniques for the synthesis of $MoS_2$-based 2D/2D heterostructures

The fabrication of $MoS_2$-based 2D/2D heterostructure composites with controllable nanostructured properties is a great challenge in the current research scenario. The techniques for the synthesis of $MoS_2$-based 2D/2D heterostructures are broadly categorized into two classes: (a) *ex situ* synthesis method and (b) *in situ* and one-pot synthesis method.[53,65] Among the various reports in the literature, only a few are discussed in the following section.

**3.2.1 *Ex situ* synthesis method.** The *ex situ* synthesis method is also known as the "self-assembly method", which plays a great role in the fabrication of $MoS_2$-based 2D/2D heterostructure composites. In this technique, two individual pre-synthesized 2D layered materials undergo the *ex situ* assembly method. The pre-synthesized components are synthesized through (i) exfoliation from their bulk samples through mechanical or chemical methods, (ii) solid-phase grinding, (iii) liquid-phase ultrasonic adsorption, (iv) hydrothermal treatment, and (v) calcination. Subsequently, each pre-synthesized 2D material is manually stacked through weak van der Waals interlayer interaction *via* the self-assembly process give rise to 2D/2D layered heterostructures. In *ex situ*-mediated 2D/2D heterostructure composites, the photo/electrocatalytic activity is mainly attributed to their interlayer distance and orientation of the superposition lattice of each 2D–2D material.[53,62,65]

It should be noted that in some cases, a single 2D material can be directly exfoliated from its bulk under the action of some solvent and exfoliation treatment, whereas in some cases, the neat material can be prepared from its molecular precursors directly. For example, Xiong *et al.* fabricated a 2D/2D $MoS_2/CdS$ heterojunction by employing an adsorption–calcination process, as shown in Fig. 4a. This method involved the preparation of neat 2D-$MoS_2$ from its commercial bulk counterpart through exfoliation, whereas neat CdS was prepared through the solvothermal–precipitation route followed by exfoliation to get an ultrathin nanosheet structure. Then, the two above-prepared neat materials were mixed through the adsorption process *via* sonication, and then further subjected to a calcination process (Ar atmosphere), which facilitates the close contact between the two components.[92] Similarly, Jeong *et al.* fabricated a black phosphorus (BP)@$MoS_2$ 2D/2D nanocomposite by mixing as-exfoliated BP and $MoS_2$ through the ball milling method followed by high energy ultrasonication.[93] Meanwhile, another type of 2D/2D nanojunction was constructed through the direct assembly strategy followed by the reflux method, in which $MoS_2$ nanosheets with 6 to 8 layers were prepared through a simple solvothermal method followed by exfoliation strategy, whereas $Bi_2WO_6$ nanosheets were prepared through a hydrothermal method, which were then dispersed in NMP (*N*-methyl-2-pyrrolidone) solvent *via* sonication followed by reflux. The large and close 2D/2D contact surface of the $Bi_2WO_6/MoS_2$ heterojunction is favorable for interfacial charge transfer. In heterojunction materials, the abundant reductive active sites and high electron conductivity are mainly dependent on the controlled S–Mo–S layer of $MoS_2$ nanosheets, which look like curled edges. It was observed that the controlled curled edges of $MoS_2$ possess a larger interlayer spacing (0.702 nm and 0.685 nm) compared to that of bulk $MoS_2$ (0.61 nm).[77]

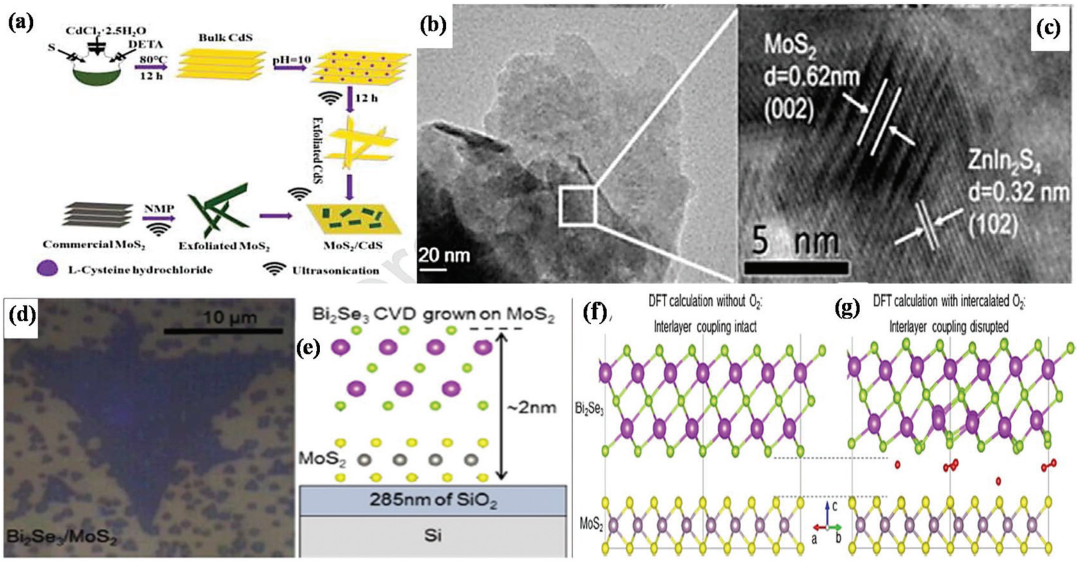

Fig. 4 (a) Strategy for the fabrication of $MoS_2/CdS$ heterojunctions. Reproduced with permission.[92] (b) SEM and (c) HRTEM images of $ZnIn_2S_4/MoS_2$ composite. Reproduced with permission.[95] (d) Optical image and (e) side-view diagram of $Bi_2Se_3/MoS_2$ heterostructure, (f) charge redistribution representation of the interlayer region and the interlayer coupling and (g) interlayer coupling with interlayer separation by $O_2$ molecule of $Bi_2Se_3/MoS_2$. Reproduced with permission.[96]

In addition, *ex situ* strategies are also regulated through ball milling and the mechanical grinding method. Li *et al.* developed a 2D/2D $C_3N_4/MoS_2$ heterojunction photocatalyst with a stable intrinsic crystal structure *via* a simple mechanical grinding method. They mixed an appropriate amount of commercial $MoS_2$ and g-$C_3N_4$ and put it on ball grinder for mechanical operation.[94] However, good interfacial contact was also achieved through the electrostatic self-assembly approach, considering the zeta potential value of each neat material. By following this strategy, Huang *et al.* designed a sheet-on-sheet 2D/2D $ZnIn_2S_4/MoS_2$ heterostructure, in which $MoS_2$ nanosheets were well connected with ultrathin sheets of $ZnIn_2S_4$. Briefly, initially, both pristine materials have negatively charged surfaces with a zeta potential value of −23.8 mV and −45.7 mV for the $MoS_2$ and $ZnIn_2S_4$ nanosheets, respectively. However, after treatment with poly(diallyldimethylammonium chloride) (PDDA), the negative surface of the $MoS_2$ nanosheets in the aqueous dispersion changed became positive with a zeta potential value of +36.5 mV. After the modification, strong electrostatic attraction occurred between the negatively charged $ZnIn_2S_4$ and positively charged PDDA-$MoS_2$, which provided the necessary condition for the development of a 2D/2D heterostructure with an intimate contact interface for efficient charge separation and migration. The sheet-on-sheet structure with large contact interface and individual clear fringes for neat $MoS_2$ and neat $ZnIn_2S_4$ in the 2D/2D $ZnIn_2S_4/MoS_2$ heterostructure is presented in Fig. 4b and c, respectively.[95]

Besides the above-mentioned methods, the transfer process in which a single 2D material originates from the CVD method is also treated as an *ex situ* method for the direct configuration of 2D/2D van der Waals heterostructures. Wang *et al.* developed a method for the direct growth of $MoS_2$ on h-BN by employing an *ex situ* path. The $MoS_2$/h-BN van der Waals heterostructure was prepared through a two-step poly(methyl methacrylate) (PMMA)-assisted transfer approach. The method involved the direct transfer of CVD-grown $MoS_2$ to a new $SiO_2/Si$ substrate containing h-BN to achieve a 2D/2D heterostructure.[68] It was noted that for the synthesis of more active 2D/2D van der Waals heterostructures, parameters such as the interlayer separation distance and stacking lattice orientation should be optimized. Therefore, Hennighausen *et al.* tuned the interlayer through the intercalation and deintercalation of diffusive atmospheric oxygen molecules. By regulating the atmospheric oxygen, the interlayer coupling in the 2D/2D $Bi_2Se_3$ heterostructure could be reduced under laser or thermal energy. The synthetic method involved the initial growth of an $MoS_2$ monolayer followed by the growth of $Bi_2Se_3$ on top of it through vapour phase chalcogenization and vapour phase deposition, respectively. The successful uniform and regular growth of one layer of $Bi_2Se_3$ on one layer of $MoS_2$ crystal on $SiO_2$ and the strong van der Waals epitaxial structure were clearly observed from the optical image (Fig. 4d) and side-view diagram (Fig. 4e), respectively. The DFT calculation, as shown in Fig. 4f and g, predicted the uniform charge redistribution in the interlayer region. The relatively small-sized $O_2$ molecules are easily intercalated in the interlayer region, as predicted by DFT calculation (Fig. 4g), which facilitates charge separation by tuning the interlayer coupling, thus making the material electronically independent.[96] Subsequently, Biroju and coworkers accomplished the synthesis of sequentially stacked atomic layers throughout the development of an $MoS_2$/graphene van der Waals solid through the wet transfer CVD method. In this case, a single layer of graphene was grown on three-four atomic layers of $MoS_2$ by mixing and matching various layers, resulting in a transparent flexible electrode, and its efficacy in the HER was demonstrated.[97]

### 3.2.2 *In situ* synthesis method.

In addition to the *ex situ* approach, an alternative technique has been implemented, which is commonly known as the "*in situ* growth method", for the fabrication of $MoS_2$-based 2D/2D heterostructures. The methods for the *in situ* growth of $MoS_2$-based 2D/2D heterostructure may be (i) a one-step growth method or multistep transformation approach, in which the direct growth of one 2D layered material occurs on the surface of primarily synthesized 2D-$MoS_2$ substrates or *vice versa* through various techniques such as wet chemical synthesis, chemical vapor deposition method (CVD), and nanoconfinement methods. (ii) Direct growth of $MoS_2$-based 2D/2D heterostructure composites. The experimental studies indicate that in some cases, during the synthesis of 2D-$MoS_2$-based 2D/2D heterostructure, firstly, anions from the Mo source, *i.e.*, $MoS_4{}^{2-}$ and $MoO_4{}^{2-}$, are generated and adsorbed on the other 2D material, and then reduced to $MoS_2$ upon the addition of the S source under heat treatment. Generally, epitaxial growth and direct growth are the two approaches employed for the *in situ* growth of 2D/2D heterostructures. From a number of experimental surveys, it has been deduced that among the various synthetic techniques, the CVD and wet chemical synthesis methods are the commonly used methods, resulting in distinct types of contagious interfaces together with potential catalytic application depending on the interface.[53,62,65]

For the CVD technique, a substrate and a volatile substance are required, in which one pre-synthesized 2D material is employed as the 2D substrate on which the volatile substances are exposed so that the other 2D materials can easily react or decompose for the growth of 2D/2D heterostructures. When the reaction is complete, volatile byproducts are produced, which are removed from the reaction system with the help of a gas flow. This is the most promising technique for the synthesis of hybrid materials based on the 2D/2D architecture.[53,65] Moreover, it has been observed that during the growth process, given that the precursors of both 2D materials coexist in the vapor phase, there may be a cross-contamination issue with the various elements present in the as-fabricated 2D/2D heterostructure. However, this issue can be mitigated through the two-step CVD growth strategy, in which two 2D composite layers are synthesized in two separate steps and the growth process on a metal substrate is found to be more effective. This method offers high-quality 2D/2D TMD heterostructures together with a pure phase, resulting in versatile applications in various fields.

Zhai *et al.* developed 2D-van der Waals heterostructures using $NiTe_2/MoS_2$ through a two-step *in situ* CVD growth method. The as-fabricated heterostructure possessed a better heterointerface and enhanced electronic and optoelectronic performances, which were found to be three orders greater compared to that of single 2D-$MoS_2$. The epitaxial growth of the van der Waals heterostructure is mainly attributed to the similar hexagonal symmetry of both 2D layered materials. In this case, firstly, by using the low-pressure chemical vapour deposition (LPCVD) strategy, $MoS_2$ monolayers are grown on $SiO_2$/Si substrates. It should be noted that the LPCVD method is easier and much more beneficial for designing high crystalline monolayer $MoS_2$ with a clean and triangular surface. After the formation of triangular $MoS_2$, it is employed as a substrate for the growth of an $NiTe_2$ layer, resulting in an $NiTe_2/MoS_2$ van der Waals heterostructure, in which the bottom $MoS_2$ layer and upper $NiTe_2$ thin film layer are vertically stacked with each other through weak van der Waals forces (Fig. 5a). Fig. 5b depicts the two-step CVD growth procedure for the synthesis of the $MoS_2/MoTe_2$ heterostructure. The vertical heterostructure of $NiTe_2$ on the monolayer of $MoS_2$ is depicted in the SEM image in Fig. 5c. According to the AFM image (Fig. 5d), the thickness of the upper $NiTe_2$ and bottom $MoS_2$ is 5.20 nm and 0.85 nm, suggesting the formation of five and single triple-layers comprised of $NiTe_2$ and $MoS_2$, respectively.[98]

Furthermore, it has been demonstrated that vertical bilayers with the strongest interlayer coupling and shortest interlayer spacing can be obtained based on the twisted stacking angles with equivalent crystallographic alignment in van der Waals heterostructures, such as A–A or A–B-type stacking. Due to this type of modulation in the interlayer coupling, the heterostructure exhibits superior optical and electrical properties, *i.e.*, it facilitates the interlayer transfer and migration of charge pairs, thus reducing the charge recombination more efficiently. Zhang *et al.* reported the epitaxial growth of an $MoS_2/WS_2$ heterostructure, in which $MoS_2$ films were grown on top of $WS_2$ through a two-step CVD growth approach in the A–A and A–B stacking fashion. The top and side atomistic views of the heterostructure are presented in Fig. 5e. In this case, $MoS_2$ is nucleated at the edges of $WS_2$ in a triangular shape with only 0° and 60° orientations with respect to the bottom $WS_2$ layer, maintaining the most stable A–A and A–B stacking configurations, respectively. According to the Raman spectra study, the A–B stacked bilayers had a strong lower breathing frequency mode than the A–A stacked bilayers, which possessed a shorter interlayer distance and stronger interlayer coupling.[99]

Further, Shi and co-workers designed a vertically stacked van der Waals heterostructure *via* the temperature-mediated selective growth of 2D-$MoS_2$ on 2D-$WS_2$ and *vice versa* using Au foil as the substrate material in the two-step CVD method.[100] Briefly, as shown in Fig. 5f, in the first step, the individual monolayer $MoS_2$ or $WS_2$ was grown on Au foil from its precursor element ($MoO_3$ or $WO_3$, respectively) under a low-pressure CVD method. In the second step, the as-prepared $MoS_2$/Au or $WS_2$/Au samples were subjected to further heat treatment in a furnace in the presence of the corresponding metal precursors for the subsequent preparation of the 2D/2D $MoS_2/WS_2$ heterostructure. The uniform distribution and vertical growth of $MoS_2$ or $WS_2$ (triangular domain) on $WS_2$/Au or $MoS_2$/Au were clearly observed from the SEM images (Fig. 5g and h), respectively. In contrast, Lee *et al.* proposed a novel method for the direct growth of $MoS_2$/graphene using the CVD technique in the presence of a UV/ozone-treated solid C-source, as illustrated in Fig. 5i. $MoO_3$ and sulfur powder were used as the $MoS_2$ precursors, while for the growth of graphene, 1,2,3,4-tetraphenylnaphthalene (TPN) was used as the precursor. Firstly, an $MoS_2$ monolayer was prepared using the molten-salt-assisted CVD method, resulting in the formation of an $MoS_2/SiO_2$/Si substrate, on which the graphene layer was grown. However, UV/ozone treatment of the spin-coated TPN

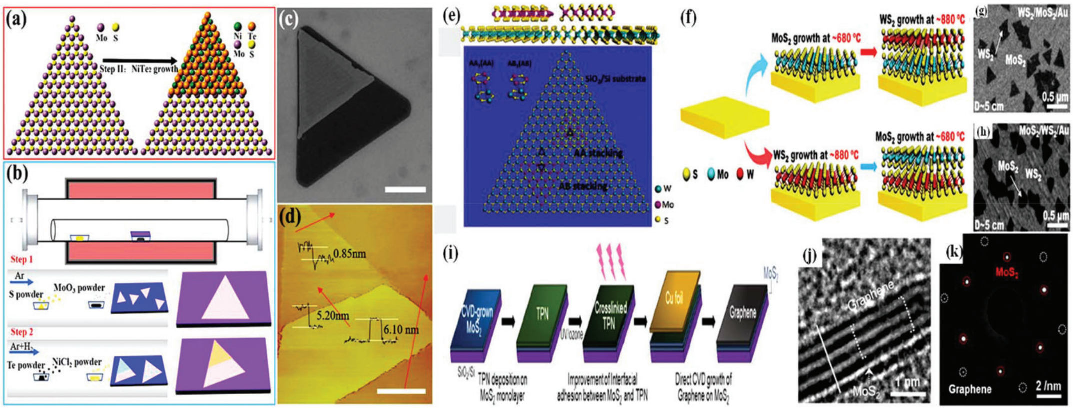
(a)
Mo S
Ni Te
Mo S
Step II: NiTe₂ growth
(b)
Step 1
Ar
S powder
MoO₃ powder
Step 2
Ar+H₂
Te powder
NiCl₂ powder
(c)
(d)
0.85nm
5.20nm
6.10 nm
(e)
AA.(AA)
AB.(AB)
SiO₂/Si substrate
AA stacking
AB stacking
W
Mo
S
(f)
MoS₂ growth at ~680 °C
WS₂ growth at ~880 °C
WS₂ growth at ~880 °C
MoS₂ growth at ~680 °C
S
Mo
W
(g)
WS₂/MoS₂/Au
WS₂
MoS₂
D~5 cm
0.5 μm
(h)
MoS₂/WS₂/Au
MoS₂
WS₂
D~5 cm
0.5 μm
(i)
CVD-grown MoS₂
TPN
UV/ozone
Crosslinked TPN
Cu foil
Graphene
MoS₂
SiO₂/Si
TPN deposition on MoS₂ monolayer
Improvement of interfacial adhesion between MoS₂ and TPN
Direct CVD growth of Graphene on MoS₂
(j)
Graphene
MoS₂
1 nm
(k)
MoS₂
Graphene
2 /nm

**Fig. 5** (a) Schematic illustration of the vertical stack and (b) two-step CVD growth process for $NiTe_2/MoS_2$ heterostructure. (c) SEM image depicting the vertical heterostructure of $NiTe_2/MoS_2$ on an $SiO_2$/Si substrate. (d) AFM images of vertical stacking region and interfacial region. Reproduced with permission.[98] (e) Atomic representation of vertically assembled A–A and A–B stacked (top and side views) $MoS_2/WS_2$ bilayers. Reproduced with permission.[99] (f) Schematic diagram representing the two-step CVD growth process. (g) and (h) SEM images of $WS_2/MoS_2$/Au and $MoS_2/WS_2$/Au, respectively. Reproduced with permission.[100] (i) Schematic representation showing the direct growth of graphene/$MoS_2$ heterostructure on $SiO_2$/Si substrate, (j) HRTEM image of graphene/$MoS_2$ heterostructure and (k) SAED image of $MoS_2$ monolayer (red circle) and graphene (white circle). Reproduced with permission.[101]

on $MoS_2/SiO_2/Si$ substrate increased the interfacial adhesion between the two layers, and the final growth of graphene occurred under Cu vapor when Cu foil was placed on the TPN-coated $MoS_2/SiO_2/Si$ substrate, resulting in the formation of the graphene/$MoS_2$ heterostructure. The successful growth of graphene layers on the monolayer $MoS_2$ and sharp interface between graphene and $MoS_2$ were confirmed from the cross-sectional TEM image (Fig. 5j). Furthermore, the SAED pattern (Fig. 5k) confirmed the clean diffraction spots for both $MoS_2$ and graphene in the graphene/$MoS_2$ heterostructure, suggesting that the 2D/2D heterostructure is suitable for application in an ultrathin electronic device with high surface-sensitive properties.[101]

Besides the CVD method, the *in situ* process for the synthesis of 2D/2D heterostructures can also be mediated through the hydrothermal technique. Ji *et al.* modified 2D-$CeO_2$ on 2D-$MoS_2$ nanosheets through an *in situ* facile hydrothermal technique to design a new 2D/2D $MoS_2/CeO_2$ heterojunction, which possessed abundant reactive centers for degradation reactions.[102] Throughout the reaction, the $Ce^{4+}$ ions from 2D-$CeO_2$ generated sufficient oxygen vacancies by utilizing photoexcited charge carriers and acted as redox centers. In this case, firstly, 2D $CeO_2$ nanosheets were prepared *via* the hydrothermal method followed by calcination, and then introduced to the Mo and S precursors through the hydrothermal process, resulting in the formation of 2D/2D $MoS_2/CeO_2$. The morphological characterization *via* TEM and HRTEM of 2D/2D $MoS_2/CeO_2$ indicated that both 2D nanosheets were uniformly combined, in which the 2D-$CeO_2$ nanosheets were located on the 2D-$MoS_2$ nanosheets in a vertical and lateral fashion. Furthermore, Yuan *et al.* developed face-to-face 2D/2D black phosphorus (BP)/$MoS_2$ through the solvothermal method, in which $MoS_2$ nanosheets were homogeneously dispersed on the surface of BP nanosheets. It was observed that the interaction occurred between the precursors of $MoS_2$ and the oxygen present in the exfoliated BP nanosheets, which exhibited a large intimate contact interface and abundant exposed edges for superior catalytic activity.[103]

Besides the face-to-face heterostructure, the *in situ* synthesis method is also responsible for the formation of highly efficient 2D/2D heterostructure materials with electrostatic interaction between them. By combining electrostatic self-assembly chemistry with the *in situ* hydrothermal strategy, Nayak *et al.* constructed an $MoS_2$/Ni–Fe LDH nanocomposite.[104] Particularly, 2D-$MoS_2$ nanosheets underwent a nucleation and growth process on the edge-shared $MO_6$ octahedron site (positively charged surface) provided by 2D-LDH, resulting in the formation of 2D/2D $MoS_2$/Ni–Fe LDH. The overall growth process is governed through the electrostatic self-assembly and $O_2$ vacancies in the LDH nanosheets, which effectively co-ordinate with the $Mo^{4+}$ and $S^{2-}$ ions during the *in situ* hydrothermal reaction. Interestingly, both the exfoliation of strongly bonded positive layers of LDH and the growth of $MoS_2$ nanosheets on the positively charged surface of the exfoliated LDH take place in one step during the hydrothermal reaction. Swain *et al.* developed a hierarchical structure with a 2D/2D contact heterojunction in which the crumpled sheets of $MgIn_2S_4$ flowers were covered with petal-like $MoS_2$ nanosheets through S–S linkages at the interface.[90] As illustrated in Fig. 6a, under hydrothermal treatment, the $MoS_2$ nanopetals derived from the $MoS_2$ nanoflowers under ultrasonication mixed with the precursor salt solution (Mg, In, and S) of $MgIn_2S_4$, resulting in the formation of an $MoS_2/MgIn_2S_4$ marigold flower-like morphology. The resulting 2D/2D heterojunction is constructed in

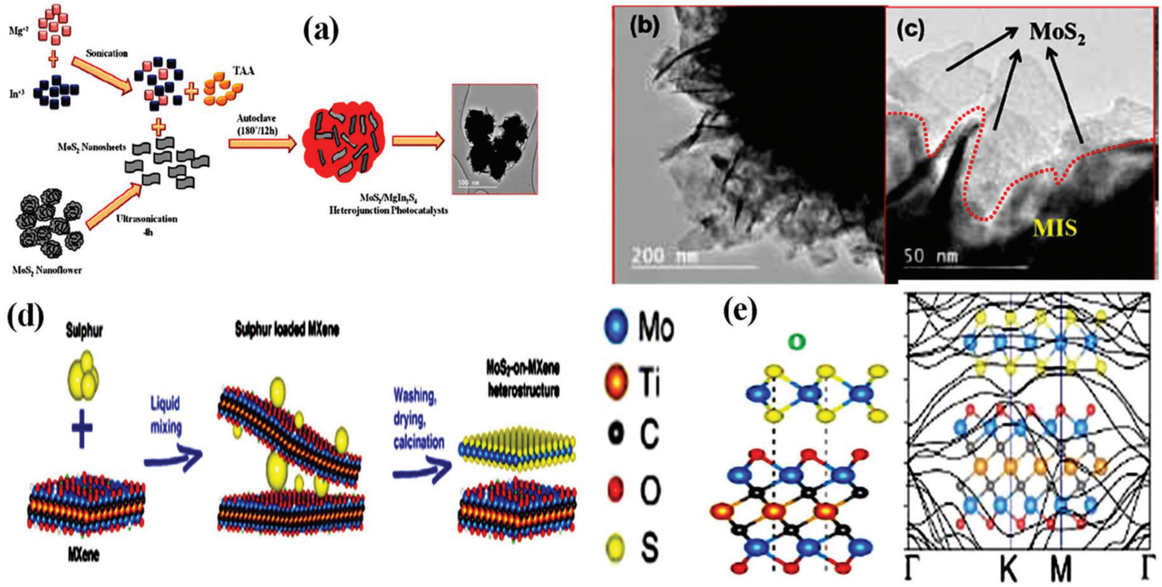

Fig. 6 (a) Schematic diagram showing the growth mechanism and (b) and (c) corresponding HRTEM images of $MoS_2/MgIn_2S_4$ heterojunction photocatalyst. Reproduced with permission.[90] (d) Schematic representation of the fabrication of $MoS_2$/MXene hybrids and (e) structural stacking patterns and electronic band structure of $MoS_2/Mo_2TiC_2O_2$. Reproduced with permission.[105]

such a way that both neat counterparts are tightly joined with each other in a zigzag face-to-face and face-to-edge contact, providing a large number of exposed unsaturated S active sites for the photocatalytic reaction. The TEM images (Fig. 6b and c) of the $MoS_2/MgIn_2S_4$ heterojunction indicate the wrapping of $MoS_2$ nanosheets around the micro-sized petals of the $MgIn_2S_4$ flowers.

Furthermore, highly active $MoS_2$-based 2D/2D heterostructures can also be achieved *via* the partial replacement of S in 2D-$MoS_2$ with another anion such as phosphide and carbide having a similar atomic radius or the addition of S to another non-$MoS_2$-based material.[105] 2D MoP/$MoS_2$ heterostructure nanosheets were constructed by Wu and coworkers, in which the S present in $MoS_2$ underwent rational substitution with P. Typically, $MoS_2$ nanosheets were evenly distributed and grown on CC cloth under hydrothermal treatment, and then MoP was obtained on the $MoS_2$ nanosheet template under phosphorization treatment. However, the partial replacement of S with P should be controllable so that a part of the $MoS_2$ phase remains in the final product to maintain the 2D/2D MoP/$MoS_2$ sheet-like heterostructure. It was demonstrated that the as-fabricated 2D/2D heterostructure possessed rich active sites and good conductivity.[106] In another study, Chen *et al.* designed a 2D $MoS_2$-on-MXene heterostructure *via* the *in situ* sulfidation of a molybdenum-containing 2D-Mxene ($Mo_2TiC_2T_x$) material (Fig. 6d). In the $Mo_2TiC_2T_x$ structure, one layer of Mo atoms is present on the surface of the $Mo_2TiC_2T_x$ MXene, and thus a part of the surface Mo–O pattern can be controllably transformed into an Mo–S motif on the MXene surface under *in situ* sulfidation, resulting in the formation of an $MoS_2/Mo_2TiC_2T_x$ heterostructure with intimate interfacial interactions. The schematic mechanism suggests that under the liquid mixing process, sulfur-incorporated MXene layers are initially derived, which are further subjected to heating in an inert atmosphere, producing the final product followed by the transformation of Mo–O to Mo–S and removal of residual S simultaneously. The stable structural and electronic properties of the resulting heterostructure were depicted from the computational investigation, as shown in Fig. 6e. According to the position of the Mo and S atoms in $MoS_2$ with respect to O and Ti in $Mo_2TiC_2O_2$, respectively, it was deduced that the integration between $MoS_2$ and $Mo_2TiC_2O_2$ resulted in enhanced conductivity, which is suitable for application in Li-ion batteries.[105]

#### 3.2.3 One-pot synthesis method.

The one-pot synthesis method, also known as one-step synthesis, is another exciting *in situ* advance technique used for the fabrication of 2D/2D-based heterostructures. This process is more advantageous over the two abovementioned methods, *i.e.*, *ex situ* and *in situ* synthesis methods, which proceed through two or more than two complicated processes. Thus, the involvement of these complicated steps limits the industrial utilization of the resulting hybrids. In contrast, the main advantage of the one-pot technique is its time-saving behavior. In the one-pot method, the precursor salt solutions of both 2D materials are combined in one step, *i.e.*, the individual salt precursors are treated in one step, resulting in the formation of 2D/2D products.[65,107] Zhang and coworkers reported the synthesis of an $MoS_2/CdIn_2S_4$ 2D/2D flower-like heterojunction *via* a cost-effective one-pot self-assembly hydrothermal method. The intimate contact between $MoS_2$ and $CdIn_2S_4$ nanosheets mainly originates from the electrostatic attraction developed between the negatively charged $MoS_2$ surface with Cd and In ions in $CdIn_2S_4$ during the one-pot reaction.[108] Further, Fu and coworkers reported a unique method to achieve strong interfacial coupling between $MoS_2$ and g-$C_3N_4$ ultrathin van der Waals layers, involving self-assembly followed by thermal treatment. The reaction mechanism is illustrated in Fig. 7a. In this case, initially, the molybdenum ($Na_2MoO_4$) and g-$C_3N_4$ (dicyandiamide) precursors undergo a self-assembly process in acid solution, resulting a layer-by-layer structure, which is then softly ground with sodium sulphate solution to obtain a ground mixture. Consequently, the layered complex is uniformly coated on the $Na_2SO_4$ crystal, which is subjected to thermal processing, resulting in the formation of an ultrathin $MoS_2$/g-$C_3N_4$ van der Waals layer heterostructure. Briefly, the $MoS_2$ sheet originates from the reaction of $MoO_3$ with S *via* the thermal reaction of either the surface sulphate radical, which releases S or $H_2S$, or the precursors of g-$C_3N_4$, whereas the g-$C_3N_4$ ultrathin layer is developed on $MoS_2$ due to the polymerization of dicyandiamide. The DFT study revealed that through the abovementioned synthetic method, strong electronic coupling is created between Mo of $MoS_2$ and the N atom in g-$C_3N_4$ in $MoS_2$/g-$C_3N_4$ which is highly beneficial for its electrocatalytic performance.[109] Similarly, Dong and coworkers constructed an S-doped g-$C_3N_4/MoS_2$ 2D/2D face-to-face heterojunction through the hydrothermal-polymerization method, as depicted in Fig. 7b.[110]

To date, the exploration of the one-pot CVD process for the controlled synthesis of 2D/2D hybrid materials has rarely been discussed although this method is very scalable, versatile and time-saving. In the literature, only a few works have been reported on the one-pot CVD method towards the synthesis of hybrid materials. Yu and co-workers proposed a one-pot CVD strategy for the successful fabrication of $MoS_2$ microflowers on $VS_2$ microflakes by using suitable precursors on macroporous carbon fiber paper as the substrate under atmospheric pressure, and the reaction was performed in a one-temperature-zone furnace.[111] The procedure for the fabrication of the $MoS_2/VS_2$ hybrid is schematically illustrated in Fig. 7c. Typically, the metal precursors are positioned side-by-side, whereas the S element is placed at an upstream position in the quartz boat together with CFP in the middle of the furnace. The uniform growth of the $MoS_2/VS_2$ hybrids on the CFP was achieved by increasing the temperature to 800 °C under the flow of a gas mixture. The SEM images of the $MoS_2/VS_2$ hybrid at different magnifications (Fig. 7d–f) demonstrated the uniform distribution and full coverage of $MoS_2$ on the $VS_2$ microflakes. By modulating the temperature from low to high, they predicted that the $VS_2$ nanoflakes are derived initially at a lower temperature, and later with an increase in the reaction temperature (high temperature), $MoS_2$ microflowers grow on

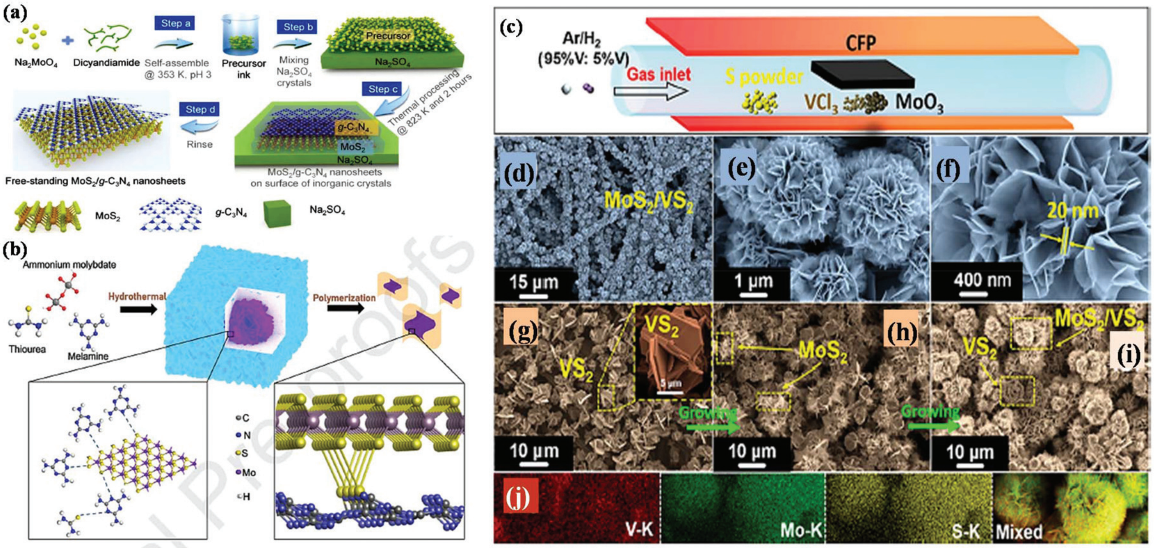
(a)
Na$_2$MoO$_4$
Dicyandiamide
Step a
Self-assemble @ 353 K, pH 3
Precursor ink
Step b
Mixing Na$_2$SO$_4$ crystals
Precursor
Na$_2$SO$_4$
Step c
Thermal processing @ 823 K and 2 hours
g-C$_3$N$_4$
MoS$_2$
Na$_2$SO$_4$
MoS$_2$/g-C$_3$N$_4$ nanosheets on surface of inorganic crystals
Step d
Rinse
Free-standing MoS$_2$/g-C$_3$N$_4$ nanosheets
MoS$_2$
g-C$_3$N$_4$
Na$_2$SO$_4$
(b)
Ammonium molybdate
Thiourea
Melamine
Hydrothermal
Polymerization
C
N
S
Mo
H
(c)
Ar/H$_2$ (95%V: 5%V)
Gas inlet
CFP
S powder
VCl$_3$
MoO$_3$
(d)
MoS$_2$/VS$_2$
15 µm
(e)
1 µm
(f)
20 nm
400 nm
(g)
VS$_2$
VS$_2$
5 µm
10 µm
Growing
MoS$_2$
(h)
10 µm
Growing
VS$_2$
MoS$_2$/VS$_2$
(i)
10 µm
(j)
V-K
Mo-K
S-K
Mixed

**Fig. 7** (a) Schematic illustration of the synthetic strategy for free-standing MoS$_2$/g-C$_3$N$_4$ vdW layers. Reproduced with permission.[109] (b) Schematic representation of the synthesis of MCN nanocomposites *via* the hydrothermal-polymerization method. Reproduced with permission.[110] (c) Schematic diagram representing the one-pot CVD process for the preparation of the MoS$_2$/VS$_2$ hybrid, (d–f) SEM images at different magnifications observed for MoS$_2$/VS$_2$ hybrid, (g–i) TEM images of the MoS$_2$/VS$_2$ hybrid at different temperatures and (j) EDX colour elemental mapping of the MoS$_2$/VS$_2$ hybrid. Reproduced with permission.[111]

VS$_2$. Fig. 7g–i illustrate the morphological evolution of the MoS$_2$/VS$_2$ hybrid at different temperatures. Depending on the temperature, four primary chemical reactions occur, as illustrated by eqn (1)–(4). The successful synthesis and the near-surface elemental distribution of the VS$_2$/MoS$_2$ hybrid can be clearly observed in Fig. 7j.

$$8H_{2(g)} + S_{8(g)} \rightarrow 8H_2S_{(g)}, \quad T = \sim 150\,°C - 180\,°C \tag{1}$$

$$2VCl_{3(s)} \rightarrow VCl_{4(g)} + VCl_{2(s)}, \quad T = \sim 270\,°C - 300\,°C \tag{2}$$

$$\begin{gathered} 2H_2S_{(g)} + VCl_{4(g)} \rightarrow VS_{2(s)} + 4HCl_{(g)}, \\ T = \sim 270\,°C - 300\,°C \end{gathered} \tag{3}$$

$$\begin{gathered} MoO_{3(s)} + 3H_2S_{(g)} \rightarrow MoS_{2(s)} + S_{(s)} + 3H_2O, \\ T = 700\,°C - 750\,°C \end{gathered} \tag{4}$$

In addition to the abovementioned report, Woods *et al.* synthesized an MoS$_2$/WS$_2$-based 2D/2D van der Waals heterostructure *via* one-pot CVD followed by metallic seed layer growth under sulfurization treatment.[112] It should be noted that the transition between the vertical and horizontal structure can be controlled by controlling the thickness of the seed-layer, and the horizontal orientation in the 2D/2D hybrid can be derived by using a metallic seed layer thinner than 3 nm. The authors demonstrated a horizontally oriented MoS$_2$/WS$_2$ stacked layered heterostructure by selecting a goldilocks metallic seed layer with a thickness of 1 nm. The growth procedure of MoS$_2$/WS$_2$ involves the sequential magnetron sputtering of W and Mo on an Si/SiO$_2$ substrate followed by sulfurization. The completion of sulfurization was confirmed by the change in colour from blue to light green, which completely fulfils the defined patterning of the MoS$_2$/WS$_2$ film.

## 4. Emerging photo/electrocatalytic applications of 2D-MoS$_2$ and MoS$_2$-based 2D/2D heterostructures

Considering the demand for nanomaterials towards energy and environmental applications, 2D-MoS$_2$ serves as an excellent material with important roles in the field of electrocatalysis and photocatalysis and contributes to energy production such as hydrogen evolution, ammonia generation, and CO$_2$ reduction. In terms of photocatalysis, on going from bulk 3D structured MoS$_2$ to 2D MoS$_2$, the band gap increases as it changes from indirect to direct, thus decreasing the possibility of electron hole recombination. In contrast, in the field of electrocatalysis, to achieve a superior electrocatalytic performance, the interfacial structure of 2D-MoS$_2$ plays the pivotal role. Again, studies have suggested that the photo/electro-activity of 2D-MoS$_2$ is mainly attributed to its high stability, broad absorption capacity, number of layers and presence of exposed active sites originating from the unsaturated coordinated S atoms (dangling S bond) and Mo edges.[7,32,45,113–120] However, although it is considered as one of the strategic materials in the field of photo/electrocatalysis, its low electrical conductivity, small surface area and restacking issues based on the number of layers limit its catalytic application as a single material.[32,45,51,121] Hence, different approaches such as exfoliation, doping, and formation of hybrid heterostructures and composites have been developed to minimize the drawbacks associated with $MoS_2$. Among the different approaches, the development of hybrid structures regarding $MoS_2$-based 2D/2D composite materials is one of the latest research trends. Here, in the application part, we present a brief overview of the energy and environmental applications of the recently reported 2D $MoS_2$ and $MoS_2$-based 2D/2D heterostructures.

### 4.1 Hydrogen evolution

To achieve a post-fossil fuel regime, molecular hydrogen is considered as environmentally friendly clean energy and also regarded as a promising alternative for future energy sustainability. In the recent literature, the production of hydrogen through very promising and convenient methods such as $H_2O$ splitting catalyzed by various catalysts is considered a novel approach.[3,5,6,73,76,122–126] Moreover, $H_2O$ can be split into hydrogen over 2D-$MoS_2$ both photocatalytically and electrocatalytically, as summarized in the following section.

**4.1.1 Electrocatalytic $H_2$ evolution.** The electrochemical water splitting reaction is regarded as another promising and efficient approach that can produce hydrogen fuel in high purity by utilizing electrical energy and water. The electrochemical hydrogen evolution reaction (HER) is an environmentally benign and cost-effective method that mainly occurs in different electrode-electrolytic systems. Currently, $MoS_2$ is regarded as the most promising electrocatalyst and widely investigated for the HER process.[116,127,128] Generally, the HER can be studied under both acidic and alkaline reaction conditions, and in both cases, it involves three reaction steps, which are governed by two mechanistic pathways, *i.e.*, the Volmer–Heyrovsky and Volmer–Tafel mechanisms. The first step is the Volmer or discharge step, which involves the adsorption of a hydrogen ion ($H_{ads}$) on the electrode surface, resulting from the coupling reaction between the electrons with a proton (in acidic condition) and a water molecule (in alkaline medium). After the adsorption of the hydrogen ion, the Volmer step is followed either by the Heyrovsky reaction or the Tafel reaction step for the evolution of molecular hydrogen depending on the experimental reaction conditions. When the two adsorbed hydrogen atoms followed by one electron are combined at the electrode surface, then it follows the Tafel reaction step, and when $H_2$ gas is generated from the coupling of one adsorbed hydrogen atom with one proton by up taking one electron, then the mechanistic pathway is known as the Heyrovsky step.[116,127] All the reaction steps in both acidic and alkaline conditions are illustrated in eqn (5)–(10) as follows:

**Acidic medium:** $2H_{(aq)}^{+} + 2e^{-} \rightarrow H_{2(g)}$

$$H_3O^+ + e^- \rightarrow H_{ads} + H_2O \text{ (Volmer)} \tag{5}$$

$$2H_{ads} \rightarrow H_2 \text{ (Tafel)} \tag{6}$$

$$H_3O^+ + H_{ads} + e^- \rightarrow H_2 + H_2O \text{ (Heyrovsky)} \tag{7}$$

**Alkaline Medium:** $2H_2O + 2e^{-} \rightarrow H_{2(g)} + 2OH_{(aq)}^{-}$

$$2H_2O + 2e^- \rightarrow 2H_{ads} + 2OH^- \text{(Volmer)} \tag{8}$$

$$2H_{ads} \rightarrow H_2 \text{ (Tafel)} \tag{9}$$

$$H_{ads} + H_2O + e^- \rightarrow H_2 + OH^- \text{(Heyrovsky)} \tag{10}$$

Moreover, the overall HER reaction mechanism greatly depends on the Gibb's free energy of the adsorbed hydrogen atom ($\Delta G_{H^*}$) due to the involvement of $H_{ads}$ in both the Volmer–Heyrovsky and Volmer–Tafel steps, and hence the rate-limiting step is the adsorption of a hydrogen atom.[127] According to DFT analysis, it has been deduced that the weak and strong adsorption process of H atoms on the active sites of the surface of the electrode greatly affects the effective adsorption (Volmer step) of a hydrogen atom and desorption (Tafel or Heyrovsky steps) of the hydrogen molecule, respectively. Thus, the HER process mainly prefers a catalyst possessing a moderate hydrogen binding capacity with a $\Delta G_{H^*}$ value close to zero. By using DFT calculation, the Gibb's free energy[36,73,130] for the chemisorbed hydrogen can be calculated by combining the binding energy with the thermal calculations using eqn (11).

$$\Delta G_{H*} = \Delta E_{H*} + \Delta E_{ZPE} - T\Delta S_H \tag{11}$$

where $\Delta E_{H^*}$ is the differential chemisorption energy/binding energy of hydrogen, and $\Delta E_{ZPE}$ and $\Delta S_H$ are the difference in zero-point energy and difference in entropy between the adsorbed state and the gas phase, respectively.

The volcano plot, as shown in Fig. 8, predicts the $\Delta G_{H^*}$ of some metals together with $MoS_2$, where it can be found that $MoS_2$ has similar properties to the well-known Pt noble metal.[129,131] Hence, in recent decades, the low-cost $MoS_2$ has opened an exciting area of research for the HER. Studies revealed that bulk $MoS_2$ with an inert basal plane has very poor catalytic activity, which is attributed to its limited active sites and low conductivity. In the study by Peng *et al.*, the $\Delta G_{H^*}$ on 2H-$MoS_2$ was calculated to be 2.18 eV, which is a slight deviation from its optimal value, *i.e.*, $\Delta G_{H^*}$ = 0,

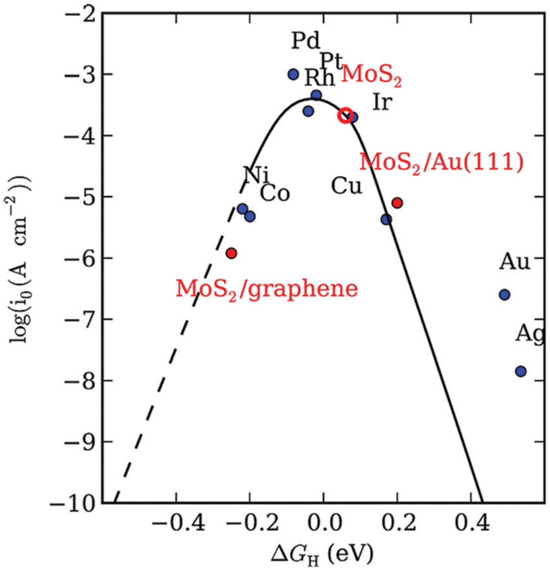

**Fig. 8** Volcano plot of various elements with respect to $\Delta G_{H^*}$. Reproduce from ref. 129.

suggesting that the basal plane of bulk $MoS_2$ is slightly inactive towards the HER.[130] In contrast, single and few-layer 2D $MoS_2$ with abundant unsaturated S active sites exhibit superior electrocatalytic activity.

The hydrogen coverage (ratio of hydrogen to sulfur atoms) on the top surface of the S-layers of $MoS_2$ was found to be 1/16. Moreover, the $\Delta E_{H^*}$ of the H-atom on the surface of $MoS_2$ can be defined by eqn (12).

$$\Delta E_{H^*} = E(MoS_2 + H) - E(MoS_2) - \frac{1}{2}EH_2 \quad (12)$$

where $E(MoS_2 + H)$, $E(MoS_2)$ and $EH_2$ represent the total energy corresponding to $MoS_2$ with one adsorbed H-atom on its surface, pure $MoS_2$ and molecular gaseous hydrogen, respectively.[130]

In 2005, Hinnemann and co-workers performed seminal work on $MoS_2$ towards the HER and reported that the edge of Mo $(10\bar{1}0)$ in $MoS_2$ is very active for the HER due to its low $\Delta G_{H^*}$ value. DFT studies predicted that the binding energy towards $H^+$ for $MoS_2$ is +0.08 eV, which is close to that of noble metals such as Pt, at only its edge site. However, its catalytic activity is somehow limited given that the basal plane being relatively inert because it is less conducting although the exposed S edges are the active sites for electron transfer.[132] Specifically, the defected S-edges play an important role in the HER for $MoS_2$. Typically, the HER activity of $MoS_2$ mainly depends on its size, edge active sites and number of layers. Thus, it is necessary to engineering $MoS_2$ with efficiently exposed unsaturated S-sites to obtain electrocatalysts with high HER activity.

Interestingly, Kong and his group introduced more freshly exposed active sites on 2D $MoS_2$ by engineering nanosized $MoS_2$.[133] The additional active sites are beneficial towards the intermediate adsorption of H, dramatically boosting the HER performance of 2D-$MoS_2$ in both acidic and alkaline electrolytic solution. As illustrated in Fig. 9a–d, by employing a simple annealing method, the old molybdenum and sulfur atoms (marked area) present in 2D-$MoS_2$ underwent a vaporization treatment and were replaced with fresh inner active edges with no alteration in the 2D structure of $MoS_2$. Consequently, the new 2D-$MoS_2$ possessed a greater density of under-coordinated S sites, exhibiting an enhanced ECSA and mass-normalized activity together with superior durability, and thus significantly improved HER activity. Upon heat treatment, the current density of the engineered 2D-$MoS_2$ reached up to 440 mA $cm^{-2}$ at a more positive onset potential compared that required for pristine $MoS_2$. Besides engineering the edges of $MoS_2$ through annealing treatment, designing defect-rich $MoS_2$ through hydrothermal treatment on a substrate is another strategy for establishing highly exposed edge sites. Xie *et al.* constructed defect-engineered $MoS_2$ catalysts with a controllable thickness, in which ultrathin nanosheets of $MoS_2$ were vertically aligned to construct a nanowall structure.[134] This $MoS_2$ nanowall catalyst exhibited a high current density of 310 mA $cm^{-2}$ at $\eta$ = 300 mV with a low onset over potential of 85 mV. Its superior catalytic performance is attributed to its freestanding vertical channels, which are beneficial for ion penetration, and the presence of a rough surface together with highly exposed active edges. Nevertheless, it is still a challenge to design 2D-$MoS_2$ with rational and controllable active sites. Accordingly, various strategies such as surface modification, morphological variation, phase and structure control, and fabrication of hybrid materials have been employed to increase the intrinsic activity and electrical conductivity of $MoS_2$, thus increasing its active sites. Among

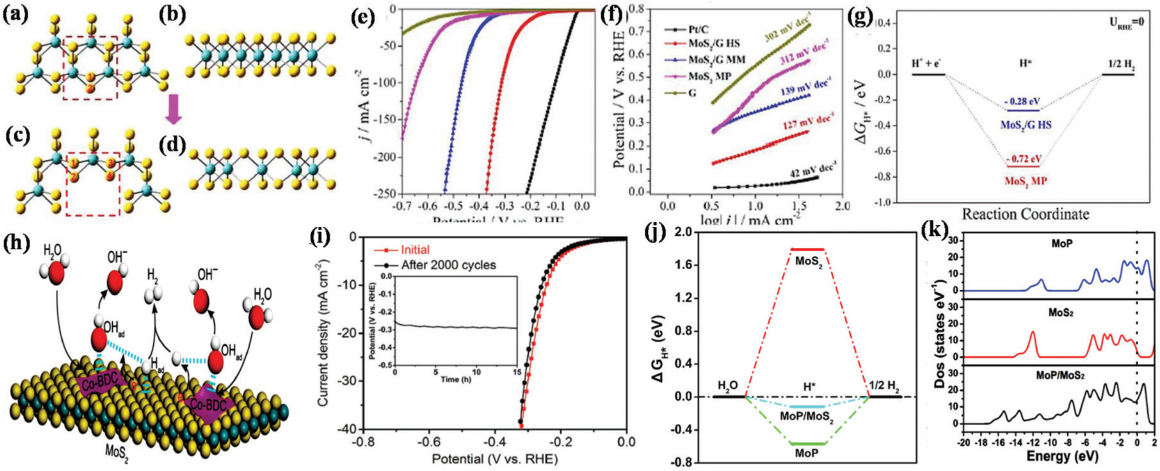

Fig. 9 Structural representation of the edge of pristine $MoS_2$ nanosheets in (a) top and (b) side views, and structural model of annealed $MoS_2$ nanosheets in (c) top and (d) side views (Mo and S atoms are represented by blue and yellow balls, respectively). Reproduced with permission.[133] (e) Polarization graph and (f) corresponding Tafel slope of various catalysts together with commercial Pt/C electrode in 1.0 M KOH and (g) hydrogen adsorption free energy plot for neat $MoS_2$ MP and $MoS_2$/GHS. Reproduced with permission.[73] (h) Illustration of the catalysis mechanistic pathway for alkaline-mediated HER over Co-BDC/$MoS_2$ hybrid, (i) polarization curves and chronopotentiometric response (inset) of Co-BDC/$MoS_2$. Reproduced with permission.[134] (j) Free-energy diagram for the HER and (k) calculated total electronic density of states for MoP, $MoS_2$ and MoP/$MoS_2$ heterostructures. Reproduced with permission.[106]

the various achievements, here we only focus on the use of hybrid materials through hierarchical structures based on 2D/2D heterostructures. To date, a large number of HER studies has been reported on 2D $MoS_2$-based 2D/2D heterostructures and few these studies of are detailed here.

Yu and co-workers established an $MoS_2$/graphene 2D/2D hetero-layered electrocatalyst towards electrocatalytic HER using both acidic (0.5 M $H_2SO_4$) and alkaline (1.0 M KOH) electrolytic solution and observed better HER activity in the former.[73] According to the LSV data, it was deduced that a current density of 10 mA is achieved for the $MoS_2$/graphene heterostructure at an overpotential of only 180 mV in acidic condition and 183 mV in alkaline solution (Fig. 9e), which is much lower than that obtained for neat $MoS_2$, *i.e.*, overpotential of 383 mV in acidic solution and 436 mV in alkaline solution, respectively. Furthermore, the catalytic performance toward the HER was evaluated through the Tafel slope, which was found to be 79 mV $dec^{-1}$ and 127 mV $dec^{-1}$ for the $MoS_2$/graphene heterostructure in acidic and alkaline condition (Fig. 9f), and the corresponding Tafel slope value obtained for the neat $MoS_2$ was about at 219 mV $dec^{-1}$ and 312 mV $dec^{-1}$, respectively. The superior HER performance of 2D/2D $MoS_2$/G HS was due to the formation of an intimate face-to-face contact through the alternating layer-by-layer arrangement between 2D-$MoS_2$ nanosheets and 2D-graphene, which led to more unsaturated atomic edge active sites contacting with the electrolyte and abundant defects between the 2D/2D interface of $MoS_2$ and graphene. This layer-by-layer arrangement also has a great influence on the electronic state, which favoured the transfer and separation of charges, thus improving the electronic conductivity at the coupled interface. The increase in the number of edge active sites arose from the expanded interplanar distance (1.104 nm) for $MoS_2$/graphene compared to that of $MoS_2$ (0.615 nm), which is beneficial for the adsorption and desorption of hydrogen at the electrode electrolyte interface. The experimental study revealed that the 2D/2D $MoS_2$/graphene HS exhibited superior wettability upon exposure to the electrolyte, which is beneficial for the availability and participation of more active sites in the HER. The smaller contact angle between $MoS_2$ and graphene in the 2D/2D heterostructure than $MoS_2$ improved the electronic conductivity at the coupled interface, facilitating the easy transfer and separation of charges at the interface. The high HER performance was also predicted by DFT studies through the three-state diagram (Fig. 9g) for the non-expanded pristine $MoS_2$ and interlayer-expanded 2D/2D $MoS_2$/G heterostructures. According to DFT, the $\Delta G_{H^*}$ (a powerful parameter for evaluating the adsorption and desorption process) was −0.72 eV for $MoS_2$ and −0.28 eV for the 2D/2D heterostructure, where the lower potential suggests a lower energy barrier for the fast release and adsorption of hydrogen in the heterostructure, thus improving the rate of the HER.

Inspired by some theories, Zhu and co-workers introduced a 2D-MOF (Co-BDC)/$MoS_2$ interface for alkaline HER (1 M KOH solution), in which Co-BDC with the optimum binding strength to $H_2O$ and hydroxyl promoted the sluggish water dissociation rate, while $MoS_2$ enhanced the production and adsorption of hydrogen atoms at the hybrid interface.[135] Importantly, the introduction of Co-BDC (acts as an electron donor) in $MoS_2$ not only improved the alkaline HER, but also induced a partial phase transfer from 2H to 1T, which lowered the additional energy barrier. Fig. 9h illustrates the overall mechanism for the alkaline HER, which proceeds through the adsorption of hydroxyl, $H_2O$ and H* followed by the dissociation and desorption of $H_2O$ and $H_2$ molecules, respectively, on the 2D-MOF (Co-BDC)/$MoS_2$ hybrid nanosheets. The aforementioned electrocatalyst achieved an excellent current density at a very low overpotential. In addition, the long-term durability of the 2D-MOF (Co-BDC)/$MoS_2$ hybrid was assessed to verify its stability in alkaline solution. Both the cyclic voltammetry and chronoamperometry curves (Fig. 9i) substantiating the excellent stability of the Co-BDC/$MoS_2$2D/2D hybrid nanosheet sample, even after 2000 cycles.

However, in some cases, the HER process is performed in neutral medium to avoid the problems arising in formidable strong acidic and alkaline environments, which also mitigates the environmental-related pollution. Wu *et al.* developed a 2D/2D MoP/$MoS_2$ heterostructure that fulfils all the requirements needed for the HER process in a neutral environment, *i.e.*, it possesses good conductivity for electron transfer, which is beneficial to decrease the Ohm resistance, plentiful active sites on the heterointerface present between 2D-MoP and 2D-$MoS_2$ for $H_2O$ activation, and a porous environment on the surface for easy mass transfer, thus weakening the diffusion resistance.[106] The neutral medium was balanced using 0.5 M $H_2SO_4$ with 1 M phosphate buffered solution and 1 M KOH. The MoP/$MoS_2$ heterostructure exhibited an impressive current density at a low overpotential in neutral medium, which was much higher than that obtained for the bare $MoS_2$ and for the reaction occurring in acidic and basic conditions. Furthermore, the MoP/$MoS_2$ heterostructure also exhibited a good reaction kinetic mechanism with a low Tafel slope value (48 mV $dec^{-1}$), which follows the Volmer–Heyrovsky reaction pathway. Considering that the neutral medium is governed through the adsorption of $H_2O$ molecules on the surface of the catalyst, the relative free energy of the hydrogen atom and $H_2O$ molecule was evaluated through DFT calculations, as shown in Fig. 9j. The calculated $\Delta G_{H^*}$ for hydrogen adsorption indicates that the MoP/$MoS_2$ 2D/2D heterostructure (−0.12 eV) is more favourable for the HER than bare $MoS_2$ (1.79 eV). Furthermore, the higher $H_2O$ adsorption energy obtained for MoP/$MoS_2$ (−1.38 eV) than its neat counterpart suggests that $H_2O$ can be easily adsorbed on the catalyst surface and is beneficial due to 2D/2D heterostructure. Furthermore, according to the density of state near the Fermi level, as shown in Fig. 9k, the fast electron transport in the HER process for $MoS_2$/MoP was evaluated. Conversely, Liang *et al.* demonstrated that $MoS_2$/black phosphorous exhibited superior activity in both acidic and basic medium.[136]

**4.1.2 Photocatalytic $H_2$ evolution.** Overall water splitting under light illumination is a redox reaction and is mainly divided into two key reactions, which are water oxidation and water reduction [eqn (13)–(16)] and have been extensively considered since the pioneering work by Fujishima and Honda.

$$\text{Photocatalyst} \xrightarrow{h\vartheta} e^- + h^+ \tag{13}$$

$$\text{Reduction}:\ 2H^+ + 2e^- \rightarrow H_2 \tag{14}$$

$$\text{Oxidation}:\ H_2O + 2h^+ \rightarrow 2H^+ + \frac{1}{2}O_2 \tag{15}$$

$$\text{Overall}:\ H_2O \rightarrow H_2 + \frac{1}{2}O_2 \tag{16}$$

Generally, for the production of hydrogen and oxygen, the photocatalytic system mainly requires efficient photocatalysts and a light supply, which can be either a visible or UV-visible source. Under the action of photons, photogenerated charge carriers are generated and transferred to their respective band edge, *i.e.*, electron jumps from the VB to CB edge, leaving a hole in the VB position. The electron in the CB of the photocatalyst is responsible for the reduction of water to produce hydrogen gas, while the hole in the VB facilitates the water oxidation reaction. This mechanism will happen when the CB position is located at a potential that is more negative than the potential required for the reduction of water, *i.e.*, $H^+/H_2$ = 0 V *vs.* NHE at pH = 0 and −0.41 V *vs.* NHE at pH = 7, whereas the top level of the VB must be more positive than the redox potential of $H_2O/O_2$, *i.e.*, 1.23 V at pH = 0 and 0.82 at pH = 7. In addition, the band gap must be higher than 1.5 V and not exceed 3.2 V.[3,5,6] However, the utilization of noble metals or alloys is hindered by their high cost. Therefore, currently, it is urgent for researchers to develop competitive alternatives to noble metals. Despite the numerous photocatalytic materials, the unique candidate 2D-$MoS_2$ plays an important role not only as a co-catalyst but also an excellent visible-light semiconductor with high hydrogen evolution activity due to its high surface to volume ratio, low cost, high catalytic activity, good stability and abundant active sites.[45,46,137]

The studies in the literature revealed that generally pure $MoS_2$ as a photocatalyst exhibits no or negligible hydrogen evolution activity under visible light illumination. However, the photocatalytic hydrogen evolution activity of 2D-$MoS_2$ is regulated by the number of layers of $MoS_2$. With a decrease in the number of layers, the photocatalytic $H_2$ evolution activity increases, which is maximum for a single layer of $MoS_2$. This layer-dependent activity mainly originates from the exposed edges of $MoS_2$ containing a large number of unsaturated dangling sulphur atoms (active sites for hydrogen generation), which bind the $H^+$ ion very strongly.[32] In addition, the band gap structure of 2D-$MoS_2$ also plays a role in its photocatalytic $H_2$ evolution performance. The wide band gap resulting from the quantum confinement effect of $MoS_2$ (1.8–1.9 eV) and its low conduction band (CB) potential (0 to −0.12 eV) satisfy the conditions for the water reduction reaction (0 eV, at pH = 0 *vs.* RHE). To date, numerous works have been reported regarding the water reduction reaction using neat ultrathin $MoS_2$. For example, Peng *et al.* fabricated a single-layer multiphasic $MoS_2$ nanosheet keeping the optimum ratio between the 2H semiconducting phase and quasi metallic 1T' phase and employed it directly as an efficient hydrogen evolution photocatalyst.[130] According to the DFT study, they revealed that the in phase heterojunction between the 2H and 1T' phase is responsible efficient charge transfer and separation, which are essential for photoactivity. Moreover, the suitable band gap of the 2H semiconducting phase is responsible for light absorption and charge generation, and the basal and edge sites at the 1T' phase are the most favourable for hydrogen evolution. Further, considering the limited $H_2$ production by pure $MoS_2$, Wan and co-workers employed a novel approach for the synthesis of few-layer $MoS_2$ nanosheets from an $MoS_2$ stack with high yield through the facile solvothermal method followed by liquid exfoliation treatment.[138] This synthetic procedure is beneficial for electronic and structural modification, which provides a large surface area together with additional exposed active edge sites, promoting the separation and transformation of photogenerated charge pairs to a greater extent. The solid monodispersed few-layer $MoS_2$ nanosheets exhibited an excellent photocatalytic hydrogen evolution performance of 1241.3 μmol $g^{-1}$ $h^{-1}$. As described in Fig. 10a and b, the high photocatalytic effect is mainly attributed to the (i) formation of isolated nanosheets with a high surface area and exposed active sites for $H^+$ adsorption and hydrogen evolution reaction, (ii) creation of lattice cracks on the inert basal plane due to the ultrasonication effect, followed by heat treatment, which added extra active sites, (iii) decrease in the number of layers of $MoS_2$ nanosheets, which is beneficial for efficient charge separation and migration together with the creation of a direct band gap, (iv) structure change in which the $MoS_2$ nanosheets possess a more negative CB potential for superior HER activity. Furthermore, the solid nature together with excellent stability and dispersibility in solution make the $MoS_2$ nanosheets a great potential candidate for application in many fields. In addition, the as-obtained $MoS_2$ nanosheets exhibited enhanced photoelectrochemical properties such as high transient photocurrent density, suggesting its superior photoelectric response, and the impedance measurement showed they possess good conductivity for promoting the transfer of photoinduced charge pairs in the photocatalytic reaction. Another few-layer $MoS_2$ material towards photocatalytic hydrogen evolution was reported by Wang *et al.*[139] They prepared few-layer (1–4 layer) $MoS_2$ through a facile liquid-phase exfoliation strategy using a salt and organic electrolyte solution. It was found that the sodium tartrate-treated $MoS_2$ exhibited a superior photocatalytic hydrogen evolution rate, *i.e.*, 0.5 mmol $g^{-1}$ $h^{-1}$ compared to that of bulk $MoS_2$.

Besides few-layer neat $MoS_2$, the compositing of ultrathin neat $MoS_2$ as a photocatalyst and co-catalyst with various UV- and visible-driven materials such as metal oxides, metal sulphides and carbonaceous materials has been studied recently. Here, we summarize a few recent reports on 2D/2D $MoS_2$-based heterostructures towards photocatalytic hydrogen evolution. For example, Yuan *et al.* developed a 2D/2D black phosphorous/$MoS_2$ heterostructure photocatalyst towards hydrogen evolution under visible light irradiation.[103] The 2D/2D BP/

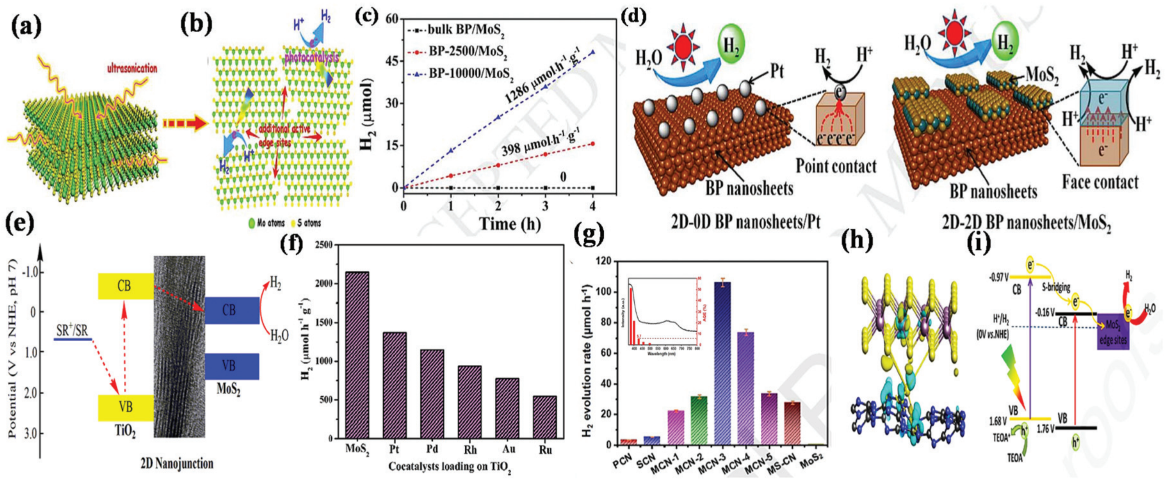

Fig. 10 (a) Schematic illustration of the liquid exfoliation strategy for $MoS_2$ by ultrasonication treatment and (b) disordered structure of few-layer $MoS_2$ nanosheets. Reproduced with permission.[138] (c) Production of $H_2$ through the photoreduction of various BP/$MoS_2$ samples and (d) schematic illustration of the charge transfer process in 2D–0D BP-10000/Pt and 2D–2D BP-10000/$MoS_2$ photocatalyst. Reproduced with permission.[103] (e) Energy diagram illustration of the photocatalytic mechanism over the 2D–2D $MoS_2/TiO_2$ photocatalyst and (f) $H_2$ production yield on 0.50 wt% of different co-catalyst-loaded $TiO_2$. Reproduced with permission.[140] (g) Comparison of $H_2$ production rates of MS-CN, SCN and MCN samples, [inset figure: representation of AQE for $H_2$ evolution], (h) side-view illustration of MCN heterostructure with differential charge density (net electron accumulation and depletion are depicted by the yellow and navy regions, respectively) and (i) proposed mechanistic pathway diagram for photocatalytic $H_2$ production reaction under visible light illumination. Reproduced with permission.[110]

$MoS_2$ heterostructure exhibited a high current density (3.14 mA $cm^{-2}$) together with high $H_2$ evolution efficiency (1286 μmol $h^{-1}$ $g^{-1}$), as shown in Fig. 10c, and an apparent quantum yield of 1.2% in comparison with $MoS_2$ nanosheets and bare BP sheets. In this study, the high photocatalytic activity is due to the unique 2D/2D interface (face contact) and was compared to a typical 0D/2D structure (point contact) by taking Pt as a 0D cocatalyst. According to the point of charge migration and charge pair separation, as given in Fig. 10d, it is obvious that the smart 2D/2D photocatalyst exhibits a much great contact nanointerface than 0D/2D, which provides a longer diffusion path length for the charge transfer and separation of photogenerated charge pairs, thus resulting in higher photocatalytic $H_2$ evolution. Moreover, the driving force is another crucial factor in modulating the photocatalytic $H_2$ production performance, and here the combination of quantum-sized BP (10 000 rpm) with $MoS_2$ provides a greater driving force, which lowers the CB to a more negative potential to achieve a high photocatalytic hydrogen evolution rate. In addition, Yuan *et al.* also applied a similar type of phenomenon to a 2D/2D binary ($MoS_2$/CdS, $MoS_2$/g-$C_3N_4$) system and 2D/2D/2D ternary system (g-$C_3N_4$/graphene/$MoS_2$) through face-to-face contact and observed excellent photocatalytic activity compared to other photocatalysts.[141–143] Compared to the 2D/2D $MoS_2$-based heterostructure, we employ a 2D $MoS_2$-based 2D/OD heterostructure to gain more insight into the structure–activity relationship. In this case, Chai *et al.* monitored the photocatalytic hydrogen evolution experiment using an $MoS_2$/CdS composite in which $MoS_2$ nanosheets were uniformly distributed on CdS nanospheres.[144] The as-fabricated composite with only 5% $MoS_2$ exhibited a hydrogen evolution rate of about 372 μmol $h^{-1}$ with an apparent quantum yield of 7.31% under 300 W Xenon lamp illumination. The photocatalytic activity is attributed to the easy migration and separation of photogenerated charge carriers in the composite photocatalysts. Moreover, it should be noted that in comparison to binary 2D heterostructures, ternary 2D heterostructures provide a larger and more intimate 2D junction, which can effectively enhance the charge transfer rate, resulting in high photocatalytic activity.

Yuan *et al.* employed facile hydrothermal method for developing an $MoS_2/TiO_2$ (001) 2D/2D nanosheet heterojunction.[140] The constructed typical 2D/2D heterojunction possessed a large and intimate interface between $MoS_2$ and $TiO_2$ and also boosted the separation and transportation efficiency of photogenerated charge pairs, which is attributed to the synergistic effect of $MoS_2$ and $TiO_2$. The energy diagram for the charge transfer process between $MoS_2$ and $TiO_2$ is illustrated in Fig. 10e. The 2D/2D interfacial structure provides a large contact area with abundant exposed active sites, which accelerate the rate of hydrogen evolution, achieving 2145 μmol $h^{-1}$ $g^{-1}$, a value 36.4-fold that of $TiO_2$ nanosheets with an apparent quantum yield of 6.4% (360 nm). According to the data shown in Fig. 10f, it is also obvious that the $MoS_2/TiO_2$ (001) 2D/2D heterojunction is more active towards $H_2$ production than noble metals such as Pt, Pd, Au, Rh and Ru-loaded $TiO_2$ (001) nanosheets. Hence, it was proven that $MoS_2$ acts as a better cocatalyst in 2D–2D systems than noble metals for hydrogen evolution activity.

Recently Dong *et al.* developed an S-doped g-$C_3N_4$/$MoS_2$ 2D/2D face-to-face heterojunction photocatalyst and observed its superior photocatalytic activity.[110] The hydrogen evolution performance was investigated under visible light irradiation together with TEOA as a sacrificial agent. As shown in Fig. 10, the 2D/2D g-$C_3N_4$/$MoS_2$ heterojunction achieved a high $H_2$ production rate, *i.e.*, 2120 μmol $h^{-1}$ $g^{-1}$ (Fig. 10g) together with a notable quantum yield of 5.7% (inset image) The high photocatalytic performance is attributed to the fast transportation of photogenerated charge carriers and efficient charge separation through the interface contact produced due to the face-to-face heterojunction between the two 2D components, which was also supported by the high photocurrent response. Moreover, first principle calculations of the differential charge density have become a crucial parameter to get an in-depth understanding about the charge separation efficiency based on photocatalytic activity. In this regard, Fig. 10h shows the charge redistribution at the face-to-face interface between 2D-S-g-$C_3N_4$ and 2D-$MoS_2$, which clearly represents the accumulation and depletion of electrons in the $MoS_2$ region, while the holes remain in the SCN region. The high efficiency is mainly due to the presence of S atoms, as seen in polarized field in the figure, facilitating the charge distribution at the interface region, which not only improves the light absorption capacity, but also allows efficient charge transfer. The possible $H_2$ evolution mechanism proposed in Fig. 10i together with the energy band structure shows that the rapid channelization of photoexcited electron occurs from SCN to $MoS_2$ through the face-to-face interface and the final $H_2$ gas is evolved over the unsaturated S atoms at the $MoS_2$ exposed edges. Thus, the above studies deduced that 2D/2D engineering between two 2D materials through face-to-face contact is one of the feasible ways to achieve charge separation for superior photocatalytic hydrogen production. The face-to-face 2D/2D interface structure for photocatalytic application has been widely employed by many researchers, and prior to this, more insight was gained by comparison with point contact.

### 4.2 Nitrogen reduction reaction

Similar to hydrogen, ammonia is an expectant "green fuel" candidate towards environmental sustainability, which is required to minimize the current issue based on the scarcity of fossil fuels.[145,146] Due to its low liquefying pressure and high hydrogen density, ammonia also plays a vital role as an easy transportable promising carbon-neutral energy carrier with zero-balance greenhouse gases such as $CO_2$ emission.[147,148] However, the conversion of $NH_3$ from $N_2$ through the $N_2$ fixation reaction *via* natural (nitrogenase enzymatic process) and artificial (*i.e.*, industrialized Haber–Bosch process) processes is a practical problem nowadays due to the involvement of series of biochemical steps, which delay the reaction rate, increase the cost-effective, and reduce the safety.[7,149] Thus, now it is of great significance to develop cost-effective, green and sustainable techniques for the production of $NH_3$. Although a mimicking methodology has been investigated, *i.e.*, traditional heterogeneous catalysis, electrocatalysis and photocatalysis-based NRR involving stable and noble-metal free catalysts at room temperature and atmospheric pressure is becoming a highly desirable and profitable artificial technique towards the reduction of $N_2$ to $NH_3$.[7,75,146,148,150–153] For instance, the electrochemical NRR process involves the use of electrolytic cells together with different electrodes and electrolytes, which are powered by solar cells, wind turbines, *etc.*, whereas in terms of photocatalytic NRR, the reaction is directly governed by sunlight or visible light. Although Mo-based catalysts exhibit a great performance towards the NRR as both photocatalytically and electrocatalytically active, to date, only a few studies have been reported, which are summarized in the following section. In the case of the photocatalytic and electrocatalytic NRR processes, both follow a number of mechanistic pathways, which can be determined through DFT analysis, to give the product.

To design a potential catalyst with a low limiting potential ($U_L$) towards superior photo/electrocatalytic $N_2$ reduction, theoretical calculations based on machine learning are considered. According to DFT calculations, it has been predicted that the NRR performance is directly correlated with the five adsorbates (H, $N_2$, $N_2H$, NH, and $NH_2$), whose binding energies are over 8 eV.[154] The limiting potential that determines the minimum applied voltage to the exergonic NRR process follows one of two protonation steps, *i.e.*, $^*N_2 \rightarrow {}^*N_2H$ and $^*NH \rightarrow {}^*NH_2$. Based on the DFT-computed free energy study, the $U_L$ can be represented as follows:

$$U_L = \frac{\Delta G_{N_2H} - \Delta G_{N_2}}{e} \text{ or } U_L = \frac{\Delta G_{NH_2} - \Delta G_{NH}}{e}$$

It has been determined from machine learning work that the catalytic surface, which fulfils the 4 to 6 d orbital occupation, can potentially lower the $U_L$ for the NRR reaction.[154]

**4.2.1 Electrocatalytic NRR.** In electrochemical NRR, the first step is the generation of an $H^+$ ion at the electrode/electrolyte interface, which then migrates through the electrolytic solution towards the catalytic surface, and finally, on the surface of catalytic site present on the cathode, the adsorbed $N_2$ reacts with $H^+$ and is converted to $NH_3$ with the capture of an electron. Thus, the crucial step in the electrocatalytic NRR is the binding capacity of N to the catalytic surface, which indicates that the working electrode (catalyst) should have an optimized nitrogen binding capacity. The NRR follows three mechanistic pathways to give product. The mechanistic pathway is governed by the proton-coupled electron ($H^+$/$e^-$) transfer process, which converts $N_2$ to $NH_3$ under ambient reaction conditions. In detail, in the first step, the $N_2$ molecule is adsorbed on the surface of the catalyst ($^*N{\equiv}N$) and then captures one proton ($H^+$) and one electron from the catalyst surface to give an adsorbed intermediate chemical species, *i.e.*, $^*N{=}NH$, which is converted to the final $NH_3$ product following the transfer of $H^+$/$e^-$ pairs through the associative mechanism followed by the formation of different intermediate by-products such as $N_2H_4$ and $N_2H_2$.[146,155,156] From a theoretical point of view, it has been elucidated that some metals such as Fe, Mo, Ru, Rh, Pt and Ir exhibit relatively optimized nitrogen binding capacity.[155] Kim *et al.* investigated the distal mechanistic pathway through machine learning over several transition metals and found that the Mo surface with (110) plane exhibits the lowest $U_L$ value among them, *i.e.* about −0.92 V. Together with the low limiting potential over the Mo (110) surface, the binding energy difference, which estimates the adsorption competition of $N_2$ and H components, is also more negative, *i.e.*, −0.18 eV, which suggests a higher faradaic efficiency.[154]

Based on the demands regarding optimized $N_2$ binding catalysts, Mo-based materials have been widely investigated as NRR electrocatalysts. Among them, 2D-$MoS_2$ acts as an ideal catalyst for the NRR. Similar to the HER on $MoS_2$, the edge sites of $MoS_2$ are also more preferable towards the electrocatalytic NRR under ambient conditions. It has been considered that the elements Mo and S, which are the key elements of the nitrogenase-mediated reaction, play a vital role in the nitrogen fixation reaction. Accordingly, proof-of-concept regarding electrocatalytic NRR over $MoS_2$ was investigated on accordance with DFT calculations, which mapped out the electronic environment of $MoS_2$ through various energy profile diagramd.[117,157] In this regard, in 2018, Zhang and co-workers reported their study based on the electrocatalytic NRR activity of 2D-$MoS_2$ from a theoretical and experimental point of view to show whether the edge-site $MoS_2$ are electrocatalytically active.[117] According to the DFT studies, the isosurface of the deformation charge density of $MoS_2$ was calculated to be a positively charged environment, *i.e.* $+0.963|e|$, around the edges of the Mo ion, which plays a significant role in the activation and polarization of $N_2$ molecules. Also, the $N_2$ molecules are generally activated and polarized at the positively charged centre, and thus based on DFT, they further deduced a free energy profile, as shown in Fig. 11a, from which the potential determining step (PDS) was studied. The PDS explains the reductive protonation of adsorbed $N_2$ on the Mo edge surface with a lower limiting barrier of about 0.68 eV without applying any external potential, which is much higher in the case of some common metal surfaces, ranging from 1 to 1.5 eV. The relatively low barrier predicted by PDS for the Mo edge suggests the significant elongation of the N–N bond length, *i.e.*, from $^*N_2$ (1.129 Å) to *NNH (1.221 Å), as shown in Fig. 11b, which accelerates the NRR. Consequently, the N≡N triple bond is easily weakened by the transformation of the charge from $N_2$ to positively charged Mo-edge, resulting in N–Mo bond formation. This is clearly illustrated by the deformation charge density of *NNH supplied in Fig. 11c. Fig. 11d shows the $NH_3$ yield together with the corresponding faradaic efficiencies (FEs) under the application of different potentials. An appreciable $NH_3$ yield of $8.08 \times 10^{-11}$ mol $s^{-1}$ $cm^{-2}$ with a faradaic efficiency of 1.17% was achieved. The highest $NH_3$ yield and faradaic efficiency were achieved at an optimum potential of −0.5 V, after which, the value markedly decreased, suggesting the competence adsorption nature of both hydrogen and nitrogen on the electrode surface. In addition, the $MoS_2$/CC electrode possessed high stability given that there was no obvious change in $NH_3$ yield after ten successive recycling tests. This relatively low barrier in terms of PDS on the Mo-edge further strengthens the claim that $MoS_2$ is a potential catalyst for the NRR. Based on the abovementioned studies, although the $MoS_2$ edge site is predicted to give an appreciable $NH_3$ yield, some improvement is still needed regarding NRR selectivity due to its HER competence. Hence, Liu *et al.* prepared an ultrathin S-rich $MoS_2$ nanosheet through Li intercalation and tested its performance towards the NRR in an acidic environment.[158] The Li ion interacts with the S edge site of $MoS_2$, which facilitates the adsorption of $N_2$, and hence enhances the nitrogen reduction. According to the DFT study, it was found that Li–S interaction increases the $N_2$ adsorption free energy from −0.32 to −0.70 eV and decreases the activation energy barrier of the reaction control

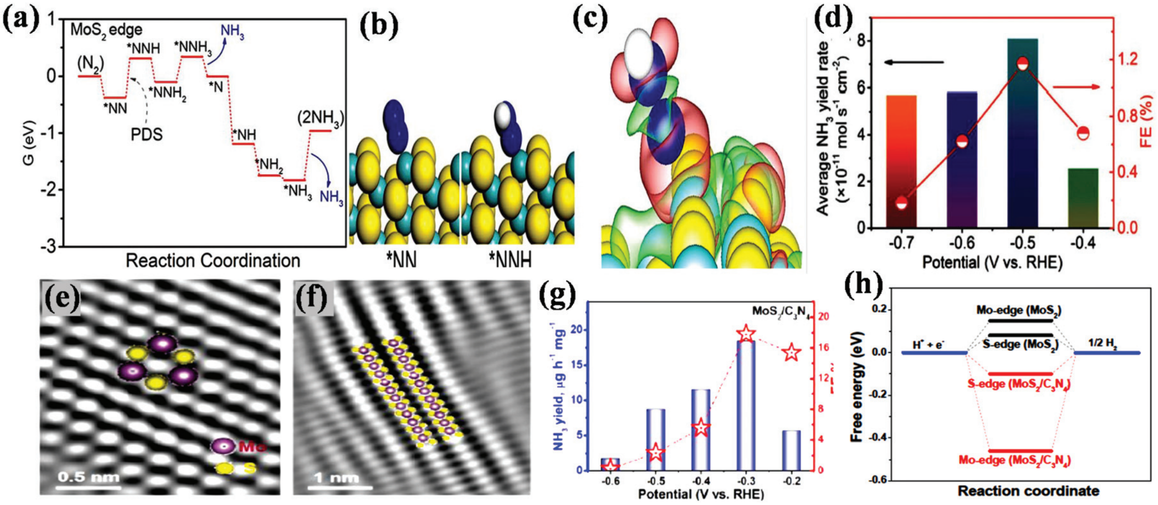

Fig. 11 (a) Free-energy profile diagram at $MoS_2$ edge site for the NRR, (b) structural representation of the key intermediates of the PDS, (c) deformation charge density diagram of *NNH, and (d) average $NH_3$ yield and faradaic efficiency graph for $MoS_2$/CC at different potentials. Reproduced with permission.[117] (e) and (f) IFFT images of $MoS_2/C_3N_4$, (g) $NH_3$ concentration and faradaic efficiency plot for $MoS_2/C_3N_4$ and (h) free energy diagrams of *H ($\Delta G^*H$) of $MoS_2$ and $MoS_2/C_3N_4$ on Mo-edge and S-edge sites. Reproduced with permission.[159]

step from 0.84 to 0.42 eV, and simultaneously, it also reduces the hydrogen adsorption free energy. The designed catalyst exhibited an $NH_3$ yield rate of 43.4 μg $h^{-1}$ $mg^{-1}$ with the highest faradaic efficiency of 9.81%, while suppressing the HER yield.

Nevertheless, the electrocatalytic NRR activity of neat $MoS_2$ nanosheets is still not satisfactory, and hence interfacial engineering *via* 2D/2D $MoS_2$-based heterostructures is a powerful technique to meet the requirements for the NRR. Chu *et al.* designed a 2D/2D $MoS_2$/g-$C_3N_4$ heterostructure for the NRR through a simple *in situ* hydrothermal method.[159] According to the DFT analysis, the effective NRR performance is due to the face-to-face coupling interaction of $MoS_2$/g-$C_3N_4$, which facilitates the stimulation of Mo edge sites towards the NRR and protects the NRR-active Mo-edge sites against the competing HER. However, the noise-filtered inverse fast-Fourier transform (IFFT) study, as shown in Fig. 11e and f, for $MoS_2/C_3N_4$ revealed that over the hexagonal symmetry basal plane of 2D-$MoS_2$, orderly stacked $MoS_2$ layers are present together with exposed abundant Mo edge-terminating sites, which are believed to be the NRR active sites. Thus, to prove this hypothesis, the NRR performance over $MoS_2/C_3N_4$ was evaluated in 0.1 M $LiClO_4$ solution under ambient conditions. The best $NH_3$ yield and the faradaic efficiency of the given electrocatalyst, as depicted in Fig. 11g, were obtained to be 18.5 μg $h^{-1}$ $mg^{-1}$ and 17.8%, respectively, at only −0.3 V of applied potential. However, beyond the potential of −0.3, the rate of $NH_3$ together with the faradaic efficiency significantly decreased (*e.g.*, at −0.2 V), which is ascribed to the competing HER on the surface of the electrode. During the course of the reaction, Chu *et al.* also depicted that the $MoS_2/C_3N_4$ heterostructure electrocatalyst resulted in an excellent ammonia yield with good selectivity towards the NRR compared to neat $C_3N_4$ and $MoS_2$ given that no $N_2H_4$ was detected. The reduction mechanism was thoroughly investigated through a DFT study (distal pathway). The free energy calculation followed by the potential limiting steps of all the intermediates suggested that $MoS_2/C_3N_4$ exhibits a relatively low energy barrier for the reaction-controlling step, *i.e.*, up to 0.55 eV for $*N_2$ to $*N_2H$, which changes to 0.62 eV for the pathway of $*NNH_2$ to *N. The PDS value for $MoS_2/C_3N_4$ is much more lower than that of neat $MoS_2$, which suggests that the face-to-face interfacial contact created between 2D-$MoS_2$ and 2D-$C_3N_4$ effectively stimulates the NRR activity by stabilizing $*N_2H$. Furthermore, the protection of the NRR-active Mo-edge sites from the competing HER was also proven through the free energy study, as shown in Fig. 11h. Based on the calculated free energy data, $\Delta G^*H$ was 0.08 and 0.15 eV for Mo and S-edge in pristine $MoS_2$, respectively, whereas it was −0.46 eV for Mo edge and −0.12 eV for S-edge in the $MoS_2/C_3N_4$ heterostructure. However, the great change in $\Delta G^*H$ at the Mo-edge suggests the protection of the Mo-edge rather than the S-edge sites (favourable $\Delta G^*H$), which is unfavourable for the HER, hindering the formation $H_2$ while allowing the NRR.

In addition, Li *et al.* developed a highly active and durable $MoS_2$/RGO hybrid towards electrocatalytic NRR and found that it exhibited excellent selectivity for $N_2$ conversion to $NH_3$ under ambient conditions.[160] The $MoS_2$/RGO 2D/2D electrocatalyst achieved a high $NH_3$ yield, *i.e.*, 24.82 μg $h^{-1}$ $mg^{-1}$, with the corresponding faradaic efficiency of 4.56% at a potential of −0.45 eV. According to the DFT study, the authors suggested that the $N_2$ adsorption on $MoS_2$/RGO is more favourable than that on separate $MoS_2$, which originated from the enhanced electron transfer. Further the PDS of the electron–proton coupling transferring process of $*NHNH_2$ to $*NH_2NH_2$ with an energy barrier of 0.49 eV suggests the feasible generation of ammonia.

**4.2.2 Photocatalytic NRR.** The photocatalytic nitrogen fixation strategy is regarded as energy efficient and environmentally benign because the reaction proceeds under ambient conditions, benefiting from clean and renewable resources such as solar energy, and the product is achieved directly from nitrogen and water.[149,155] The photocatalytic NRR process involves three steps as follows: (i) generation of photoexcited charge carriers under light energy irradiation, (ii) separation and migration of charge carriers to the catalytic surface, and (iii) participation of photoexcited electrons and holes in the redox process of NRR modulated by $H^+$ and electrons. Thus, for an efficient NRR, the CB of the catalyst should lie at a more negative potential than the theoretical reduction potential required for $N_2$ hydrogenation and the VB should be at a more positive than the water reduction potential value.[7] The photofixation mechanism is not only governed by the suitable heterogeneous catalytic centre, but also a multi-electron reduction process to minimize the thermodynamic barrier, which can also prevent the formation of high energetic intermediates, as already discussed in the electrochemical NRR section. To date, a number of photocatalytic semiconductors such as $CeO_2$, $TiO_2$, $WO_3$, and $Bi_2MoO_6$ besides $MoS_2$ have been reported to reduced $N_2$ to $NH_3$ under UV and visible light illumination, but the obtained concentration of $NH_3$ is not satisfactory to meet the practical demand.[152,161–163] $MoS_2$ plays a vital role in this field and also acts as an electron-rich semiconductor that facilitates the multi-electron reduction reaction essential for the NRR. Reviewing the literature regarding photocatalytic $N_2$ fixation, it was deduced that a few works have been carried out on the design of $MoS_2$. According to these works, some examples such as Sun *et al.* in 2017 developed sonicated ultrathin $MoS_2$ for photocatalytic $N_2$ reduction to $NH_3$ under simulated solar light and achieved a concentration of 0.14 mg $L^{-1}$ $NH_3$ in DI water in 10 h.[50] The production of a high concentration of $NH_3$ mainly depends on its ultrathin structure, providing a platform to produce more charged excitons, which behave as an electron-rich species (Fig. 12a). Considering that the NRR is regulated by a multi-electron–proton-based pathway, the participation of protons was studied by considering the photocatalytic NRR in an acidic solution with different pH, as shown in Fig. 12b. The result suggests that the ammonia concentration is high (0.83 mg $L^{-1}$) when the pH of the solution is 3.5, which may be attributed to the production of an excess proton from the acid water environment, and this reduces the kinetic barrier for the $N_2$ reduction reaction. In addition, to

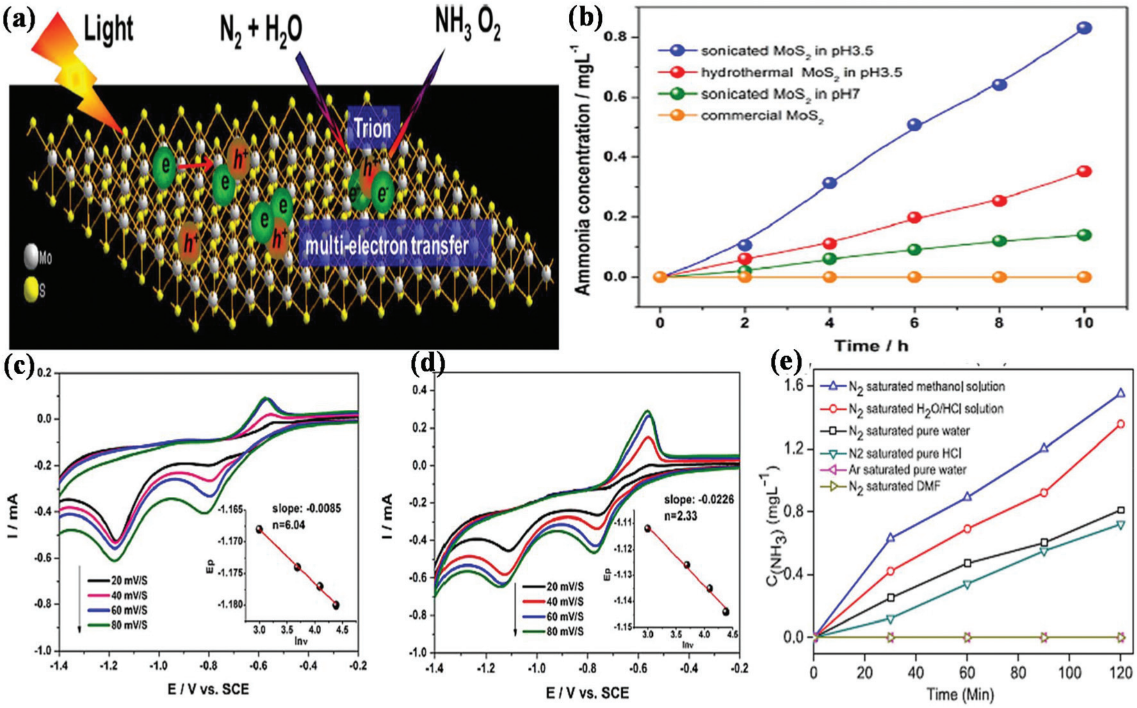

**Fig. 12** (a) Schematic representation of multi-electron $N_2$ photoreduction process and (b) rate of ammonia concentration over various $MoS_2$ samples mediated by different conditions. Cyclic voltammograms in $N_2$-saturated 0.5 M $Na_2SO_4$ (pH = 3.5) at different scan rates for (c) sonicated ultrathin $MoS_2$ electrode and (d) commercial $MoS_2$ electrode. Reproduced with permission.[50] (e) Yield of photoreduction of $N_2$ fixation on 5% $MoS_2$/$MgIn_2S_4$ heterojunction photocatalyst under various solvent conditions. Reproduced with permission.[90]

verify the multi-electron reduction process, the electron transfer number for the $N_2$ reduction reaction was calculated according to the Laviron equation. The slope of the curve, as depicted in Fig. 12c and d, suggested a 2.33- and 6.04-electron transfer process for bulk/commercial $MoS_2$ and ultrathin $MoS_2$, respectively, which make $MoS_2$ energetically qualified for the $N_2$ photoreduction reaction. The electron transfer number of 6.04 is sufficient to decrease the thermodynamic barrier under ambient conditions.

However, the $N_2$ reduction efficiency obtained for pristine $MoS_2$ is quite low compared to other photocatalysts, but from an experimental view, it has been seen that after compositing it with other 2D photocatalysts, its $N_2$ reduction efficiency significantly increases. In this regard, our group designed a 2D/2D $MoS_2$/$MgIn_2S_4$ heterojunction photocatalyst and tested its activity under visible light irradiation (250 W Hg lamps).[90] The controlled photocatalytic $N_2$ fixation experiment as illustrated in Fig. 12e, where the as-fabricated sample was tested under different reaction conditions using various scavenging units at the optimum pH. The investigated 2D/2D heterojunction photocatalyst achieved the highest concentration of $NH_4^+$ (1.54 mg $L^{-1}$) with 10 vol% methanol–water system compared to that for distilled water (0.81 mg $L^{-1}$) and DMF (no ammonia) due to the quick oxidation of methanol by $h^+$, which produces $CO_2^{*-}$ to facilitate the reaction easily. In contrast, by regulating the pH of the reaction, it was deduced that under a very high acidic environment (0.1 M HCl), the concentration of $NH_3$ is quite low (0.72 mg $L^{-1}$), whereas it increases with an increase in pH. It was observed for the HCl/$H_2O$ system with the optimum pH (pH = 3.6) that the ammonia concentration reached a high value (1.35 mg $L^{-1}$). However, it was believed that in a highly acidic medium, the HER is dominant over the corresponding NRR, and in a moderate acidic medium, the generation of excess protons reduces the kinetic barrier for the NRR. Moreover, the given 2D/2D heterojunction photocatalyst possessed high selectivity towards the $N_2$ reduction reaction with a 4.8-electron transfer process given that the peak for the bi-product ($N_2H_4$) was absent. The 2D/2D $MoS_2$/$MgIn_2S_4$ photocatalyst achieved an excellent NRR performance and long-term stability was also observed for its photocurrent density. However, the overall photocatalytic performance depends on the 2D/2D combination through petals of the flower (2D-$MgIn_2S_4$) and a sheet ($MoS_2$), which are attached *via* a face-to-face and face-to-edge fashion and the p–n heterojunction mechanism, favouring efficient charge migration and separation at the interface.

### 4.3 Carbon dioxide reduction reaction

As already discussed in the previous section, the excessive consumption of fossil fuels greatly increases the atmospheric carbon dioxide ($CO_2$) level, and hence is regarded as the main culprit responsible for global climate change. The increase in $CO_2$ level also disturbs the carbon cycle, leading to a severe greenhouse effect on the Earth's surface.[1,2,4,164,165] Thus, nowadays, the foremost challenge faced by society is to conserve the environment for the future generation in the aspect of depletion of renewable energy sources with a reduction in the $CO_2$ level in the atmosphere. In this scenario, the key issue is to design novel technologies that can relieve environmental problems by mitigating the $CO_2$ concentration in the environment together with the production of sustainable energy using a clean and abundant strategies. Thus, to realize this fascinating blueprint, converting $CO_2$ through the reduction process into renewable fuels together with value-added clean carbon-based nontoxic chemicals such as carbon monoxide (CO), hydrocarbons, alcohols, syngas, and formic acid has emerged as the most compelling pathway to build a sustainable recycling system by fulfilling the global energy demands.[164–167] Nevertheless, $CO_2$ is a stable, linear and chemically inert molecule bearing a huge energy gap of around 13.7 eV between its LUMO and HOMO, and hence the transformation of $CO_2$ is a thermodynamically uphill reaction, demanding a significant energy input for the dissociation of the C=O bond, which is around 750 kJ $mol^{-1}$.

The process of $CO_2$ reduction involves the adsorption and activation of a $CO_2$ molecule on the surface of catalyst followed by a number of different reaction steps regulated through a 2, 4, 6, 8, 12 or more electron transfer pathway, which is kinetically very unfavourable.[4] However, the photo/electro reduction of $CO_2$ using efficient catalysts is becoming an economical and practical approach to solve the associated thermodynamic and kinetic hurdles. It has been concluded that both photocatalytic and electrocatalytic $CO_2RR$ are surface phenomena regulated through both protons and electrons.[165,166]

Besides water splitting, 2D-$MoS_2$ has also emerged as an excellent candidate for the reduction of $CO_2$ both photocatalytically and electrocatalytically. The superior catalytic efficiency of $MoS_2$ in the $CO_2$ RR has mainly emerged from its Mo and S-terminated edges and low work function value, which promote the efficiency of $MoS_2$. By observing the periodic strip model, it was reported that in $MoS_2$ there are two distinct types of edges, *i.e.*, $\bar{1}010$ and $10\bar{1}0$ edges, which are attributed to the S and Mo edges, respectively, and highly active towards the $CO_2$ reduction reaction.[168] In addition, it has been seen that in 2D-$MoS_2$, the presence of active Mo-terminated edge sites stabilizes the intermediate products such as $CH_xO_y$ produced during the $CO_2$ reduction reaction.[168–170]

The $CO_2$ reduction activity can be analysed *via* the binding energies of the $CO_2$ reduction intermediates through computational analysis. For the $CO_2$ reduction reaction, the computational hydrogen electrode model has received much attention to determine the mechanism of catalytic reactions and free energy profiles of the reaction intermediates proceeding through proton–electron ($H^+/e^-$) pair transfer by considering the effect of the electrode potential value on the reaction free energy.[171,172] In addition, for each elementary step, the theoretical limiting potential ($U_L$) is necessary, which determines the lowest external potential at which the reaction steps become exergonic together with the theoretical onset potential for the $CO_2$ reduction reaction and is calculated as follows:

$$U_L = -\frac{\Delta G_{U=0}}{e}$$

where $\Delta G_{U=0}$ represents the change in free energy of the reaction at 0 V *vs.* RHE.

Accordingly, the most negative limiting potential is taken as the onset potential of the reaction. Chan *et al.* reported that product formation by the $CO_2$ reduction reaction to CO follows the lowest free energy reaction path for $MoS_2$ compared to other transition metals such as Au. From their study, at a specific surface coverage, $MoS_2$ with Mo edges and S edges exhibited a $U_L$ value of −0.61 V and −0.15 V, respectively, which are smaller than that for Au (−0.78 V) at 0 V *vs.* RHE.[168]

However, the sluggish reduction potential needed for the conversion of $CO_2$ into products with low gas adsorption ability limits its stability as a catalyst in its pure form. Additionally, the fast radiative recombination and low gas adsorption also affect the conversion efficiency of neat $MoS_2$.[173,174] Nevertheless, the practical applicability of $MoS_2$ towards the $CO_2$ reduction reaction can be improved by contributing to the role of exposed active sites on edge, defects and the terrace of the $MoS_2$. The formation of heterostructures with other 2D materials can also be an effective way for the efficient $CO_2$ reduction reaction. However, to date, there are only a few reports regarding the catalytic activity of $MoS_2$ as a photocatalyst towards the $CO_2RR$.

#### 4.3.1 Electrochemical $CO_2$ reduction.

Currently, the $CO_2$ reduction reaction through electrocatalysis is employed as the most efficient and long-term solution, which is clean, environmentally compatible and cost effective and is termed the electrochemical $CO_2$ reduction reaction ($CO_2RR$). For the electrochemical $CO_2$ RR, electrons are provided by the directly used electrical energy and the reduction abilities of electrons based on the applied voltage.[166] This process starts with the activation of an adsorbed $CO_2$ molecule upon electric energy treatment *via* the one-electron transfer pathway, producing the $CO_2^{\bullet -}$ intermediate. However, this step proceeds with a negative formal redox potential (−1.9 V *vs.* NHE), and hence is highly unfavourable and emerged as the rate-limiting step for the reduction reaction of $CO_2$. An alternative strategy to the one-electron process was established with a lower energetic cost to bypass the formation of the $CO_2^{\bullet -}$ intermediate, which is the so-called proton-assisted multiple-electron ($H^+/e^-$) transfer method, bearing a more positive thermodynamic value ($E^\circ$ = −0.20 V and −0.60 V). The overall $CO_2$ RR is governed through the formation of two primary reduction products such as CO and formate due to the reduction of $CO_2$ *via* the protonation of the oxygen atom and C atom of $CO_2$, respectively. The reduction of $CO_2$ to value-added hydrocarbon products is the fission and coupling of the C–O and C–C bond, respectively. Based on the number of protons and electrons transferred, the reduction of $CO_2$ results in different carbon-based products with different redox potentials. eqn (17)–(22) represent the various intermediates and products formed due to the activation and reduction of $CO_2$ together with corresponding redox potential values at NHE.[4,166,175,176]

$$CO_2 + e^- \rightarrow CO_2^- \quad E^{\ominus}_{\text{Redox}} = -1.9\,\text{V} \tag{17}$$

$$CO_2 + 2H^+ + 2e^- \rightarrow HCOOH \quad E^{\ominus}_{\text{Redox}} = -0.61\,\text{V} \tag{18}$$

$$CO_2 + 2H^+ + 2e^- \rightarrow CO + H_2O \quad E^{\ominus}_{\text{Redox}} = -0.53\,\text{V} \tag{19}$$

$$CO_2 + 4H^+ + 4e^- \rightarrow HCHO + H_2O \quad E^{\ominus}_{\text{Redox}} = -0.48\,\text{V} \tag{20}$$

$$CO_2 + 6H^+ + 6e^- \rightarrow CH_3OH + H_2O \quad E^{\ominus}_{\text{Redox}} = -0.38\,\text{V} \tag{21}$$

$$CO_2 + 8H^+ + 8e^- \rightarrow CH_4 + 2H_2O \quad E^{\ominus}_{\text{Redox}} = -0.24\,\text{V} \tag{22}$$

In comparison to the traditionally used noble metals, $MoS_2$ acts as a promising cost-effective substitute for a superior $CO_2$ electrochemical reduction performance. The high current density and low overpotential associated with the $CO_2RR$ are mainly due to the molybdenum-terminated edges and the catalytic performance is due to the high d-electron density and metallic character of $MoS_2$.[177]

Lv *et al.* exfoliated bulk $MoS_2$ into the nanosheet form by ball-milling followed by CVD and observed that the latter showed greater $CO_2$ reduction activity. The exfoliated few-layer $MoS_2$ nanosheets reduced $CO_2$ to CO with a current density of 61 mA $cm^{-2}$ at 1.1 V together with a faradaic efficiency of up to 41.2% at −0.9 V. The lower onset potential of ultrathin $MoS_2$ (−0.43 V) in comparison to bulk $MoS_2$ (−0.30 V) indicates a lower overpotential requirement for the reduction over the exfoliated form. They observed that the percentage of 1T-phase in the exfoliated $MoS_2$ was much larger than its bulk form. Hence, decreasing the thickness of $MoS_2$ can significantly increase its reduction ability. The mechanism behind the production of CO followed by the desorption of CO* on the surface of $MoS_2$ is clearly shown in Fig. 13a and b, respectively. According to this figure, it was deduced that the catalytic site of $MoS_2$ is the highly active Mo atoms on which $CO_2$ is easily adsorbed after combining with $H^+/e^-$. Conversely, $MoS_2$ possessing $\Delta G$ = 0.72 eV facilitates the easy desorption of CO* from its surface, resulting in the formation of products.[178] The production of liquid hydrocarbon-containing products such as 1-propanol from $CO_2RR$ regulated through a high proton–electron process, *i.e.*, 18 $H^+$ and 18 $e^-$, is kinetically challenging as the formation of two C–C bond is achieved. In addition, experimental studies revealed that during the electrochemical $CO_2$ RR, water reduction to $H_2$ evolution dominates over the $CO_2$ reduction process given that water is present at a higher concentration compared to dissolved $CO_2$ with a relatively low concentration. Accordingly, Francis and his group derived single-crystal $MoS_2$, which yielded 1-propanol from $CO_2$ in an aqueous electrolytic environment. Simultaneously, together with $CO_2$ reduction, hydrogen was also produced by the reduction of water as the dominant electrolysis product. To gain insight into the selective production of 1-propanol over hydrogen evolution for a single-crystal $MoS_2$ terrace, Fig. 13c provides the current density value *via* LSV measurement in both a $CO_2$ environment ($CO_2$ saturated electrolyte) and $N_2$ environment ($N_2$-purged phosphate buffer). The results indi-

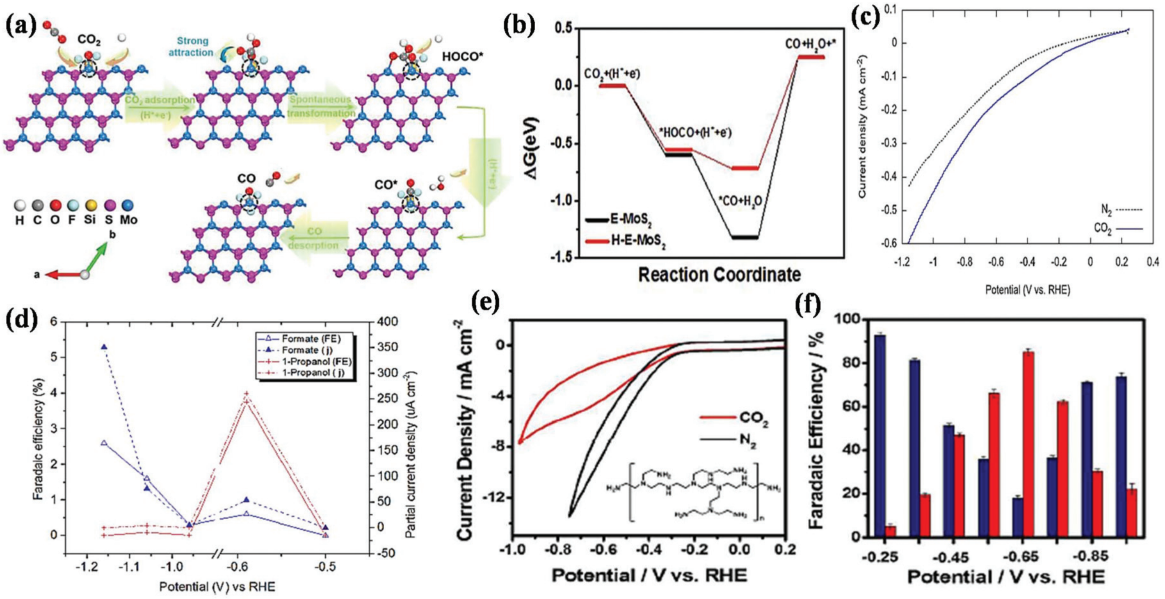

**Fig. 13** (a) Schematic illustration of mechanism for the formation of CO over H-E-$MoS_2$ monolayers (Mo atoms are the catalytic sites represented by a dashed circle) and (b) free energy graph calculation for $CO_2$ electroreduction to CO. Reproduced with permission.[178] (c) Comparison of LSV data for an $MoS_2$ single crystal in an $N_2$ or $CO_2$ environment and (d) potential-regulated partial current densities (dashed lines) and faradaic efficiencies (solid lines) of the $CO_2R$ products. Reproduced with permission.[179] (e) CV plot over rGO-PEI-$MoS_x$-modified GCE in $CO_2$-saturated (red curve) $N_2$-saturated (black curve), with a scan rate of 50 mV $s^{-1}$ and (f) faradaic efficiency graph of CO (red bars) and $H_2$ (blue bars). Reproduced with permission.[180]

cate that the cathodic current obtained under the $CO_2$ atmosphere is larger than that observed under the $N_2$ atmosphere, which suggests that the reduction of $CO_2$ is dominant over $H_2O$ reduction on the $MoS_2$ single-crystal terrace. However, the production of 1-propanol was found to be larger for both the single $MoS_2$ crystal and $MoS_2$ thin film with low edge densities rather than that for the thin film containing high edge site densities. Thus, it was concluded that for the reduction of $CO_2$ to 1-propanol, the $MoS_2$ surface terrace is responsible not the edges of the thin-film $MoS_2$. Experimentally, the $MoS_2$ single crystal terrace displayed a faradaic efficiency of 3.5% at an applied potential of −0.59 V (*vs.* RHE) for the conversion of $CO_2$ to 1-propanol, and that obtained for the $MoS_2$ thin film with low edge site densities was around 1%. The experiment also revealed that together with 1-propanol as the major product, other minor products such as formate, ethylene glycol, and t-butanol are produced. The faradaic efficiency and the current density of major product, *i.e.*, 1-propanol, together with formate are illustrated in Fig. 13d. Based on the experimental condition, it was concluded that production of 1-propanol involves the disulfidization of $MoS_2$ followed by the coupling of intermediate species on the surface of the $MoS_2$ single-crystal terrace.[179]

Li *et al.* fabricated amorphous 2D-molybdenum sulfide ($MoS_X$) on a polyethyleneimine (PEI)-modified rGO substrate and tested its $CO_2$ reduction ability in aqueous $NaHCO_3$ medium with high efficiency and selectivity. As revealed in Fig. 13e and f, the as obtained 2D/2D material selectively reduced $CO_2$ to CO with a very low overpotential of 140 mV, while the maximum faradaic efficiency of 85.1% for the product was obtained at −0.65 V (RHE) with a TOF value of 2.4 $s^{-1}$. They found that the PEI layer plays a major role in enhancing the catalytic activity of MoSx by suppressing the HER and stabilizing the $CO_2$ intermediate during $CO_2$ reduction.[180]

**4.3.2 Photocatalytic $CO_2$ reduction reaction.** The photocatalytic $CO_2$ reduction process is mainly governed through 5 sequential steps: (i) production of electrons and holes under the absorption of a photon by a semiconductor possessing a suitable band structure to dynamically and favorably reduce and oxidize $CO_2$ and $H_2O$, respectively. From the experimental interpretation, the estimated bandgap is considered to be 1.8–2.0 eV. In addition, it is also noted that the VB edge of the semiconductor photocatalyst should be more positive than the redox potential required for the water oxidation reaction, and similarly, the potential edge of the CB should be more negative than the redox potential for the $CO_2$ reduction. Thus, in the case of the photocatalytic $CO_2$ RR, the electrons are mainly generated by light excitation and the reduction abilities of the electrons rely on the potential of the conduction band. (ii) The second step involves the inhibition of the recombination process by separating photogenerated electron–hole pairs. (iii) In this step, the adsorption of a $CO_2$ molecule on the surface of the photocatalyst takes place followed by the transfer of an electron from the catalytic surface to the $CO_2$ molecule for the reduction process. For the adsorption of more $CO_2$, the photocatalyst should possess a high surface area and abundant active sites. (iv) The process involves the surface redox reaction originating from two different half reactions driven by the photogenerated electrons and holes. In this step, the holes oxidize water to molecular oxygen and electrons reduce $CO_2$ to various hydrocarbons such as $CH_4$, CO, $CH_3OH$, and HCOOH, as described in the earlier equations. This step is purely interconnected between photocatalysis and electrocatalysis and (v) the last step is the desorption of products within a particular time, and if the product is not released in time from the surface of the catalyst, then the catalyst becomes poisoned.[4,181]

Due to the insufficient reduction potential required for converting $CO_2$ into hydrocarbons, the $MoS_2$ photocatalyst exhibits negligible activity towards $CO_2$ reduction. Indeed, Geioushy and co-workers developed a 2D structured $MoS_2$ sheet by employing a hydrothermal method followed by annealing. The photoreduction of $CO_2$ proceeded under UV light irradiation and the formation of product, *i.e.*, methanol and acetaldehyde, with hydrocarbon selectivity was controlled by choosing a different aqueous solution such as 0.5 M $NaHCO_3$, NaOH and NaCl. The as-fabricated 2D $MoS_2$ with a stacked-layer exhibited superior $CO_2$ photoreduction conversion to different hydrocarbons such as methanol of 109.5 μmol $g^{-1}$ (in 0.5 M $NaHCO_3$ aqueous solution) and acetaldehyde of 19.2 μmol $g^{-1}$ (in 0.5 M NaCl aqueous solution), as shown in Fig. 14a. The

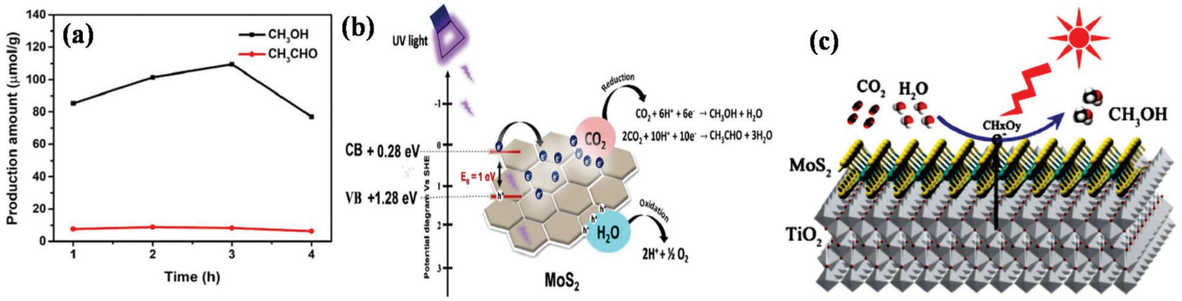

Fig. 14 (a) Rate of $CO_2$ reduction by $MoS_2$ sheets in 0.5 M $NaHCO_3$ and (b) schematic representation of the mechanistic pathway for photocatalytic $CO_2$ reduction over $MoS_2$ sheets. Reproduced with permission.[173] (c) Schematic illustration of the photoreduction of $CO_2$ to $CH_3OH$ in the $MoS_2$/$TiO_2$ heterostructure. Reproduced with permission.[170]

variation in the different hydrocarbon products was mainly governed through the effect of the various solvents used as the scavenging unit. The selectivity of the product depends on the anion effect of the solvent, which delays the charge carrier recombination. It was observed that the use of 0.5 M $NaHCO_3$ solution resulted in the selectivity of $CO_2$ photoreduction towards the production of $CH_3OH$, accelerated through a 6-electron process. The selectivity for the production of $CH_3OH$ is attributed to the formation of $HCO_3^-$ ions, which inhibit the charge pair recombination and also initiate multiple reaction pathways originating from the production of various intermediates such as formate ions followed by formyl anion. Alternatively, the production of methanol can also proceed *via* a 10-electron process, which can be due to the dimerization of the intermediates. The overall $CO_2RR$ reaction mechanism together with the reduction potential and multi-electron participation over the undecorated 2D $MoS_2$ sheet is depicted in Fig. 14b. It was also observed that with a change in the solvent from $NaHCO_3$ to NaOH and NaCl, the production of methanol somewhat decreased followed by an increase in acetaldehyde upon $CO_2$ photoreduction. The anion, *i.e.*, $OH^-$ and $Cl^-$, present in the respective solvent behaves as a hole scavenger and efficiently separates the photogenerated electron–hole pairs by accumulating more electrons on the $MoS_2$ surface for the dimerization of two carbon species, resulting in the formation of $CH_3CHO$. The high photocatalytic performance is attributed to the 2D structure morphology of $MoS_2$, which boosts the transportation of electrons throughout the $MoS_2$ sheet and also facilitates the reduction of adsorbed $CO_2$ molecules.[173]

Further, Tu *et al.* designed a 2D $MoS_2/TiO_2$ hybrid nanojunction, in which 2D-$MoS_2$ nanosheets were grown on a $TiO_2$ nanosheet *via* an *in situ* method. The as-fabricated 2D nanojunction exhibited enhanced and selective $CO_2$ photoreduction, resulting in $CH_3OH$ as the product in an aqueous $NaHCO_3$ solution. The photocatalytic performance was tested under UV-visible light with $CO_2$-saturated 1 M $NaHCO_3$ aqueous solution as the scavenger. The $MoS_2/TiO_2$ hybrid nanosheets with an $MoS_2$ content of 0.5 wt% selectively produced 10.6 $\mu mol\ g^{-1}\ h^{-1}$ of $CH_3OH$, which is 2.9 times greater than that for $TiO_2$. The high photocatalytic efficiency is due to the unique coupling of $MoS_2$ and $TiO_2$ and the presence of Mo-terminated edges, which make it somewhat metallic, and also due to the presence of a high d-electron density, stabilizing the CHxOy intermediate during the $CO_2RR$ under UV-Vis light illumination *via* electrostatic attraction. This type of 2D/2D hybrid nanojunction creates a compact contact, which is beneficial for the quick transfer of photogenerated electrons from $TiO_2$ to the Mo sites of $MoS_2$ with a high d-electron density to enhance the lifetime of the charge carriers and reduction efficiency. The mechanism for photoreduction involves the binding of negatively charged intermediate species such as $HCOO^-$ and $CHO^-$ with the positively charged Mo cations through electrostatic attraction. The $CO_2$ reduction performance was also compared with the novel metal-loaded $TiO_2$ nanosheets, but the rate of reduction of $CO_2$ to the main product was lower than that for $MoS_2$-loaded $TiO_2$. The overall $CO_2$ reduction mechanism is schematically illustrated in Fig. 14c.[170]

To achieve an ideal bandgap and exposed active sites towards superior photocatalytic $CO_2$ reduction to value-added hydrocarbons, interfacial engineering between two 2D layered materials has emerged as a productive strategy. Qiu and co-workers employed electrostatic self-assembly as a cost-effective strategy for developing a series of 2D layered LDH-$MoS_2$ heterostructured nanocomposites, providing a novel route to produce syngas with tunable a $H_2$:CO proportion *via* $CO_2$ photoreduction under visible light irradiation. The electrostatic interaction is created throughout the reaction by the combination of positively charged LDH with the negatively charged surface of $MoS_2$, which provides a large interface for the $CO_2RR$, and by controlling the interface-rich heterostructure catalyst concentration, the production of the syngas ($H_2$:CO) proportion can be tuned. The experiment revealed that both LDH and $MoS_2$ individually were unable to produce syngas with a modulated $H_2 : CO$ proportion; however, with a change in the loading percentage of $MoS_2$ from 0.1 to 0.3 in the LDH/$MoS_2$ heterostructure, the $H_2$:CO proportion was modulated, and with 0.30%, the proportion changed from 1 : 1 to 9 : 1. The origin of CO production from $CO_2$ was traced *via* a $^{13}CO_2$ isotopic experiment and analyzed through GC-MS spectrometry based on the signal obtained at $m/z = 29$, which is attributed to $^{13}CO$. In addition, the overall experiment was conducted in the presence of a photosensitizer ($H_2O$/acetonitrile with $[Ru(bpy)_3]Cl_2 \cdot 6H_2O$) and sacrificial agent (TEOA), which accelerate the $CO_2$ photoreduction mechanism. Theoretical calculation of the binding energy and DFT calculation were employed to determine the charge transfer between the heterojunction and structure–activity relationship during the $CO_2$ photoreduction. The lower work function value of LDH (3.946 eV) than that of $MoS_2$ (5.92 eV) suggests that the flow of electron occurs from LDH to $MoS_2$ through the Mo–O–S chemical bond to maintain the equilibration of the Fermi level. A new type of charge distribution suggested electron accumulation near the LDH surface and predicted the flow of electrons from $MoS_2$ to the LDH surface. Moreover, the narrower bandgap energy observed *via* DOS calculation for the $MoS_2$/LDH heterojunction indicates the strong interaction between LDH and $MoS_2$. Prior to light illumination, firstly, photogenerated electrons are excited from the HOMO to LUMO of the Ru complex and then transferred to the CB of the LDH and $MoS_2$ *via* the interface and selectively reduce $CO_2$ to CO at the LDH surface and $H_2$ at both the LDH and $MoS_2$ surface by coupling with active hydrogen species.[182] Besides, Kumar *et al.* designed an advanced functionalized nanomaterial, *i.e.*, pyrrole-promoted RGO-$MoS_2$ nanocomposite, for the efficient photoreduction of $CO_2$ into solar fuels and observed superior photocatalytic $CO_2$ reduction.[183] In comparison, Xu *et al.* fabricated a 1D/2D $TiO_2/MoS_2$ hybrid nanostructure in which a 2D-$MoS_2$ sheet vertically and uniformly covered 1D-$TiO_2$ electrospun fibres, which exhibited superior activity for $CO_2$ reduction to $CH_3OH$ and $CH_4$ under UV-visible light irradiation. The developed 1D/2D nanohybrid achieved the production rate of 2.6 and 2.55 μmol $g^{-1}$ $h^{-1}$, corresponding to $CH_4$ and $CH_3OH$, respectively, together with an apparent quantum yield of 0.16%. The photocatalytic activity is attributed to the presence of 2D-$MoS_2$, which enhances the light-harvesting properties of $TiO_2$ by increasing its absorption range.[184] In addition, other 2D–3D ($MoS_2$/SiC[185] and $MoS_2$/$TiO_2$[186]) have also been investigated for their $CO_2$ reduction activity; however, 2D–2D $MoS_2$-based materials for $CO_2$ reduction not been researched on a large scale.

### 4.3 Other applications of 2D $MoS_2$ and $MoS_2$-based 2D/2D heterostructures

In addition to energy conversion, other practical applications over $MoS_2$ have also been reported. To date, 2D-$MoS_2$ has been extensively applied for the photodegradation of various pollutants, antibiotics and dyes due to its absorption properties in a wide range of light, strong absorptivity properties, non-toxicity, stability against corrosion and environmentally friendly nature.[47] Ji and co-workers constructed a 2D/2D $MoS_2$/$CeO_2$ heterojunction photocatalyst,[102] which exhibited stronger degradation ability (88.5% in 120 min) than its neat counterpart with a huge reduction in the intensity of the peak in the UV-Vis spectrum with time, which shifted from 277 nm to 260 nm. In addition, the high surface to volume ratio, rapid response with improved sensitivity and low power consumption behaviour of 2D-$MoS_2$ materials have stimulated substantial research for different sensing applications such as biosensors, chemical sensors, electrochemical sensors, and gas sensors.[187] Hwang and co-workers developed a vertically aligned 2D-$MoS_2$ nanofilm with highly exposed Mo and S dangling bonds through the CVD method and tested it for the detection of heavy metals ($Pb^{2+}$) in tap water.[188] The material exhibited superior detection sensitivity with a limit of detection of 0.3 ppb at 180 s deposition time with a relative standard deviation of 3.1%. Again, various gas molecules such as NO, $H_2$, and $NH_3$ can be easily adsorbed on the surface of $MoS_2$. Additionally, 2D-$MoS_2$-based heterostructures have also been explored for the detection of different biomolecules and analytes in the environment. More importantly, in dye-sensitized solar cells (DSSCs), 2D-$MoS_2$ has exhibited superior performances due to its high electrocatalytic activity and high conductivity. Vikraman *et al.* fabricated a highly efficient layered $MoS_2$ counter electrode, which acts as a low-cost alternative to Pt-based DSSCs. Under 100 mW $cm^{-2}$ (AM 1.5) stimulated solar irradiation, a high power conversion efficiency of 7.14% was achieved, which is nearly equal to that of 8.73% observed for the Pt/FTO counter electrode through the reduction of triiodide to iodide.[189]

Furthermore, 2D-$MoS_2$ has been extensively investigated for its application in electronic devices as a channel material mainly due to its atomically thin structure, which exhibits exceptional electronic properties including variable band gap and suitable charge carrier mobility.[190,191] Due to the presence of a band gap in 2D-$MoS_2$ compared to bulk $MoS_2$, its conductivity can be modulated, which is feasible for the electrostatic control of this material and make it a suitable candidate for application in the field of electronic devices, especially field-effect transistors (FETs) and low-power electronic devices.[192] It has been demonstrated that 2D-$MoS_2$ as an FET at room temperature exhibited an on/off drain current ratio of $10^8$ with an enhancement in mobility of up to 200 $cm^2$ $(V\ s)^{-1}$.[193] Inspired by its direct band gap (~1.9 eV) with semiconducting behaviour and excellent mechanical properties such as flexibility and stretchability, 2D-$MoS_2$ is attracting great attention in the area of optoelectronic devices such as light sensing photodetectors, LEDs, and solar cells.[194,195] Zhai *et al.* designed an $NiTe_2$/$MoS_2$ 2D/2D vertical heterostructure towards the study of a back-gated FET and photodetector as an electronic and optoelectronic device, respectively. The as-obtained stack layered materials resulting from the van der Waals epitaxial heterostructure provided enhanced electronic contact at the heterointerface, which enhanced the optoelectronic responses by 5 times and the electronic behaviour compared to that of neat $MoS_2$.[98] Besides, 2D-$MoS_2$ is widely used in the field of energy storage devices especially in supercapacitor applications due to its tunable interlayer distance and long cycle durability. The presence of a stacked-lamellar sheet-like structure together with suitable oxidation states over Mo, *i.e.*, +2 and +6, 2D-$MoS_2$ exhibits electrical double layer capacitance behavior. Considering that the van der Waals attraction present between the stacked layers is weak, the various guest components such as ions/electrons can be easily intercalated throughout the layer, thus increasing the charge discharge behaviour of the material together with its capacitance.[196,197] A novel intercalated nanostructured fibre electrode was developed by Wang *et al. via* the combination of $MoS_2$ sheets, which exhibited a high pseudocapacitance value, with graphene with high electrical conductivity. The aforementioned graphene/$MoS_2$ fibre electrode with an intercalated nanostructure possessed a high ion-accessible surface area, resulting a high specific capacitance of 368 F $cm^{-3}$ at a current density of 0.1 A $cm^{-3}$ when the $MoS_2$ content was up to 33.98%. In addition, the fibre electrode exhibited cycle stability of 80% for 8000 cycles with a current density of 12.8 mW h $cm^{-3}$.[198] Moreover, recently, Kirubasankar and co-workers constructed a 2D $MoS_2$/MXene nanohybrid interlayer structure, which restricted the electrostatic attraction and prevented the self-stacking of individual layers, thus providing high mass transfer between the electrolyte-electrode interface. The $MoS_2$/MXene nanohybrid presented a superior specific capacitance about 583 F $g^{-1}$ with a rate capability of 2.5% at 1 A $g^{-1}$ and 96.5% cycle stability up to 5000 cycles at 5 A $g^{-1}$.[199] The various photocatalytic and electrocatalytic applications towards energy conversion using 2D-$MoS_2$ and its 2D/2D heterostructures are presented in Table 1.

**Table 1** Summary of the various applications of 2D-$MoS_2$ and $MoS_2$-based 2D/2D heterostructures

| Photocatalyst | Synthesis method | Amount of photocatalyst and volume of sacrificial agent | Irradiation light source | Rate of hydrogen evolution | Apparent quantum yield/ Efficiency (AQY/AQE) | Ref. |
|---|---|---|---|---|---|---|
| **(i) Photocatalytic hydrogen evolution reaction** | | | | | | |
| Few-layer $MoS_2$ nanosheets | Facile solvothermal treatment coupled with the liquid exfoliation strategy | 50 mg in 100 mL of aqueous solution containing 0.35 M $Na_2S$ and 0.25 M $Na_2SO_3$ | 300 W Xe | 1241.3 mmol $g^{-1}$ $h^{-1}$ | — | 138 |
| Few-layer $MoS_2$ nanosheets | Liquid-phase exfoliation strategy | 3 mg in 15% TEOA aqueous solution | 300 W Xenon lamp | 0.5 mmol$g^{-1}$ $h^{-1}$ | — | 139 |
| In-plane multiphasic 2D $MoS_2$ nanosheets | Chemical intercalation method | 40 mg in 40 mL of deionized water with 0.01 M lactic acid | 200 W Hg lamp | 1.5 mmol $h^{-1}$ $g^{-1}$ | AQY = 12.90% | 130 |
| $MoS_2$/CdS | *Ex situ* adsorption-calcination | 10 mg in 20 mL $H_2O$ + 5 mL lactic acid | 300 W Xenon lamp ($\lambda \geq 420$ nm) | 18.43 mmol $h^{-1}$ $g^{-1}$ | AQE = 3.4% | 92 |
| $MoS_2$/g-$C_3N_4$ | *Ex situ* | 50 mg in 200 mL of 10 vol% glycerol solution | 500 W Xenon lamp | 10 000 μmol $h^{-1}$ $g^{-1}$ | — | 200 |
| $MoS_2$/g-$C_3N_4$ | *Ex situ* ultrasonic assisted strategy | 20 mg in 20 mL water/methanol (4 : 1 v/v) solution | 300 W Xenon lamp | 1497 μmol $h^{-1}$ $g^{-1}$ | AQY = 3.3% | 121 |
| $ZnIn_2S_4$/$MoS_2$ | *Ex situ* electrostatic self-assembly process | Lactic acid | Visible light | 4.974 mmol $g^{-1}$ $h^{-1}$ | — | 95 |
| Black phosphorous/ $MoS_2$ | *In situ* solvothermal method | 10 mg in 250 mL of 0.1 M $Na_2S$ and 0.1 M $Na_2SO_3$ aq. solution | 300 W Xenon lamp | 1286 μmol $h^{-1}$ $g^{-1}$ | AQY = 1.2% | 103 |
| $MoS_2$/$Ti_3C_2$ | *In situ* hydrothermal method | 30 mg in 50 mL of methanol solution | 300 W Xenon lamp | 6144.7 mmol $g^{-1}$ $h^{-1}$ | — | 201 |
| $MoS_2$/CdS | *In situ* hydrothermal method | 50 mg in 250 mL 0.4 M $Na_2S$ and 0.4 M $Na_2SO_3$ solution | 300 W Xenon lamp | 26.32 mmol $h^{-1}$ $g^{-1}$ | AQY = 46.65% | 141 |
| $MoS_2$/g-$C_3N_4$ | *In situ* probe sonication-assisted liquid exfoliation | 50 mg in 250 mL of 0.1 M TEOA aqueous solution | 300 W Xenon lamp | 1155 μmol $h^{-1}$ $g^{-1}$ | AQY = 6.8% | 142 |
| $MoS_2$/$SnNb_2O_6$ | *In situ* Hydrothermal method | 50 mg in 50 mL of 20 vol% methanol. | 300 W Xenon arc lamp | 12.9 μmol $h^{-1}$ | — | 202 |
| $CoMoS_2$/rGO/$C_3N_4$ | *In situ* solvothermal method | 100 mg in a mixed solution of TEOA and $H_2O$ (volume ratio equal to 1/5) | 300 W Xenon lamp | 684 μmol $g^{-1}$ $h^{-1}$ | — | 203 |
| g-$C_3N_4$/graphene/$MoS_2$ | *In situ* hydrothermal method | 50 mg in 250 mL of 0.1 M TEOA solution | 300 W Xenon lamp | 317 μmol $g^{-1}$ $h^{-1}$ | AQY = 3.4% | 143 |
| $Ti_3C_2$ MXene/$MoS_2$/$TiO_2$ | *In situ* two-step hydrothermal | 10 mg in aqueous acetone with dissolved sacrificial reagent (TEOA) | 300 W Xenon lamp | 6425.297 μmol $h^{-1}$ $g^{-1}$ | AQY = 4.61% | 204 |
| S-Doped polymeric carbon nitride/$MoS_2$ | One-pot hydrothermal-polymerization method | 50 mg in 10 vol% TEOA aq. solution | 300 W Xenon lamp | 2120 μmol $h^{-1}$ $g^{-1}$ | AQE = 5.7% | 110 |
| N-Doped $MoS_2$/S-doped g-$C_3N_4$ | One-step thermal polycondensation method | 50 mg in 100 mL 10 vol% TEOA | 300 W Xenon lamp | 658.5 μmol $g^{-1}$ $h^{-1}$ | — | 205 |
| $MoS_2$/$CeO_2$ | *In situ* hydrothermal | 20 mg in 20 mL of 10 vol% methanol | 150 W xenon lamp | 508.44 μmol $h^{-1}$ | — | 89 |
| $MoS_2$/$CaIn_2S_4$ | *In situ* hydrothermal | 20 mg in 20 mL of 0.025 M $Na_2S$ and 0.025 M $Na_2SO_3$ aq. solution | 150 W xenon arc lamp | 602.35 μmol $h^{-1}$ | Apparent Conversion Efficiency = 9.71% | 76 |
| $MoS_2$/$ZnIn_2S_4$ | One-pot hydrothermal | 20 mg in 20 mL of 0.25 M $Na_2SO_3$ and 0.35 M $Na_2S$ aq. solution | 150 W xenon arc lamp | 379.1 μmol $h^{-1}$ | Apparent Conversion Efficiency = 6.07% | 115 |
| $MoS_2$/NiFe LDH | *In situ* electrostatic self-assembled chemistry | 30 mg in 30 mL of 10 vol% $CH_3OH$ aq. solution | 125 W medium pressure Hg lamps | 550.9 μmol $h^{-1}$ | — | 104 |
| $MoS_2$/$MgIn_2S_4$ | *In situ* hydrothermal method | 20 mg in 20 mL of 0.25 M $Na_2SO_3$ and 0.35 M $Na_2S$ aq. solution | 150 W Xenon arc lamp | 570.8 μmol $h^{-1}$ | — | 90 |
| UiO-66-$NH_2$ MOF/$MoS_2$ | *In situ* hydrothermal method | 20 mg in 20 mL of 10% methanol solution | 300 W Xe arc lamp | 512.9 μmol $h^{-1}$ | Apparent Conversion Efficiency = 3.84% | 113 |
| P-$MoS_2$/CdS | *In situ* hydrothermal | 10 mg in 100 mL of 0.35 M $Na_2S$ and 0.25 M $Na_2SO_3$ | 300 W Xe lamp | 58.9 μmol $h^{-1}$ | AQE = 19.0% | 206 |
| $MoS_2$/Co–Al LDH | *In situ* hydrothermal | 50 mg in 80 mL methanol solution | 300 W Xe lamp | 17.1 μmol $g^{-1}$ $h^{-1}$ | — | 207 |

**Table 1** *(Contd.)*

| Photocatalyst | Synthesis method | Amount of photocatalyst and volume of sacrificial agent | Irradiation light source | Rate of hydrogen evolution | Apparent quantum yield/ Efficiency (AQY/AQE) | Ref. |
|---|---|---|---|---|---|---|
| $MoS_2$/g-$C_3N_4$ | *In situ* solvothermal | 5 mg in 40 mL of 10% TEOA solution | 300 W Xenon arc lamp | 1787 μmol $h^{-1}$ $g^{-1}$ | — | 208 |

| Catalyst | Synthesis process | Electrolyte | Current Density (mA $cm^{-2}$) | Over-potential (mV) | Tafel slope (mV $dec^{-1}$) | Ref. |
|---|---|---|---|---|---|---|
| **(ii) Electrocatalytic hydrogen evolution reaction** | | | | | | |
| Defect-rich $MoS_2$ nanowall | Hydrothermal | 0.5 M $H_2SO_4$ | 10 | 95 | 78 | 135 |
| Fractal-shaped single-layer $MoS_2$ | CVD method | 0.5 M $H_2SO_4$ | 10 | 185 | 45 | 84 |
| Single-atom metal-doped $MoS_2$ | One-pot hydrothermal method | 0.1 M $H_2SO_4$ | 10 | 60 | 96 | 209 |
| $MoS_2$ nanosheets | Hydrothermal followed by annealing process | 0.5 M $H_2SO_4$ and 1 M KOH | 10 mA $mg^{-1}$ | (i) Acidic = 171 (ii) alkaline = 162 | (i) Acidic = 54 (ii) alkaline = 68 | 133 |
| Surfactant-exfoliated 2D molybdenum disulphide | Liquid-phase exfoliation | 0.5 M $H_2SO_4$ | −4.96 | 420 | 94 | 210 |
| 2D $MoS_2$ nanosheets | Hydrothermal method | 0.5 M $H_2SO_4$ | 25 | 280 | 90 | 88 |
| 2D $MoS_2$ Thin Films | CVD | 0.5 M $H_2SO_4$ | 60 | 640 | 90 | 85 |
| $FePS_3$/$MoS_2$ | *In situ* Hydrothermal method | 1 M KOH solution and 0.5 M $H_2SO_4$ solution | 10 | (i) 1 M KOH = 175 (ii) 0.5 M $H_2SO_4$ = 168 | (i) 1 M KOH = 127 (ii) 0.5 M $H_2SO_4$ = 107 | 211 |
| Co-BDC/$MoS_2$ | *In situ* sonication-assisted solution strategy | 1 M KOH solution | −10 | 248 | 86 | 134 |
| MoP/$MoS_2$ | *In situ* Phosphorization | 0.5 M $H_2SO_4$, 1 M phosphate buffered solutions (PBS) and 1 M KOH | 10 | (i) Neutral = 96 (ii) alkaline = 54 (iii) acidic = 69 | (i) Neutral = 48 (ii) alkaline = 58 (iii) acidic = 61 | 106 |
| $MoS_2$/black phosphorus | *In situ* | 0.5 M $H_2SO_4$, 1 M KOH and 1 M PBS | 10 | (i) Neutral = 258 (ii) alkaline = 237 (iii) acidic = 126 | (i) Neutral = 154 (ii) alkaline = 99 (iii) acidic = 68 | 136 |
| $MoS_2$/N-doped graphdiyne | *In situ* solvothermal method | 0.5 M $H_2SO_4$ | 10 | 186 | 63 | 212 |
| $MoS_2$/graphene | *In situ* self-assembly method *via* electrostatic attraction | 0.5 M $H_2SO_4$ and 1.0 M KOH | 10 | (i) Acidic = 180 (ii) alkaline = 183 | (i) Acidic = 79 (ii) alkaline = 127 | 73 |
| $MoS_2$/graphene | *Ex situ* two-step sonication method | 6 M KOH | 25 | 125 | 41 | 213 |
| RGO/$MoS_2$ | One-step hydrothermal method | 0.5 M $H_2SO_4$ solution | 100 | 150 | 52.5 | 214 |
| $MoS_2$/graphene | One-step *in situ* solvothermal | 0.5 M $H_2SO_4$ | 10 | 94.2 | 140 | 215 |
| $MoS_2$/g-$C_3N_4$ | One-pot method | 0.5 M $H_2SO_4$ | 10 | 140 | 45 | 109 |
| $MoS_2$/carbon nitride | *In situ* hydrothermal | 0.1 M KOH | 10 | 153 | 43 | 61 |

| Photocatalyst | Synthesis method | Amount of photocatalyst and volume of sacrificial agent | Irradiation light source | Rate of $NH_3$ synthesis | Ref. |
|---|---|---|---|---|---|
| **(iii) Photocatalytic nitrogen reduction reaction** | | | | | |
| Ultrathin $MoS_2$ | Hydrothermal followed by ultra-sonication | 15 mg in 200 mL DI water + HCl solution (pH = 3.5) | 500 W Xenon lamp | 325 μmol $h^{-1}$ $g^{-1}$ | 50 |
| $MoS_2$/biochar | *In situ* | 20 mg in 100 mL of DI water | 300 W Xenon lamp | 37.878 μmol $g^{-1}$ $h^{-1}$ | 216 |
| $MoS_2$/$MgIn_2S_4$ | *In situ* two-step hydrothermal method | 15 mg in 50 mL distilled water + HCl solution (pH = 3.6) | 250 W Hg lamp | 2509.2 μmol $h^{-1}$ $g^{-1}$ | 90 |

| Catalyst | Synthesis method | Electrolyte | Rate of $NH_3$ evolved | Faradic efficiency (%) | Potential (V) | Ref. |
|---|---|---|---|---|---|---|
| **(iv) Electrocatalytic nitrogen reduction reaction** | | | | | | |
| 2D-$MoS_2$ | Hydrothermal followed by annealing method | 10 mg in 0.1 M $Li_2SO_4$ solution (pH = 3.0) | 43.4 μg $h^{-1}$ $mg^{-1}$ | 9.81 | -0.2 | 158 |
| $MoS_2$ | Hydrothermal method | 0.1 M $Na_2SO_4$. | $8.08 \times 10^{-11}$ mols$^{-1}$ $cm^{-1}$ | 1.17 | −0.5 | 117 |

**Table 1** *(Contd.)*

| Catalyst | Synthesis method | Electrolyte | Rate of $NH_3$ evolved | Faradic efficiency (%) | Potential (V) | Ref. |
|---|---|---|---|---|---|---|
| $MoS_2/C_3N_4$ | *In situ* | 0.1 M $Na_2SO_4$ | 19.86 μg $h^{-1}$ $mg^{-1}$ | 6.87 | −0.5 | 75 |
| $MoS_2$/RGO | *In situ* hydrothermal | 0.1 M $LiClO_4$ | 24.82 μg $h^{-1}$ $mg^{-1}$ | 4.58 | −0.45 | 160 |
| $MoS_2/C_3N_4$ | *In situ* hydrothermal | 0.1 M $LiClO_4$ solution | 18.5 μg $h^{-1}$ $mg^{-1}$ | 17.8 | −0.3 | 159 |

| Photocatalyst | Synthesis method | Amount of photocatalyst and volume of sacrificial agent | Light source | Main product | Yield | AQY/ AQE | Ref. |
|---|---|---|---|---|---|---|---|
| **(v) Photocatalytic carbon dioxide reduction** | | | | | | | |
| 2D-$MoS_2$ sheets | Hydrothermal followed by annealing method | 0.1 g in 50 mL 0.5 M (i) $NaHCO_3$, (ii) NaOH and (iii) NaCl aqueous solution | 150 W medium pressure mercury vapour lamp | (i) Methanol in 0.5 M $NaHCO_3$ (ii) Acetaldehyde in 0.5 M NaCl | (i) 109.5 μmol $g^{-1}$ (ii) 19.2 μmol $g^{-1}$ | — | 173 |
| Polypyrrole/ rGO-$MoS_2$ | *In situ* wet chemical synthesis | 50 mg in 20 mL of 0.5 M $NaHCO_3$ | 300 W Xenon lamp | (i) CO, (ii) $CH_4$ (iii) $H_2$ | (i) 3.95 μmol $g^{-1}$ $h^{-1}$ (ii) 1.50 μmol $g^{-1}$ $h^{-1}$ (iii) 4.19 μmol $g^{-1}$ $h^{-1}$ | AQE = 0.30% | 183 |
| $MoS_2$/g-$C_3N_4$ | *Ex situ* hydrothermal deposition method | 50 mg in 100 mL deionized water | 300 W Xenon lamp | CO | 58.59 μmol $g^{-1}$ for 7 h | AQY = 0.255% | 217 |
| $MoS_2/TiO_2$ | *In situ* hydrothermal | 0.1 g in 200 mL of 1 M $NaHCO_3$ solution (pH = 8) | 300 W xenon arc lamp | $CH_3OH$ | 10.6 μmol $h^{-1}$ $g^{-1}$ | — | 170 |
| LDH/$MoS_2$ | *Ex situ* electrostatic self-assembly | Photocatalyst (0.3 mg $mL^{-1}$) and $[Ru(bpy)_3]Cl_2$ × $6H_2O$ (3.3 mg) were suspended in 10 mL aqueous solution containing $H_2O : CH_3CN : TEOA = 1 : 3 : 1$ (V/V/V) | 300 W Xe lamp | (i) CO (ii) $H_2$ | (i) 3617 μmol $h^{-1}$ $g^{-1}$ (ii) 6187 μmol $h^{-1}$ $g^{-1}$ | — | 182 |

| Catalyst | Synthesis method | Electrolyte | Main product | Current density (mA $cm^{-2}$) | Faradic efficiency | Potential | Ref. |
|---|---|---|---|---|---|---|---|
| **(vi) Electrocatalytic carbon dioxide reduction** | | | | | | | |
| Hydrophobic exfoliated $MoS_2$ nanosheets | Ball-milling followed by CVD | 1-Ethyl-3-methylimidazolium tetrafluoroborate (EMIM-BF4) aqueous solution | CO | 61 | 81.2% at −0.9 V | −1.1 V | 178 |
| $MoS_2$ thin film | Mechanical exfoliation followed by CVD method | 0.10 M potassium phosphate buffer or 0.10 M sodium carbonate that was acidified to pH 6.8 | 1-Propanol | −0.1 | 3.5% | −0.59 V | 179 |
| rGO–PEI–MoSx | *In situ* electrodeposition method | 0.5 M aqueous $NaHCO_3$ | CO | 55 | 85.1% | 540 mV | 180 |

## 5. Conclusion and future perspectives

Over the past decade, the development of $MoS_2$-based materials and their chemistry have attracted significant interest for the photo/electro catalytic generation of energy from water, $N_2$ and $CO_2$. According to the recent reports, we found that in comparison to bulk $MoS_2$, ultra-thin two-dimensional $MoS_2$ with abundant active edge sites possesses extraordinary optical and electrochemical properties. Interestingly, for an efficient catalytic reaction, the two most common phases, *i.e.*, 1T and 2H, of $MoS_2$ are mainly responsible. The semiconducting 2H phase of 2D-$MoS_2$ with its nanostructured condition possesses a lower amount of catalytic active sites due to its inert basal plane, whereas the 1T phase exhibits more active sites. Thus, the crystal-phase engineering of 2D-$MoS_2$ from 2H to 1T through precise control of the transformation has achieved great results towards energy conversion applications such as water reduction reaction, nitrogen reduction reaction and $CO_2$ reduction reaction. In some cases, it was seen that phase engineering is responsible for the activation of the basal plane of $MoS_2$, which facilitates the adsorption of $H_2$, $N_2$ and $CO_2$ on its surface and is beneficial for achieving superior photo/electro catalytic activity. Although the metallic 1T phase possesses interesting properties, which are beneficial towards energy conversion reactions, its low stability at high temperature somewhat limits its activity. Due to the stability issue of the 1T phase of $MoS_2$, the coexistence of both 1T and 2H phases in one component through phase engineering has been developed in the catalysis field, but very little work has been reported on this to date. Currently, the maximum studies on 2D-$MoS_2$ are based on its most stable semiconducting phase, which makes it a good candidate in the field of both photo and electrocatalysis. However, among the many aspects of improving the catalytic activity of neat 2D-$MoS_2$, the formation of heterostructure of 2D-$MoS_2$ with other 2D-semiconductors/catalysts has attracted significant research interest. Therefore, in this review, we especially focused on the design of semiconducting 2D-$MoS_2$ with other 2D materials using various synthetic routes especially *ex situ*, *in situ* and one-pot strategies. Further, the photo and electrochemical activity towards energy production through water splitting, $CO_2$ reduction and $N_2$ fixation over 2D-$MoS_2$-based materials were discussed elaborately. The photocatalytic and electrocatalytic activity of the resulting 2D/2D heterostructure depend on the coupling interaction of semiconducting 2D-$MoS_2$ with other 2D materials. The powerful combination of two 2D materials is mainly governed through vertical and lateral interactions, forming a 2D/2D heterostructure. In contrast to 1D/2D- and 3D/2D-based structures, the 2D/2D combination-based heterostructure furnishes the largest degree of contact in the face-to-face fashion, which results in superior charge mobility throughout the interface.

- Challenges and opportunities

Although 2D-$MoS_2$-based 2D/2D heterostructured materials have achieved very encouraging progress in a wide range of fields from photocatalysis to electrocatalysis, some challenges remain, which demand an urgent solution. The various challenges and opportunities over $MoS_2$-based 2D/2D heterostructures are elaborately discussed in the following section. (i) Although many synthetic strategies have been developed for the synthesis of high quality, large surface area ultrathin $MoS_2$ nanosheet, the controlled synthesis of the desired layer with high charge carrier mobility of $MoS_2$ still needs further research attention. Furthermore, theoretical and practical research is needed for designing efficient lateral or vertical 2D/2D heterostructures with intimate contact and efficient interfacial coupling. (ii) Also, 2D-$MoS_2$-based heterostructures need low-cost synthetic methods for the large-scale production of 2D/2D catalysts. (iii) A thorough experimental and theoretical review regarding the activity improvement of 2D/2D-$MoS_2$-based materials has been presented. However, some fundamental aspects still need to be addressed to achieve the highest activity result in the target reaction. (iv) Although 2D-$MoS_2$ possesses edge-active sulfur sites, inert basal planes and high conductivity, $MoS_2$ nanosheet-based materials do not achieve the desired performance for electrocatalytic $H_2$ evolution. In addition, $MoS_2$ nanosheets generally show excellent hydrogen evolution activity in acidic medium, but the lack of expected performance in alkaline and neutral media restricts it as a versatile catalyst. Thus, more efforts and research are required for its further development. (v) The overall solar energy conversion efficiency of natural photosynthesis is much lower than 1%; however artificial photosynthesis can provide a great efficiency for solar energy conversion to fuel. Nevertheless, the selection of a photocatalytic system with long-term use and durability is very challenging. Hence, a conversion efficiency 10% or higher must be achieved for the process to be commercialized. $MoS_2$ provides a wide photon absorption range and generates multiple excitons, and thus can be an ideal candidate as a photocatalytic system for future use. 2D-$MoS_2$- and 2D/2D $MoS_2$-based materials have widely reported for photocatalysis, but the role of $MoS_2$ as a co-catalyst and primary catalyst has yet to be fully understood. In the case of the photocatalytic mechanism over 2D/2D heterostructures, although various charge transport and separation mechanisms across the 2D–2D junction have been proposed, some are still under debate due to the lack of solid theoretical evidence for the fundamental understanding of the mechanistic pathway. Thus, the importance of DFT studies regarding rational theoretical calculations should also emphasized in the photocatalytic reaction field. (vi) 2D-$MoS_2$-based materials have received eye-catching progress in the field of the nitrogen reduction reaction. Both the theoretical investigation and practical application suggest a good result in ammonia synthesis; however, product selectivity is still a major concern, given that hydrazine and other nitrogen oxide products compete with ammonia. Thus, a detailed theoretical analysis should be carried out to determine the reaction mechanism of nitrogen reduction over $MoS_2$-based materials. Considering the theoretical aspects, $MoS_2$ nanosheets and 2D–2D-coupled heterostructures should be designed with optimized parameters such as defect-rich $MoS_2$ or highly edge active Mo ions. (vii)

Although 2D-$MoS_2$ possesses interesting properties for the $N_2$ reduction reaction, its exploration in the photocatalytic nitrogen reduction field is limited. Thus, combining theoretical aspects with photocatalytic experiments needs more work this field. (viii) Although recent reports suggest the enhanced $CO_2$ reduction activity over $MoS_2$-based materials, very little work has been done in the field of photo and electrochemical $CO_2$ reduction. $MoS_2$ with active basal plane reaction sites for the $CO_2$RR and its coupling with other suitable $CO_2$ reduction catalysts may be a rising trend in this field. Hence, DFT studies should be firstly utilized to demonstrate the basic guidelines for designing of 2D-$MoS_2$-based materials with maximum catalytic sites for selective $CO_2$ reduction.

Finally, the scope of practical applications over $MoS_2$-based 2D/2D heterostructured materials can be further expanded to other field.

## Conflicts of interest

There are no conflicts of interest to declare.

## Acknowledgements

Authors are very much thankful to S'O'A management for their constant support and encouragement.

## References

1 P. Nejat, F. Jomehzadeh, M. M. Taheri, M. Gohari and M. Z. Muhd, *Renewable Sustainable Energy Rev.*, 2015, **43**, 843–862.
2 L. Suganthi and A. A. Samuel, *Renewable Sustainable Energy Rev.*, 2012, **16**, 1223–1240.
3 X. Li, J. Yu, J. Low, Y. Fang, J. Xiao and X. Chen, *J. Mater. Chem. A*, 2015, **3**, 2485–2534.
4 J. Wu, Y. Huang, W. Ye and Y. Li, *Adv. Sci.*, 2017, **4**, 1–29.
5 T. Hisatomi, J. Kubota and K. Domen, *Chem. Soc. Rev.*, 2014, **43**, 7520–7535.
6 Z. Wang, C. Li and K. Domen, *Chem. Soc. Rev.*, 2019, **48**, 2109–2125.
7 X. Chen, N. Li, Z. Kong, W. J. Ong and X. Zhao, *Mater. Horiz.*, 2018, **5**, 9–27.
8 J. Luo, S. Zhang, M. Sun, L. Yang, S. Luo and J. C. Crittenden, *ACS Nano*, 2019, **13**, 9811–9840.
9 J. Xiong, J. Di and H. Li, *Adv. Sci.*, 2018, **5**, 1800244.
10 J. Sun, F. Tian, F. Yu, Z. Yang, B. Yu, S. Chen, Z. Ren and H. Zhou, *ACS Catal.*, 2020, **10**, 1511–1519.
11 X. Yang and D. Wang, *ACS Appl. Energy Mater.*, 2018, **1**, 6657–6693.
12 S. Ikram, *Nano Res.*, 2016, **2**, 10.
13 M. Darwish and A. Mohammadi, *Nanotechnology in Environmental Science*, 2018, pp. 315–350.
14 R. Xu, L. Du, D. Adekoya, G. Zhang, S. Zhang, S. Sun and Y. Lei, *Adv. Energy Mater.*, 2020, 2001537.
15 W. Xu, Y. Bai and Y. Yin, *Adv. Mater.*, 2018, **30**, 1–7.
16 B. Dubertret, T. Heine and M. Terrones, *Acc. Chem. Res.*, 2015, **48**, 1–2.
17 J. Low, S. Cao, J. Yu and S. Wageh, *Chem. Commun.*, 2014, **50**, 10768–10777.
18 Z. Li, X. Zhang, H. Cheng, J. Liu, M. Shao, M. Wei, D. G. Evans, H. Zhang and X. Duan, *Adv. Energy Mater.*, 2020, **10**, 1–17.
19 Z. Hua, *ACS Nano*, 2015, **9**, 9451–9469.
20 B. Luo, G. Liu and L. Wang, *Nanoscale*, 2016, **8**, 6904–6920.
21 K. S. Novoselov, A. K. Geim, S. V. Morozov, D. Jiang, Y. Zhang, S. V. Dubonos, I. V. Grigorieva and A. A. Firsov, *Science*, 2004, **306**, 666–669.
22 R. Mas-Ballesté, C. Gómez-Navarro, J. Gómez-Herrero and F. Zamora, *Nanoscale*, 2011, **3**, 20–30.
23 S. Das, J. A. Robinson, M. Dubey, H. Terrones and M. Terrones, *Annu. Rev. Mater. Res.*, 2015, **45**, 1–27.
24 J. Di, C. Yan, A. D. Handoko, Z. W. Seh, H. Li and Z. Liu, *Mater. Today*, 2018, **21**, 749–770.
25 C. N. R. Rao, K. Gopalakrishnan and U. Maitra, *ACS Appl. Mater. Interfaces*, 2015, **7**, 7809–7832.
26 R. Lv, J. A. Robinson, R. E. Schaak, D. Sun, Y. Sun, T. E. Mallouk and M. Terrones, *Acc. Chem. Res.*, 2015, **48**, 56–64.
27 J. Theerthagiri, R. A. Senthil, B. Senthilkumar, A. Reddy Polu, J. Madhavan and M. Ashokkumar, *J. Solid State Chem.*, 2017, **252**, 43–71.
28 K. F. Mak, C. Lee, J. Hone, J. Shan and T. F. Heinz, *Phys. Rev. Lett.*, 2010, **105**, 2–5.
29 O. V. Yazyev and A. Kis, *Mater. Today*, 2015, **18**, 20–30.
30 M. Pumera, Z. Sofer and A. Ambrosi, *J. Mater. Chem. A*, 2014, **2**, 8981–8987.
31 Q. H. Wang, K. Kalantar-Zadeh, A. Kis, J. N. Coleman and M. S. Strano, *Nat. Nanotechnol.*, 2012, **7**, 699–712.
32 J. Huo, R. Ge, Y. Liu, J. Guo, L. Lu, W. Chen, C. Liu, H. Gao and H. Liu, *Sustainable Mater. Technol.*, 2020, **24**, e00161.
33 D. K. Nandi, U. K. Sen, D. Choudhury, S. Mitra and S. K. Sarkar, *Electrochim. Acta*, 2014, **146**, 706–713.
34 I. Song, C. Park and H. C. Choi, *RSC Adv.*, 2015, **5**, 7495–7514.
35 Y. Yu, G. H. Nam, Q. He, X. J. Wu, K. Zhang, Z. Yang, J. Chen, *et al.*, *Nat. Chem.*, 2018, **10**, 638–643.
36 Q. Ding, B. Song, P. Xu and S. Jin, *Chem*, 2016, **1**, 699–726.
37 H. Wang, C. Li, P. Fang, Z. Zhang and J. Z. Zhang, *Chem. Soc. Rev.*, 2018, **47**, 6101–6127.
38 X. Huang, Z. Zeng and H. Zhang, *Chem. Soc. Rev.*, 2013, **42**, 1934–1946.
39 U. Krishnan, M. Kaur, K. Singh, M. Kumar and A. Kumar, *Superlattices Microstruct.*, 2019, **128**, 274–297.
40 D. Wang, X. Zhang, S. Bao, Z. Zhang, H. Fei and Z. Wu, *J. Mater. Chem. A*, 2017, **5**, 2681–2688.
41 R. Ganatra and Q. Zhang, *ACS Nano*, 2014, **8**, 4074–4099.
42 T. A. Shifa, F. Wang, Y. Liu and J. He, *Adv. Mater.*, 2019, **31**, 1804828.

43 J. Kibsgaard, Z. Chen, B. N. Reinecke and T. F. Jaramillo, *Nat. Mater.*, 2012, **11**, 963–969.

44 A. B. Laursen, S. Kegnæs, S. Dahl and I. Chorkendorff, *Energy Environ. Sci.*, 2012, **5**, 5577–5591.

45 Z. Li, X. Meng and Z. Zhang, *J. Photochem. Photobiol., C*, 2018, **35**, 39–55.

46 C. Wu, J. Zhang, X. Tong, P. Yu, J. Y. Xu, J. Wu, Z. M. Wang, J. Lou and Y. L. Chueh, *Small*, 2019, **15**, 1–25.

47 Z. Wang and B. Mi, *Environ. Sci. Technol.*, 2017, **51**, 8229–8244.

48 Y. Liu, D. Huang, M. Cheng, Z. Liu, C. Lai, C. Zhang, C. Zhou, W. Xiong, L. Qin, B. Shao and Q. Liang, *Coord. Chem. Rev.*, 2020, **409**, 213220.

49 T. R. Thurston and J. P. Wilcoxon, *J. Phys. Chem. B*, 1999, **103**, 11–17.

50 S. Sun, X. Li, W. Wang, L. Zhang and X. Sun, *Appl. Catal., B*, 2017, **200**, 323–329.

51 F. Meng, J. Li, S. K. Cushing, M. Zhi and N. Wu, *J. Am. Chem. Soc.*, 2013, **135**, 10286–10289.

52 C. K. Sumesh and S. C. Peter, *Dalton Trans.*, 2019, **48**, 12772–12802.

53 J. Su, G. D. Li, X. H. Li and J. S. Chen, *Adv. Sci.*, 2019, **6**, 1–19.

54 P. Solís-Fernández, M. Bissett and H. Ago, *Chem. Soc. Rev.*, 2017, **46**, 4572–4613.

55 X. Zhang, X. Yuan, L. Jiang, J. Zhang, H. Yu, H. Wang and G. Zeng, *Chem. Eng. J.*, 2020, **390**, 124475.

56 Y. Li, C. Gao, R. Long and Y. Xiong, *Mater. Today Chem.*, 2019, **11**, 197–216.

57 X. Liu, Q. Zhang and D. Ma, *Sol. RRL*, 2021, **5**, 2000397.

58 T. Su, Z. Qin, H. Ji and Z. Wu, *Nanotechnology*, 2019, **30**, 502002.

59 M. M. Ayyub, R. Singh and C. N. R. Rao, *Sol. RRL*, 2020, **4**, 2000050.

60 S. Cao, B. Shen, T. Tong, J. Fu and J. Yu, *Adv. Funct. Mater.*, 2018, **28**, 1–11.

61 X. Qian, J. Ding, J. Zhang, Y. Zhang, Y. Wang, E. Kan, X. Wang and J. Zhu, *Nanoscale*, 2018, **10**, 1766–1773.

62 W. J. Ong and K. P. Y. Shak, *Sol. RRL*, 2020, **4**, 2000132.

63 W. J. Ong, *Front. Mater.*, 2017, **4**, 11.

64 H. Qi, L. Wang, J. Sun, Y. Long, P. Hu, F. Liu and X. He, *Crystals*, 2018, **8**, 35.

65 H. Hou, X. Zeng and X. Zhang, *Sci. China Mater.*, 2020, **2119**, 1–34.

66 T. Su, Q. Shao, Z. Qin, Z. Guo and Z. Wu, *ACS Catal.*, 2018, **8**, 2253–2276.

67 A. Pant, Z. Mutlu, D. Wickramaratne, H. Cai, R. K. Lake, C. Ozkan and S. Tongay, *Nanoscale*, 2016, **8**, 3870–3887.

68 S. Wang, X. Wang, J. H. Warner and W. E. T. Al, *ACS Nano*, 2015, **9**, 5246–5254.

69 A. Behranginia, P. Yasaei, A. K. Majee, V. K. Sangwan, F. Long, C. J. Foss, T. Foroozan, S. Fuladi, M. R. Hantehzadeh, R. Shahbazian-Yassar, M. C. Hersam, Z. Aksamija and A. Salehi-Khojin, *Small*, 2017, **13**, 1–11.

70 Y. Yoo, Z. P. Degregorio and J. E. Johns, *J. Am. Chem. Soc.*, 2015, **137**, 14281–14287.

71 P. Das, Q. Fu, X. Bao and Z. S. Wu, *J. Mater. Chem. A*, 2018, **6**, 21747–21784.

72 Q. Yu, Y. Luo, A. Mahmood, B. Liu and H.-M. Cheng, *Electrochem. Energy Rev.*, 2019, **2**, 373–394.

73 X. Yu, G. Zhao, S. Gong, C. Liu, C. Wu, P. Lyu, G. Maurin and N. Zhang, *ACS Appl. Mater. Interfaces*, 2020, **12**, 24777–24785.

74 L. Shi, W. Ding, S. Yang, Z. He and S. Liu, *J. Hazard. Mater.*, 2018, **347**, 431–441.

75 Z. Zhao, S. Luo, P. Ma, Y. Luo, W. Wu, Y. Long and J. Ma, *ACS Sustainable Chem. Eng.*, 2020, **8**, 8814–8822.

76 G. Swain, S. Sultana, J. Moma and K. Parida, *Inorg. Chem.*, 2018, **57**, 10059–10071.

77 J. Wan, Y. Zhang, R. Wang, L. Liu, E. Liu, J. Fan and F. Fu, *J. Hazard. Mater.*, 2020, **384**, 121484.

78 W. Li, Y. Zhang, X. Long, J. Cao, X. Xin, X. Guan, J. Peng and X. Zheng, *Sensors*, 2019, **19**, 1–12.

79 K. Krishnamoorthy, P. Pazhamalai, G. K. Veerasubramani and S. J. Kim, *J. Power Sources*, 2016, **321**, 112–119.

80 K. Gacem, M. Boukhicha, Z. Chen and A. Shukla, *Nanotechnology*, 2012, **23**, 23–28.

81 D. Sahoo, B. Kumar, J. Sinha, S. Ghosh, S. S. Roy and B. Kaviraj, *Sci. Rep.*, 2020, **10**, 1–12.

82 A. Gupta, V. Arunachalam and S. Vasudevan, *J. Phys. Chem. Lett.*, 2016, **7**, 4884–4890.

83 H. Wang, D. Tran, J. Qian, F. Ding and D. Losic, *Adv. Mater. Interfaces*, 2019, **6**, 1900915.

84 Y. Wan, Z. Zhang, X. Xu, Z. Zhang, P. Li, X. Fang, K. Zhang, K. Yuan, K. Liu, G. Ran, Y. Li, Y. Ye and L. Dai, *Nano Energy*, 2018, **51**, 786–792.

85 S. Li, S. Wang, M. M. Salamone, A. W. Robertson, S. Nayak, H. Kim, S. C. E. Tsang, M. Pasta and J. H. Warner, *ACS Catal.*, 2017, **7**, 877–886.

86 P. Gnanasekar, D. Periyanagounder, A. Nallathambi, S. Subramani, M. Palanisamy and J. Kulandaivel, *CrystEngComm*, 2018, **20**, 4249–4257.

87 F. Wang, T. A. Shifa, X. Zhan, Y. Huang, K. Liu, Z. Cheng, C. Jiang and J. He, *Nanoscale*, 2015, **7**, 19764–19788.

88 S. Muralikrishna, K. Manjunath, D. Samrat, V. Reddy, T. Ramakrishnappa and D. H. Nagaraju, *RSC Adv.*, 2015, **5**, 89389–89396.

89 G. Swain, S. Sultana, B. Naik and K. Parida, *ACS Omega*, 2017, **2**, 3745–3753.

90 G. Swain, S. Sultana and K. Parida, *ACS Sustainable Chem. Eng.*, 2020, **8**, 4848–4862.

91 L. Li, Z. Qin, L. Ries, S. Hong, T. Michel, J. Yang, C. Salameh, M. Bechelany, P. Miele, D. Kaplan, M. Chhowalla and D. Voiry, *ACS Nano*, 2019, **13**, 6824–6834.

92 M. Xiong, J. Yan, B. Chai, G. Fan and G. Song, *J. Mater. Sci. Technol.*, 2020, **56**, 179–188.

93 R. H. Jeong, J. W. Lee, D. I. Kim, J. W. Yang, S. Park and J.-H. Boo, *Nanotechnology*, 2020, **31**, 155704.

94 W. Li, L. Wang, Q. Zhang, Z. Chen, X. Deng, C. Feng, L. Xu and M. Sun, *J. Alloys Compd.*, 2019, **808**, 151681.

95 L. Huang, B. Han, X. Huang, S. Liang, Z. Deng, W. Chen, M. Peng and H. Deng, *J. Alloys Compd.*, 2019, **798**, 553–559.

96 Z. Hennighausen, C. Lane, A. Benabbas, K. Mendez, M. Eggenberger, P. M. Champion, J. T. Robinson, A. Bansil and S. Kar, *ACS Appl. Mater. Interfaces*, 2019, **11**, 15913–15921.

97 R. K. Biroju, S. Pal, R. Sharma, P. K. Giri and T. N. Narayanan, *Nanotechnology*, 2017, **28**, 085101.

98 X. Zhai, X. Zhai, X. Xu, J. Peng, J. Peng, F. Jing, F. Jing, Q. Zhang, H. Liu, H. Liu, H. Liu, Z. Hu and Z. Hu, *ACS Appl. Mater. Interfaces*, 2020, **12**, 24093–24101.

99 J. Zhang, J. H. Wang, P. Chen, Y. Sun, S. Wu, Z. Y. Jia, X. B. Lu, H. Yu, W. Chen, J. Q. Zhu, G. B. Xie, R. Yang, D. X. Shi, X. L. Xu, J. Y. Xiang, K. H. Liu and G. Y. Zhang, *Adv. Mater.*, 2016, **28**, 1950–1956.

100 J. Shi, R. Tong, X. Zhou, Y. Gong, Z. Zhang, Q. Ji, Y. Zhang, Q. Fang, L. Gu, X. Wang, Z. Liu and Y. Zhang, *Adv. Mater.*, 2016, **28**, 10664–10672.

101 E. Lee, S. G. Lee, W. H. Lee, H. C. Lee, N. N. Nguyen, M. S. Yoo and K. Cho, *Chem. Mater.*, 2020, **32**, 4544–4552.

102 R. Ji, Z. Zhu, W. Ma, X. Tang, Y. Liu and P. Huo, *Catal. Sci. Technol.*, 2020, **10**, 788–800.

103 Y. J. Yuan, P. Wang, Z. Li, Y. Wu, W. Bai, Y. Su, J. Guan, S. Wu, J. Zhong, Z. T. Yu and Z. Zou, *Appl. Catal., B*, 2019, **242**, 1–8.

104 S. Nayak, G. Swain and K. Parida, *ACS Appl. Mater. Interfaces*, 2019, **11**, 20923–20942.

105 C. Chen, X. Xie, B. Anasori, A. Sarycheva, T. Makaryan, M. Zhao, P. Urbankowski, L. Miao, J. Jiang and Y. Gogotsi, *Angew. Chem., Int. Ed.*, 2018, **57**, 1846–1850.

106 A. Wu, Y. Gu, Y. Xie, C. Tian, H. Yan, D. Wang, X. Zhang, Z. Cai and H. Fu, *ACS Appl. Mater. Interfaces*, 2019, **11**, 25986–25995.

107 S. Zhang, H. Yang, H. Gao, R. Cao, J. Huang and X. Xu, *ACS Appl. Mater. Interfaces*, 2017, **9**, 23635–23646.

108 B. Zhang, H. Shi, X. Hu, Y. Wang, E. Liu and J. Fan, *J. Phys. D: Appl. Phys.*, 2020, **53**, 205101.

109 W. Fu, H. He, Z. Zhang, C. Wu, X. Wang, H. Wang, Q. Zeng, L. Sun, X. Wang, J. Zhou, Q. Fu, P. Yu, Z. Shen, C. Jin, B. I. Yakobson and Z. Liu, *Nano Energy*, 2016, **27**, 44–50.

110 G. Dong, P. Qiu, F. Meng, Y. Wang, B. He, Y. Yu, X. Liu and Z. Li, *Chem. Eng. J.*, 2020, **384**, 123330.

111 S. H. Yu, Z. Tang, Y. Shao, H. Dai, H. Y. Wang, J. Yan, H. Pan and D. H. C. Chua, *ACS Appl. Energy Mater.*, 2019, **2**, 5799–5808.

112 J. M. Woods, Y. Jung, Y. Xie, W. Liu, Y. Liu, H. Wang and J. J. Cha, *ACS Nano*, 2016, **10**, 2004–2009.

113 S. Subudhi, G. Swain, S. P. Tripathy and K. Parida, *Inorg. Chem.*, 2020, **59**, 9824–9837.

114 S. Acharya, G. Swain and K. M. Parida, *Int. J. Hydrogen Energy*, 2020, **45**, 11502–11511.

115 G. Swain, S. Sultana and K. Parida, *Inorg. Chem.*, 2019, **58**, 9941–9955.

116 S. Jayabal, G. Saranya, J. Wu, Y. Liu, D. Geng and X. Meng, *J. Mater. Chem. A*, 2017, **5**, 24540–24563.

117 L. Zhang, X. Ji, X. Ren, Y. Ma, X. Shi, Z. Tian, A. M. Asiri, L. Chen, B. Tang and X. Sun, *Adv. Mater.*, 2018, **30**, 2–7.

118 H. Liu, Y. Zhu, J. Ma, Z. Zhang and W. Hu, *Adv. Funct. Mater.*, 2020, **30**, 1–21.

119 J. Xiong, J. Di, J. Xia, W. Zhu and H. Li, *Adv. Funct. Mater.*, 2018, **28**, 1801983.

120 J. Xiong, J. Di and H. Li, *J. Mater. Chem. A*, 2020, **8**, 12928–12950.

121 E. D. Koutsouroubi, I. Vamvasakis, I. T. Papadas, C. Drivas, S. A. Choulis, S. Kennou and G. S. Armatas, *ChemPlusChem*, 2020, **85**, 1379–1388.

122 D. P. Sahoo, S. Patnaik and K. Parida, *ACS Omega*, 2019, **4**, 14721–14741.

123 A. Behera, D. Kandi, S. Sahoo and K. Parida, *J. Phys. Chem. C*, 2019, **123**, 17112–17126.

124 S. Subudhi, S. Mansingh, G. Swain, A. Behera, D. Rath and K. Parida, *Inorg. Chem.*, 2019, **58**, 4921–4934.

125 L. Paramanik, K. H. Reddy, S. Sultana and K. Parida, *Inorg. Chem.*, 2018, **57**, 15133–15148.

126 S. Nayak, A. C. Pradhan and K. M. Parida, *Inorg. Chem.*, 2018, **57**, 8646–8661.

127 Q. Zhu, Y. Qu, D. Liu, K. W. Ng and H. Pan, *ACS Appl. Nano Mater.*, 2020, **3**, 6270–6296.

128 S. J. Rowley-Neale, D. A. C. Brownson, G. C. Smith, D. A. G. Sawtell, P. J. Kelly and C. E. Banks, *Nanoscale*, 2015, **7**, 18152–18168.

129 C. Tsai, F. A. Pedersen and J. K. Nørskov, *Nano Lett.*, 2014, **14**, 1381–1387.

130 R. Peng, L. Liang, Z. D. Hood, A. Boulesbaa, A. Puretzky, A. V. Ievlev, J. Come, O. S. Ovchinnikova, H. Wang, C. Ma, M. Chi, B. G. Sumpter and Z. Wu, *ACS Catal.*, 2016, **6**, 6723–6729.

131 T. F. Jaramillo, K. P. Jørgensen, J. Bonde, J. H. Nielsen, S. Horch and I. Chorkendorff, *Science*, 2007, **317**, 100–102.

132 B. Hinnemann, P. G. Moses, J. Bonde, K. P. Jørgensen, J. H. Nielsen, S. Horch, I. Chorkendorff and J. K. Nørskov, *J. Am. Chem. Soc.*, 2005, **127**, 5308–5309.

133 X. Kong, X. Shen, C. Zhang, S. N. Oliaee and Z. Peng, *Inorg. Chem. Front.*, 2016, **3**, 1376–1380.

134 J. Xie, H. Qu, J. Xin, X. Zhang, G. Cui, X. Zhang, J. Bao, B. Tang and Y. Xie, *Nano Res.*, 2017, **10**, 1178–1188.

135 D. Zhu, J. Liu, Y. Zhao, Y. Zheng and S. Z. Qiao, *Small*, 2019, **15**, 1–8.

136 T. Liang, Y. Liu, Y. Cheng, F. Ma and Z. Dai, *ChemCatChem*, 2020, **12**, 2840–2848.

137 U. Gupta and C. N. R. Rao, *Nano Energy*, 2017, **41**, 49–65.

138 J. Wan, R. Wang, L. Liu, J. Fan, E. Liu, X. Gao and F. Fu, *Int. J. Hydrogen Energy*, 2019, **44**, 16639–16647.

139 H. Wang, S. Li, Q. Wan, X. Su, T. Song, X. Wang and J. Wang, *J. Colloid Interface Sci.*, 2020, **577**, 38–47.

140 Y. J. Yuan, Z. J. Ye, H. W. Lu, B. Hu, Y. H. Li, D. Q. Chen, J. S. Zhong, Z. T. Yu and Z. G. Zou, *ACS Catal.*, 2016, **6**, 532–541.

141 Y. J. Yuan, Z. Li, S. Wu, D. Chen, L. X. Yang, D. Cao, W. G. Tu, Z. T. Yu and Z. G. Zou, *Chem. Eng. J.*, 2018, **350**, 335–343.

142 Y. J. Yuan, Z. Shen, S. Wu, Y. Su, L. Pei, Z. Ji, M. Ding, W. Bai, Y. Chen, Z. T. Yu and Z. Zou, *Appl. Catal., B*, 2019, **246**, 120–128.

143 Y. J. Yuan, Y. Yang, Z. Li, D. Chen, S. Wu, G. Fang, W. Bai, M. Ding, L. X. Yang, D. P. Cao, Z. T. Yu and Z. G. Zou, *ACS Appl. Energy Mater.*, 2018, **1**, 1400–1407.

144 B. Chai, M. Xu, J. Yan and Z. Ren, *Appl. Surf. Sci.*, 2018, **430**, 523–530.

145 L. M. Azofra, N. Li, D. R. Macfarlane and C. Sun, *Energy Environ. Sci.*, 2016, **9**, 2545–2549.

146 X. Cui, C. Tang and Q. Zhang, *Adv. Energy Mater.*, 2018, **8**, 1–25.

147 A. Chen and B. Y. Xia, *J. Mater. Chem. A*, 2019, **7**, 23416–23431.

148 Q. Liu, X. Zhang, B. Zhang, Y. Luo, G. Cui, F. Xie and X. Sun, *Nanoscale*, 2018, **10**, 14386–14389.

149 H. Li, C. Mao, H. Shang, Z. Yang, Z. Ai and L. Zhang, *Nanoscale*, 2018, **10**, 15429–15435.

150 S. Mansingh, S. Sultana, R. Acharya, M. K. Ghosh and K. M. Parida, *Inorg. Chem.*, 2020, **59**, 6646–6646.

151 S. Mansingh, K. K. Das, A. Behera, S. Subudhi, S. Sultana and K. Parida, *Nanoscale Adv.*, 2020, **2**, 2004–2017.

152 S. Sultana, S. Mansingh and K. M. Parida, *J. Mater. Chem. A*, 2019, **7**, 9145–9153.

153 C. Yang, Y. Zhu, J. Liu, Y. Qin, H. Wang, H. Liu, Y. Chen, Z. Zhang and W. Hu, *Nano Energy*, 2020, **77**, 105126.

154 M. Kim, B. C. Yeo, Y. Park, H. M. Lee, S. S. Han and D. Kim, *Chem. Mater.*, 2019, **32**, 709–720.

155 C. Guo, J. Ran, A. Vasileff and S. Z. Qiao, *Energy Environ. Sci.*, 2018, **11**, 45–56.

156 R. Manjunatha, A. Karajić, M. Liu, Z. Zhai, L. Dong, W. Yan, D. P. Wilkinson and J. Zhang, *Electrochem. Energy Rev.*, 2020, **3**, 506–540.

157 B. H. R. Suryanto, D. Wang, L. M. Azofra, M. Harb, L. Cavallo, R. Jalili, D. R. G. Mitchell, M. Chatti and D. R. MacFarlane, *ACS Energy Lett.*, 2019, **4**, 430–435.

158 Y. Liu, M. Han, Q. Xiong, S. Zhang, C. Zhao, W. Gong, G. Wang, H. Zhang and H. Zhao, *Adv. Energy Mater.*, 2019, **9**, 1–9.

159 K. Chu, Y. P. Liu, Y. B. Li, Y. L. Guo and Y. Tian, *ACS Appl. Mater. Interfaces*, 2020, **12**, 7081–7090.

160 X. Li, X. Ren, X. Liu, J. Zhao, X. Sun, Y. Zhang, X. Kuang, T. Yan, Q. Wei and D. Wu, *J. Mater. Chem. A*, 2019, **7**, 2524–2528.

161 H. Hirakawa, M. Hashimoto, Y. Shiraishi and T. Hirai, *J. Am. Chem. Soc.*, 2017, **139**, 10929–10936.

162 A. Shi, H. Li, S. Yin, Z. Hou, J. Rong, J. Zhang and Y. Wang, *Appl. Catal., B*, 2018, **235**, 197–206.

163 Y. Hao, X. Dong, S. Zhai, H. Ma, X. Wang and X. Zhang, *Chem. – Eur. J.*, 2016, **22**, 18722–18728.

164 K. Li, X. An, K. H. Park, M. Khraisheh and J. Tang, *Catal. Today*, 2014, **224**, 3–12.

165 S. Das, J. Pérez-Ramírez, J. Gong, N. Dewangan, K. Hidajat, B. C. Gates and S. Kawi, *Chem. Soc. Rev.*, 2020, **49**, 2937–3004.

166 E. V. Kondratenko, G. Mul, J. Baltrusaitis, G. O. Larrazábal and J. Pérez-Ramírez, *Energy Environ. Sci.*, 2013, **6**, 3112–3135.

167 A. U. Pawar, C. W. Kim, M. T. Nguyen-Le and Y. S. Kang, *ACS Sustainable Chem. Eng.*, 2019, **7**, 7431–7455.

168 K. Chan, C. Tsai, H. A. Hansen and J. K. Nørskov, *ChemCatChem*, 2014, **6**, 1899–1905.

169 Y. Xie, X. Li, Y. Wang, B. Li, L. Yang, N. Zhao, M. Liu, X. Wang, Y. Yu and J. M. Liu, *Appl. Surf. Sci.*, 2020, **499**, 143964.

170 W. Tu, Y. Li, L. Kuai, Y. Zhou, Q. Xu, H. Li, X. Wang, M. Xiao and Z. Zou, *Nanoscale*, 2017, **9**, 9065–9070.

171 X. Ma, Z. Li, L. E. K. Achenie and H. Xin, *J. Phys. Chem. Lett.*, 2015, **6**, 3528–3533.

172 A. Chen, X. Zhang, L. Chen, S. Yao and Z. Zhou, *J. Phys. Chem. C*, 2020, **124**, 22471–22478.

173 R. A. Geioushy, S. M. El-Sheikh, I. M. Hegazy, A. Shawky, S. El-Sherbiny and A. H. T. Kandil, *Mater. Res. Bull.*, 2019, **118**, 110499.

174 S. Yin, J. Li, L. Sun, X. Li, D. Shen, X. Song, P. Huo, H. Wang and Y. Yan, *Inorg. Chem.*, 2019, **58**, 15590–15601.

175 S. Garg, M. Li, A. Z. Weber, L. Ge, L. Li, V. Rudolph, G. Wang and T. E. Rufford, *J. Mater. Chem. A*, 2020, **8**, 1511–1544.

176 C. Yang, S. Li, Z. Zhang, H. Wang, H. Liu, F. Jiao, Z. Guo, X. Zhang and W. Hu, *Small*, 2020, **16**, 2001847.

177 M. Asadi, B. Kumar, A. Behranginia, B. A. Rosen, A. Baskin, N. Repnin, D. Pisasale, P. Phillips, W. Zhu, R. Haasch, R. F. Klie, P. Král, J. Abiade and A. Salehi-Khojin, *Nat. Commun.*, 2014, **5**, 1–8.

178 K. Lv, C. Teng, M. Shi, Y. Yuan, Y. Zhu, J. Wang, Z. Kong, X. Lu and Y. Zhu, *Adv. Funct. Mater.*, 2018, **28**, 1–10.

179 S. A. Francis, J. M. Velazquez, I. M. Ferrer, D. A. Torelli, D. Guevarra, M. T. McDowell, K. Sun, X. Zhou, F. H. Saadi, J. John, M. H. Richter, F. P. Hyler, K. M. Papadantonakis, B. S. Brunschwig and N. S. Lewis, *Chem. Mater.*, 2018, **30**, 4902–4908.

180 F. Li, S. F. Zhao, L. Chen, A. Khan, D. R. MacFarlane and J. Zhang, *Energy Environ. Sci.*, 2016, **9**, 216–223.

181 Y. Wang, Z. Zhang, L. Zhang, Z. Luo, J. Shen, H. Lin, J. Long, J. C. S. Wu, X. Fu, X. Wang and C. Li, *J. Am. Chem. Soc.*, 2018, **140**, 14595–14598.

182 C. Qiu, S. Bai, W. Cao, L. Tan, J. Liu, Y. Zhao and Y. F. Song, *Trans. Tianjin Univ.*, 2020, **26**, 352–361.

183 N. Kumar, S. S. Ray, S. Kumar, R. Gusain, N. Manyala and S. Eslava, *ACS Appl. Energy Mater.*, 2020, **3**, 9897–9909.

184 F. Xu, B. Zhu, B. Cheng, J. Yu and J. Xu, *Adv. Opt. Mater.*, 2018, **6**, 1800911.

185 Y. Wang, Z. Zhang, L. Zhang, Z. Luo, J. Shen, H. Lin, J. Long, J. C. S. Wu, X. Fu, X. Wang and C. Li, *J. Am. Chem. Soc.*, 2018, **140**, 14595–14598.

186 P. Y. Jia, R. T. Guo, W. G. Pan, C. Y. Huang, J. Y. Tang, X. Y. Liu, H. Qin and Q. Y. Xu, *Colloids Surf., A*, 2019, **570**, 306–316.

187 V. Yadav, S. Roy, P. Singh, Z. Khan and A. Jaiswal, *Small*, 2019, **15**, 1803706.

188 J. H. Hwang, M. A. Islam, H. Choi, T. J. Ko, K. L. Rodriguez, H. S. Chung, Y. Jung and W. H. Lee, *Anal. Chem.*, 2019, **91**, 11770–11777.

189 D. Vikraman, S. A. Patil, S. Hussain, N. Mengal, H. S. Kim, S. H. Jeong, J. Jung, H. S. Kim and H. J. Park, *Dyes Pigm.*, 2018, **151**, 7–14.

190 Y. Liu, S. Zhang, J. He, Z. M. Wang and Z. Liu, *Nano-Micro Lett.*, 2019, **11**, 1–24.

191 D. Lembke, S. Bertolazzi and A. Kis, *Acc. Chem. Res.*, 2015, **48**, 100–110.

192 Y. P. Venkata Subbaiah, K. J. Saji and A. Tiwari, *Adv. Funct. Mater.*, 2016, **26**, 2046–2069.

193 B. Radisavljevic, A. Radenovic, J. Brivio, V. Giacometti and A. Kis, *Nat. Nanotechnol.*, 2011, **6**, 147–150.

194 E. Singh, P. Singh, K. S. Kim, G. Y. Yeom and H. S. Nalwa, *ACS Appl. Mater. Interfaces*, 2019, **11**, 11061–11105.

195 T. Nawz, A. Safdar, M. Hussain, D. S. Lee and M. Siyar, *Crystals*, 2020, **10**, 902.

196 N. Joseph, P. M. Shafi and A. C. Bose, *Energy Fuels*, 2020, **34**, 6558–6597.

197 E. Pomerantseva and Y. Gogotsi, *Nat. Energy*, 2017, **2**, 1–6.

198 B. Wang, Q. Wu, H. Sun, J. Zhang, J. Ren, Y. Luo, M. Wang and H. Peng, *J. Mater. Chem. A*, 2017, **5**, 925–930.

199 B. Kirubasankar, M. Narayanasamy, J. Yang, M. Han, W. Zhu, Y. Su, S. Angaiah and C. Yan, *Appl. Surf. Sci.*, 2020, **534**, 147644.

200 M. W. Kadi, R. M. Mohamed and A. A. Ismail, *J. Nanopart. Res.*, 2020, **22**, 156.

201 J. Zhang, C. Xing and F. Shi, *Int. J. Hydrogen Energy*, 2020, **45**, 6291–6301.

202 D. Jiang, B. Wen, Y. Zhang, Y. Jin, D. Li and M. Chen, *J. Colloid Interface Sci.*, 2019, **536**, 1–8.

203 X. Xu, Z. Si, L. Liu, Z. Wang, Z. Chen, R. Ran, Y. He and D. Weng, *Appl. Surf. Sci.*, 2018, **435**, 1296–1306.

204 Y. Li, Z. Yin, G. Ji, Z. Liang, Y. Xue, Y. Guo, J. Tian, X. Wang and H. Cui, *Appl. Catal., B*, 2019, **246**, 12–20.

205 Y. Chen, F. Su, H. Xie, R. Wang, C. Ding, J. Huang, Y. Xu and L. Ye, *Chem. Eng. J.*, 2021, **404**, 126498.

206 J. Xu, X. Yan, Y. Qi, Y. Fu, C. Wang and L. Wang, *Chem. Eng. J.*, 2019, **375**, 122053.

207 J. Tao, X. Yu, Q. Liu, G. Liu and H. Tang, *J. Colloid Interface Sci.*, 2021, **585**, 470–479.

208 C. M. Nagaraja, M. Kaur and S. Dhingra, *Int. J. Hydrogen Energy*, 2020, **45**, 8497–8506.

209 J. Deng, H. Li, J. Xiao, Y. Tu, D. Deng, H. Yang, H. Tian, J. Li, P. Ren and X. Bao, *Energy Environ. Sci.*, 2015, **8**, 1594–1601.

210 G. B. De-Mello, L. Smith, S. J. Rowley-Neale, J. Gruber, S. J. Hutton and C. E. Banks, *RSC Adv.*, 2017, **7**, 36208–36213.

211 H. Huang, J. Song, D. Yu, Y. Hao, Y. Wang and S. Peng, *Appl. Surf. Sci.*, 2020, **525**, 146623.

212 H. Yu, Y. Xue, L. Hui, C. Zhang, Y. Zhao, Z. Li and Y. Li, *Adv. Funct. Mater.*, 2018, **28**, 1707564.

213 A. M. Abraham, G. Bharath, A. Hai and F. Banat, *J. Phys. D: Appl. Phys.*, 2019, **53**, 065501.

214 J. Lv, M. Yang, T. Liang, S. Ken and M. Hideo, *Chem. Phys. Lett.*, 2017, **678**, 212–215.

215 X. Zhang, M. Zhang, Y. Tian, J. You, C. Yang, J. Su, Y. Li, Y. Gao and H. Gu, *RSC Adv.*, 2018, **8**, 10698–10705.

216 B. Liu, J. Qin, H. Yang, X. Hu, W. Zhao and Z. Zhang, *ChemCatChem*, 2020, **12**, 5221–5228.

217 H. Qin, R. T. Guo, X. Y. Liu, W. G. Pan, Z. Y. Wang, X. Shi, J. Y. Tang and C. Y. Huang, *Dalton Trans.*, 2018, **47**, 15155–15163.